AD-758 778

THEORETICAL AND EXPERIMENTAL STUDIES OF VLF AND LF WAVES

Norbert Nessler

Innsbruck University
Innsbruck, Austria

28 February 1972

AFOSR-TR 73-0174

AD 758778

DOCUMENT CONTROL DATA - R & D

(Security classification of title, body of abstract and indexing annotation must be entered when the overall report is classified)

1. ORIGINATING ACTIVITY (Corporate author)	2a. REPORT SECURITY CLASSIFICATION
University of Innsbruck Innsbruck, Austria	2b. GROUP

3. REPORT TITLE

THEORETICAL AND EXPERIMENTAL STUDIES OF VLF AND LF WAVES

4. DESCRIPTIVE NOTES (Type of report and inclusive dates)

Scientific Final

5. AUTHOR(S) (First name, middle initial, last name)

E. BERLOFFA, D. FRITZ, R. KLEIN, H. LEONHARD, Dr. N. NESSLER, M. WIESER

6. REPORT DATE	7a. TOTAL NO. OF PAGES	7b. NO. OF REFS
February 28, 1973	151 /5	40

8a. CONTRACT OR GRANT NO	9a. ORIGINATOR'S REPORT NUMBER(S)
F44620-72-C-0052	
b. PROJECT NO	4-72
4600-10	
c. 52702F	9b. OTHER REPORT NO(S) (Any other numbers that may be assigned this report)
674700	
d.	

10. DISTRIBUTION STATEMENT

This document has been approved for public release and sale; its distribution is unlimited.

11. SUPPLEMENTARY NOTES	12. SPONSORING MILITARY ACTIVITY
Tech. other	United States Government American Embassy (EOAR) London, England

13. ABSTRACT

The results of the research on the production, transmission and reception of VLF and LF waves is represented in 9 compact chapters. A new improved equivalent circuit diagram for the helix is calculated giving a good explanation of the measured effects over a large frequency range. The receiving characteristic of a ferrite rod antenna in the elliptically polarized field is investigated specifying a method that allows all ellipse parameters to be measured simultaneously. The phase measurement at VLF-wave propagation and the device built for this purpose are described and an improved universally usable digital phase measuring equipment for a large frequency range is particularized. The various pehnomena, e.g. reflection, refraction, and wave guiding, that are occurring at VLF and LF wave propagation are described and explained. A detailed description of a long-time registration of commercial VLF transmitters is given.

DD FORM 1473
1 NOV 65

iq

Security Classification

| 14 KEY WORDS	LINK A		LINK B		LINK C	
	ROLE	WT	ROLE	WT	ROLE	WT
trihedral built from ferrite rod antennas						
rotary field ellipse						
phase angles in rotary field ellipse						
spatial position of rotary field ellipse						
wave propagation in valleys						
wave guide theory for mountain valleys						
conformal mapping of hollow wave guides						
superposition of field components						
vector components of the VLF field						
measurements of the rotary field ellipse						
receiving characteristics of a ferrite rod antenna (pedaloid)						
mathematical description of pedaloid						
intersection surface of the pedaloid						
direction finding error in elliptically polarized fields						
helical antennas						
helical antennas for VLF waves						
equivalent circuit of helical antennas						
resonance frequencies of helical antennas						
parameters of helical antennas						
efficiency of helical antennas in air						
phase measurements for VLF waves						
digital phase measuring equipment						
errors of phase measuring devices						
registration of VLF transmitters						
subsurface registration of VLF transmitters						
transmission coefficient of VLF waves						

15

February 28, 1973

FINAL SCIENTIFIC REPORT
1972

THEORETICAL AND EXPERIMENTAL STUDIES OF VLF AND LF WAVES

Jan. 1, 1972 to Dec. 31, 1972

Dr. Norbert NESSLER

University of Innsbruck

Physics Institute

Electronics Laboratory
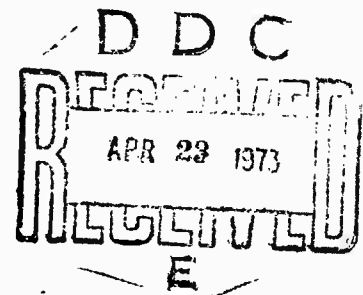
DDC

RECEIVED

APR 23 1973

E

159

PREFACE

During the past 12 years of research on the subject "Theoretical and experimental studies of VLF and LF waves" quite a number of scientific conclusions could be drawn that are reflected in more than hundred papers and were read at several scientific conferences and meetings.

Under the VLF Research Contracts nine comprehensive thesises were completed up to now, four more are in preparation.

Experimental measurements and investigations were conducted in the home mines of Grosskogel/St. Gertraudi, Falkenstein/Schwaz, Lafatsch/Scharnitz, and salt mine Hall (all of them in the Tyrol), as well as in Bleiberg/Carinthia, Mitterberg/Salzburg and in some German and Dutch mines.

In addition to commercial apparatuses and measuring instruments we have designed and built a great number of devices and equipments ourselves to reach an utmost efficiency for our specific purposes. We may especially mention the stationary facilities in the mine of St. Gertraudi, e.g. the fully conditioned mine laboratory, the floodable gallery with the pumping equipment for subsurface experiments, and the big frame antenna, that could be constructed despite of our limited budgetary funds thanks to the generous assistance of our home industries.

The general rise in prices, the shortening of budgetary funds in connection with the financial situation of the USA and last not least the devaluation of the

II

VLF Team 1972

Contractor: Dr. Norbert NESSLER

Principal Investigator: Dr. Norbert NESSLER

Thesis graduates: Erich BERLOFFA[2]

                  Dieter FRITZ

                  Richard KLEIN[2]

                  Helmut LEONHARD

                  Michael OBERLADSTÄTTER[1]

                  Manfred WIESER

[1] Started in 1972

[2] Finished his studies in 1972.

Scientific consultant: Dr. E. SALPETER

Technical consultant: Walter GRADL

Office: Brigitte NESSLER

ABSTRACT

The results of the research on the production, transmission and reception of VLF and LF waves is represented in 9 compact chapters.

A new improved equivalent circuit diagram for the helix is calculated giving a good explanation of the measured effects over a large frequency range. The receiving characteristic of a ferrite rod antenna in the elliptically polarized field is investigated specifying a method that allows all allipse parameters to be measured simultaneously.

The phase measurement at VLF-wave propagation and the device built for this purpose are described and an improved universally usable digital phase measuring equipment for a large frequency range is particularized.

The various phenomena, e.g. reflection, refraction, and wave guiding, that are occurring at VLF and LF wave propagation are described and explained.

A detailed description of a long-time registration of commercial VLF transmitters is given.

CONTENTS

LIST OF ILLUSTRATIONS

CHAPTER 1

HELICAL ANTENNAS IN THE VLF-RANGE

The impedances of the antennas H 1136, H 328, and
H 329 Cull in air showed the same characteristic shape
of real and imaginary part in the graphical representa-
tion as has been stated earlier with the antenna
H 772 /1/. The shape of the curves computed at Innsbruck
University reminds of the impedance characteristics of
a quartz crystal. It was now near at hand to examine the
equivalent circuit diagram of a quartz crystal more
thoroughly with particular consideration of its appli-
cability for the special case and possibly to modify it.

The equivalent circuit diagram

A small helix for long waves can be thought of as com-
posed in the following way:
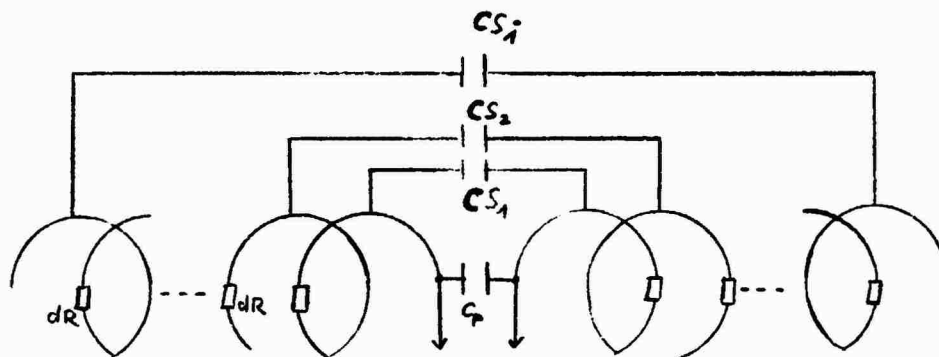
Fig. 1.1

with dL, dR, C_p being constant, CS_i being different.

In the simplified diagram
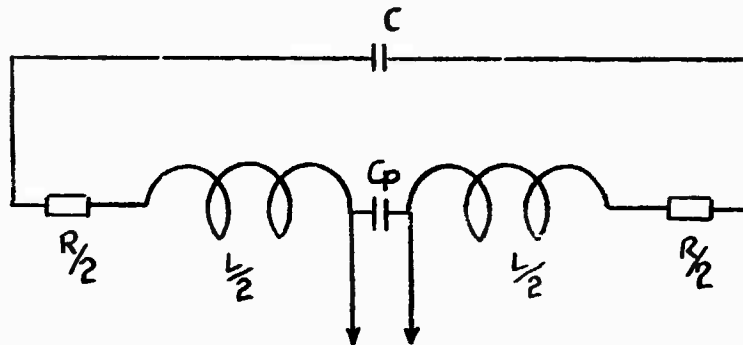
Fig. 1.2

all CS_i were united to C; R, L, C, and C_p remain constant. Fig. 1.3 shows the modified diagram.
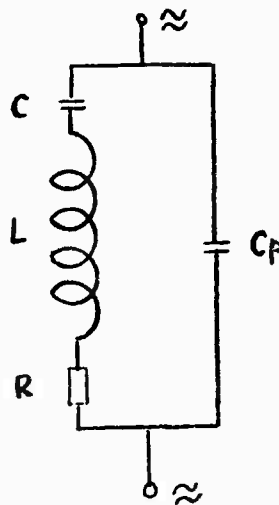
Fig. 1.3

This diagram is identical with the equivalent circuit diagram of a quartz crystal.

Calculation of the impedance of the circuit

The complex conductance amounts to

$$Y = j\omega C_p + \frac{1}{R + j(\omega L - \frac{1}{\omega C})} \quad \text{with } \omega = 2\pi f$$

or

$$Y = \frac{1}{R^2 + (\omega L - \frac{1}{\omega C})} + j \left(-\frac{\omega L - \frac{1}{\omega C}}{R + (\omega L - \frac{1}{\omega C})} + \omega C_p \right) \tag{1.1}$$

with real and imaginary part separated.

Therefrom real and imaginary part of the complex total resistance Z is calculated to be

$$ReZ = \frac{R}{1 + \omega^2 C_p^2 (R^2 + H^2) - 2\omega C_p \cdot H} \tag{1.2}$$

$$ImZ = \frac{H - \omega C_p (R^2 + H^2)}{1 + C_p (R + H) - 2 C_p \cdot H} \tag{1.3}$$

with the abbreviation

$$H = (\omega L - \frac{1}{\omega C})$$

Resonance frequencies

The resonance frequencies are calculated from ImZ = 0, resulting

$$H - \omega C_p (R^2 + H^2) = 0 \tag{1.4}$$

and therefrom we obtain a biquadratic equation for ω:

$$\omega^4 - \omega^2 \left(\frac{1}{LC_p} - \frac{R^2}{L^2} + 2 \cdot \frac{1}{LC} \right) + \frac{1}{C} \frac{1}{L^2 C_p} + \frac{1}{L^2 C^2} = 0 \tag{1.5}$$

with the solution

$$\omega^2_{res} = \frac{1}{2LC_p} - \frac{R^2}{2L^2} + \frac{1}{LC} \pm \frac{1}{2LC_p} \sqrt{1 + \frac{R^4 C_p^2}{L^2} \quad \frac{4R^2 C_p^2}{LC} \quad \frac{2R^2 C_p}{L}} \tag{1.6}$$

With the antennas in question, R and C are small, L is large; so the following approximations can be introduced:

$$\frac{2R^2C_p}{L} < 1; \qquad \frac{4R^2C_p^2}{LC} < 1.$$

The root is expanded into a series, the term $\frac{R^4C_p}{L^2}$ can be neglected.

$$\omega^2_{res} \quad \frac{1}{LC} + \frac{1}{2LC_p} - \frac{R^2}{2L^2} \pm \frac{1}{2LC_p} \left[1 - \frac{2R^2C_p^2}{LC} - \frac{R^2C_p}{L} \right] \quad (1.7)$$

resulting

$$\omega^2_1 \quad \frac{C + C_p}{LCC_p} \left(1 - \frac{R^2C_p}{L} \right) \qquad (1.8)$$

$$\omega^2_2 \quad \frac{1}{LC} \left(1 + \frac{R^2C_p}{L} \right) \qquad (1.9)$$

For the special case R = 0 all neglected terms disappear so that the resonance frequency reads as follows:

$$\omega^2_1 (R=0) = \frac{C+C_p}{LCC_p} = \omega^2_{10}; \quad \omega_{10} = \frac{1}{\sqrt{LC}} \sqrt{1 + \frac{C}{C_p}} \qquad (1.10)$$

$$\omega^2_2 (R=0) = \frac{1}{LC} = \omega^2_{20}; \qquad \omega_{20} = \frac{1}{\sqrt{LC}} \qquad (1.11)$$

Thus, two neighboring resonance frequencies appear: The first (lowest) resonance originates in the series circuit L-R-C (Fig. 1.3) with C_p as capacitive load parallel to the generator.

The second (slightly higher) resonance forms in the parallel circuit L-R on the one hand and C in series with C_p on the other hand. The tap occurs at the capacitive divider C, C_p.

From (1.8) and (1.9)

$$\omega_1 \approx \omega_p = \frac{1}{\sqrt{LC}} \sqrt{1 + \frac{C}{C_p}} \left(1 - \frac{R^2 C_p}{2L}\right) \qquad (1.12)$$

$$\omega_2 \approx \omega_s = \frac{1}{\sqrt{LC}} \left(1 + \frac{R^2 C_p}{2L}\right) \qquad (1.13)$$

is calculated.

Generally, $\frac{R^2 C_p}{2L} \ll 1$, i.e. the shift of the resonance frequency on account of the loss resistance is negligible with the antennas used here (smaller than the inaccuracy of measurement).

Loss factors are:

for parallel resonance $\left[\frac{R^2 C_p}{2L} \ll 1\right]$

$$\tan \delta_p = \frac{IR}{I \omega_p \cdot L} \qquad \frac{R}{\omega_{po} \cdot L} = R\sqrt{\frac{C}{L\left(1 + \frac{C}{C_p}\right)}} \qquad (1.14)$$

for series resonance $\left[\frac{R^2 C_p}{2L} \ll 1\right]$

$$\tan \delta_s = \frac{R}{\omega_s \cdot L} \qquad \frac{R}{\omega_{so} \cdot L} = R\sqrt{\frac{C}{L}} \qquad (1.15)$$

With the assumption of small loss factors the resonant impedances are calculated as

$$|Z| \approx \frac{1}{R(\omega_{po} C_p)^2} = \frac{C_p \cdot L}{R C_p (C + C_p)} = R_p \qquad (1.16)$$

for parallel resonance, and

$$Y = \frac{1}{R} (1 + j\omega_{s_o} C_p \cdot R) \approx \frac{1}{R} \qquad \frac{1}{|Y|} = R_s \approx R \quad (1.17)$$

for series resonance.

From the loss factors both quality and band width can be calculated:

$$Q_s = \tan \delta_s = \frac{1}{R} \sqrt{\frac{L}{C}} \ , \qquad Q_p = \frac{1}{R} \sqrt{\frac{L(1 - \frac{C}{C_p})}{C}}$$

$$b = \Delta f = \tan \delta \cdot f_{res} \implies b_s = b_p = \frac{R}{2\pi \cdot L} \quad (1.18)$$

The calculation of the constants L, R, C, and C_p from the geometric and electric data of antenna and feed line

Inductance L: calculated in approximation as inductance of a long air-core coil /2/. An accurate calculation is given in /3/:

Inductance of a single-layer cylindrical coil:

$$L_o = \frac{21.8 \cdot n^2 \cdot r}{1 + 2.2 \cdot \frac{1}{r}} \cdot 10^{-7} \qquad |H, m| \qquad (1.19)$$

21 .... total length
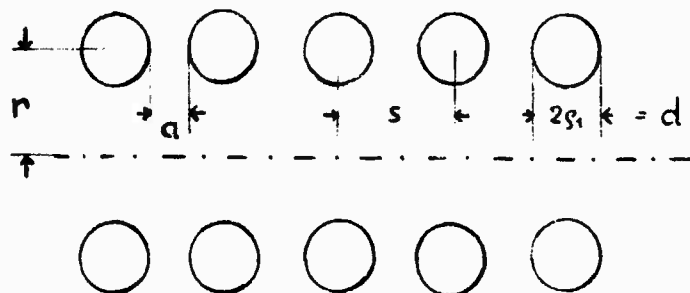
Fig. 1.4

If the clear distance $\underline{a}$ between two neighboring windings is not equal to the wire thickness $2\rho_1 = d$, the correction term ΔL must be added to Eq. (1.19).

$$\Delta L = 2n \cdot K_8 \cdot r \cdot 10^{-7} \qquad |H, m| \qquad (1.20)$$

The correction factor K_8 can be taken from Fig. 1.5.

Series loss resistance R_{total}:

The series loss resistance R of the antenna consists of the following partial resistances:

$$R_{total} = R_{wire} + R_{eddy\ curr.} + R_{diel.} + R_{rad.}$$

1. R_{wire} is the Ohmic resistance of the wire where a current I with the frequency f flows. Current displacement by skin and proximity effect must be considered at the calculation of R_{wire}.

The Ohmic resistance R_O of the wire material can be taken from tables /4/. The Ohmic resistances for wire gauges relevant for helical antennas are listed in Table 1.1.

Table 1.1: Resistance of a round Cu wire in dependence of diameter.

$\emptyset$ $|mm|$	q $|mm^2|$	R(O $\cdot$.,/m)	l per R $\left|\frac{m}{\Omega}\right|$
0.9	0.6362	0.0281	35.6
1.0	0.7854	0.0227	43.9
1.1	0.9503	0.0188	53.2
1.2	1.131	0.0158	63.2
1.5	1.767	0.0101	99

The increase of resistance caused by skin effect is thoroughly dealt with in /3/, approximation formulas are given:

For $\dfrac{d}{b} < 2$ $\qquad\qquad R = R_o$ $\qquad\qquad$ (1.21)

$\qquad 2 < \dfrac{d}{b} < 4$ $\qquad\qquad R = R_o\left[1 + \left(\dfrac{d}{5.3b}\right)^4\right]$ $\qquad$ (1.22)

$\qquad \dfrac{d}{b} > 4$ $\qquad\qquad R = R_o\left[\dfrac{d}{4b} + 0.25\right]$ $\qquad$ (1.23)

$\qquad \dfrac{d}{b} > 10$ $\qquad\qquad R = R_o\,\dfrac{d}{4b}$ $\qquad\qquad$ (1.24)

d .... wire diameter

b .... equivalent conducting layer thickness
$\qquad\qquad\qquad\qquad\qquad$ (cf. Eq. 1.25)

$$b = \frac{6.4\ K_1}{\sqrt{f}} \cdot 10^{-2} \qquad |m,\ H_z| \qquad (1.25)$$

The correction factor K_1 is dependent upon the wire material and can be seen from Table 1.2

Table 1.2

material	K_1
silver	1.00
copper	1.03
aluminum	1.37
zinc	1.97
brass	2.2
platinum	2.62

or can be taken directly from Fig. 1.6 in dependence on the frequency.
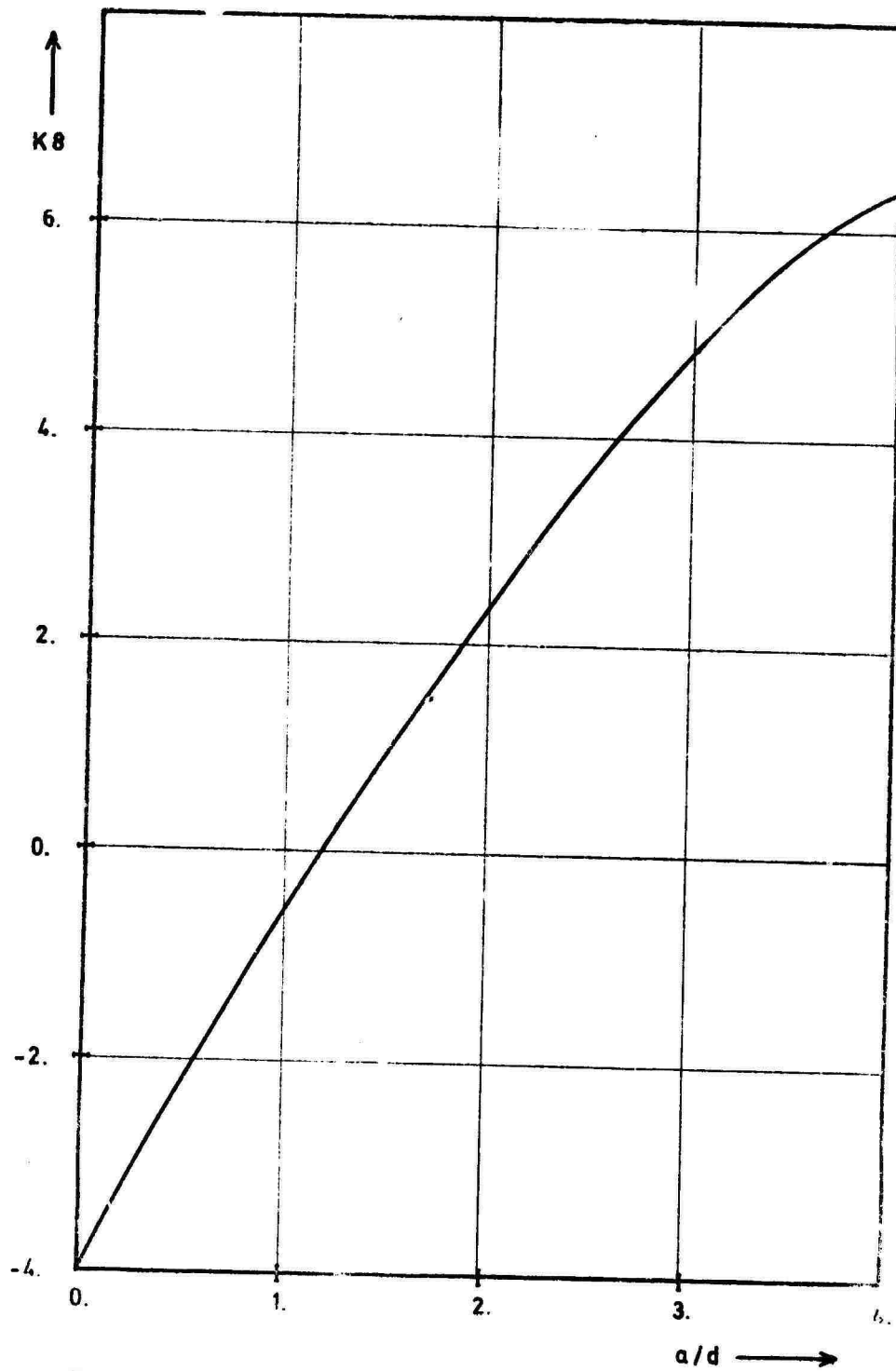
FIG. 1.5   CORRECTION FACTOR K8
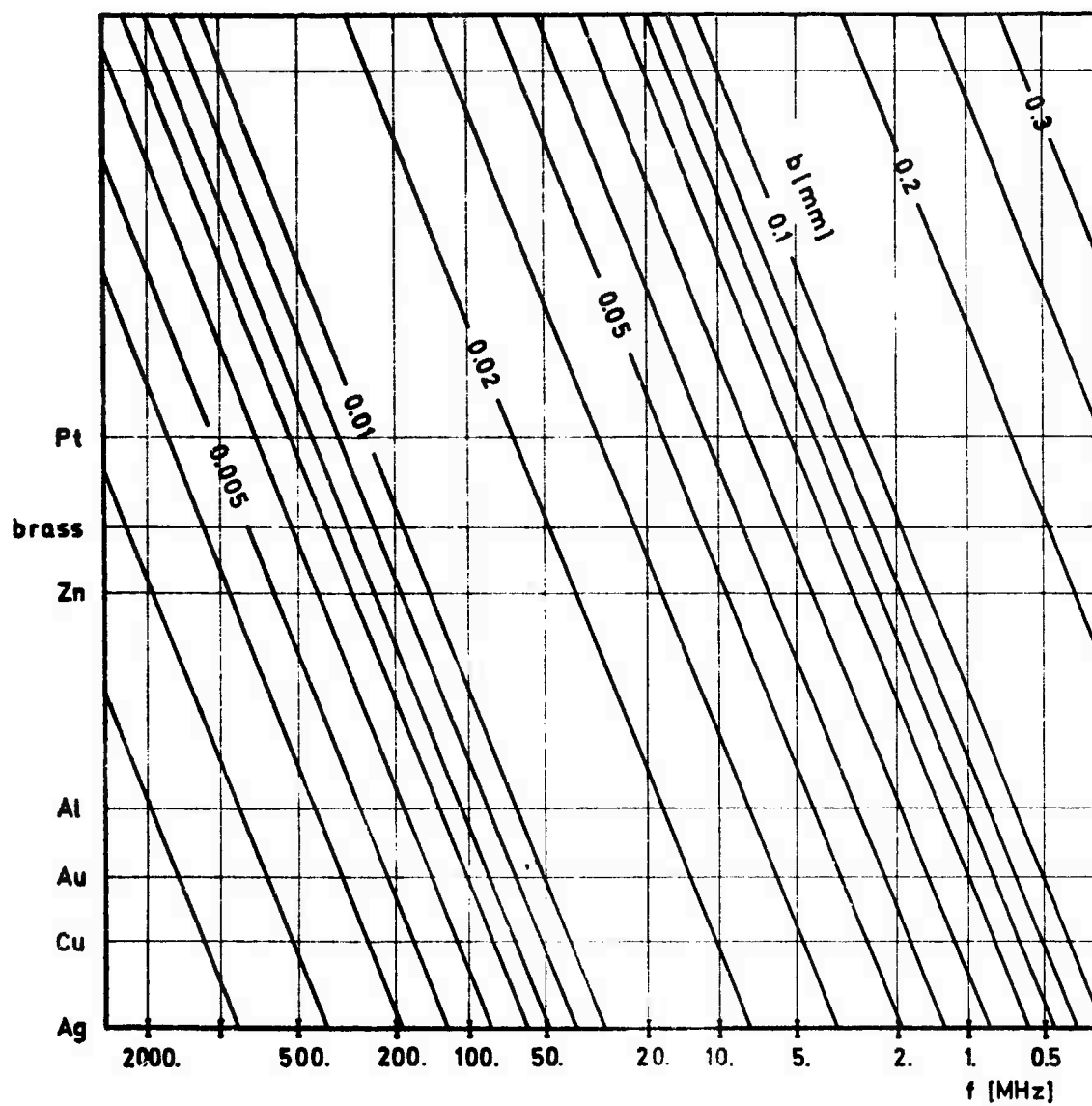
FIG. 1.6

The resistance of a 1 m silver wire in dependence on the frequency and the radius of the wire can be deduced from Fig. 1.7. If we use another wire the effective radius must be divided by the factor K_1.

Proximity effect: If currents are flowing in neighboring wires in same or opposite directions, current displacement occurs in addition to the skin effect on account of the change of magnetic fields according to Fig. 1.8.

same current   opposite current
direction   direction
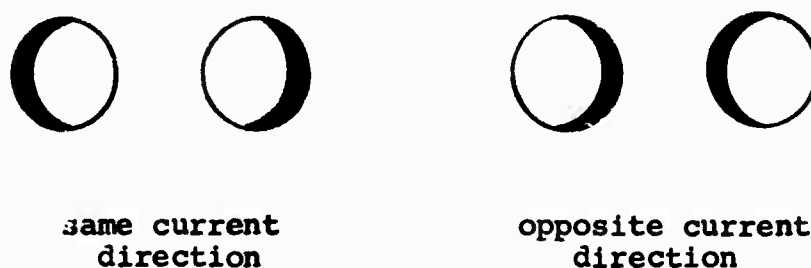
Fig. 1.8: Proximity effect

The hf-resistance of the respective wire is thus increased. By multiplying the hf-resistance by the correction factor K_2 this increase is taken into account. For the case of two parallel wires with circular cross section, K_2 can be taken from Fig. 1.9.

$R_{eddy\ current}$ is caused by the surrounding conductive rock and by the influence of the measuring devices.

If the antenna is surrounded by a second shorted wire with the resistance R_2, $R_{eddy\ current}$ reads

$$R_{eddy\ current} = \omega^2 \frac{M^2}{R_2}$$

(1.26)

M .... mutual induction

for the frequency range up to about 0.5 MHz, i.e., $R_{eddy\ current}$ is increasing proportionally to f^2.

For higher frequencies, the approximation

$$R_{eddy\ current} = R_2 \cdot k^2 \frac{L_1}{L_2} \qquad (1.27)$$

k .... coupling coefficient

is valid, i.e., the increase of eddy-current resistance is only proportional to the increase in R_2 by the skin effect.

$\underline{R_{diel.}}$ consists of losses caused by the capacitive currents in the wire isolation and in the carrier material. For constant current $R_{diel.}$ increases with f^3.

$$R_{diel.} = 0.25 \cdot f^3 \cdot C_L \cdot L^2 \cdot d_C \cdot 10^3 \qquad (1.28)$$
$$|\Omega,\ Hz,\ F,\ H|$$

C_L .... self-capacitance of the antenna
L ..... inductivity of the antenna
d_C .... loss factor of the dielectric

The value of C_L can be seen from Fig. 1.10 (with the same designation as in Fig. 1.4), d_C from tables, e.g. in /4/.

$\underline{R_{radiation}}$ must be considered only with very high frequencies or in the case of antenna dimensions larger than $\lambda/10$ (λ = working wavelength). In /5/ radiation resistances for smaller antennas (capacitive or inductive standard antenna) are quoted:

FIG. 1.7

FIG 1.9

CORRECTION FACTOR K 2
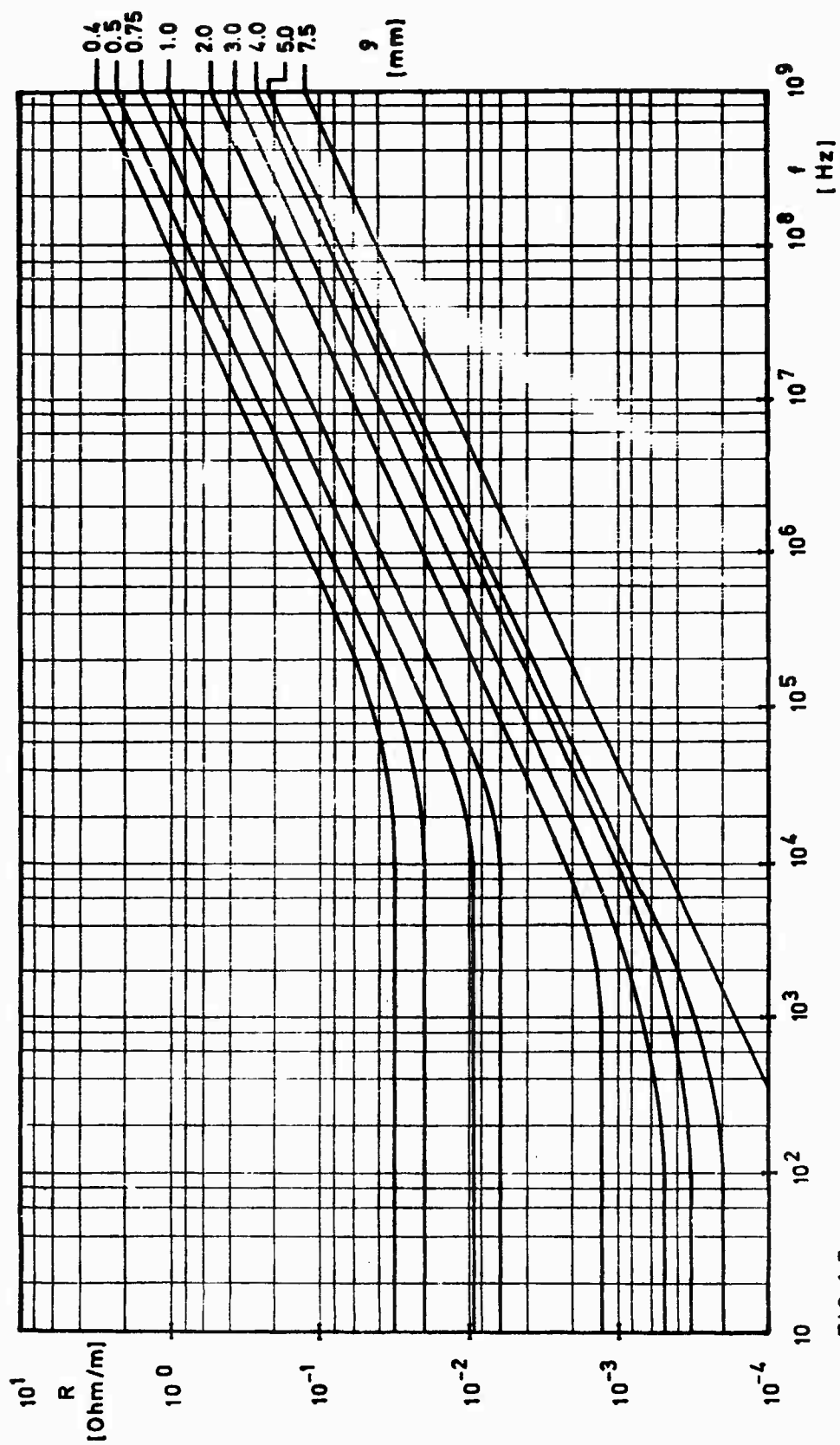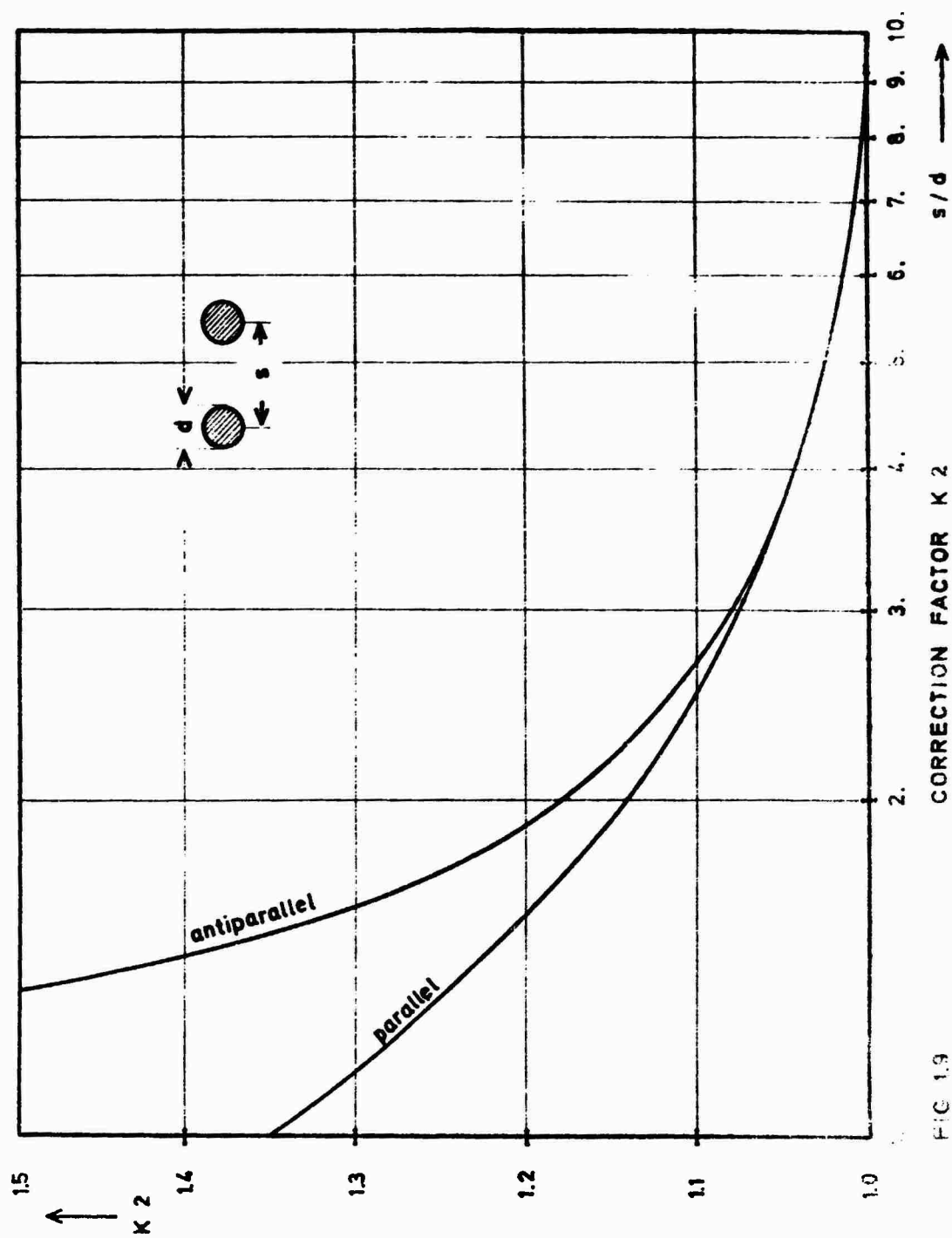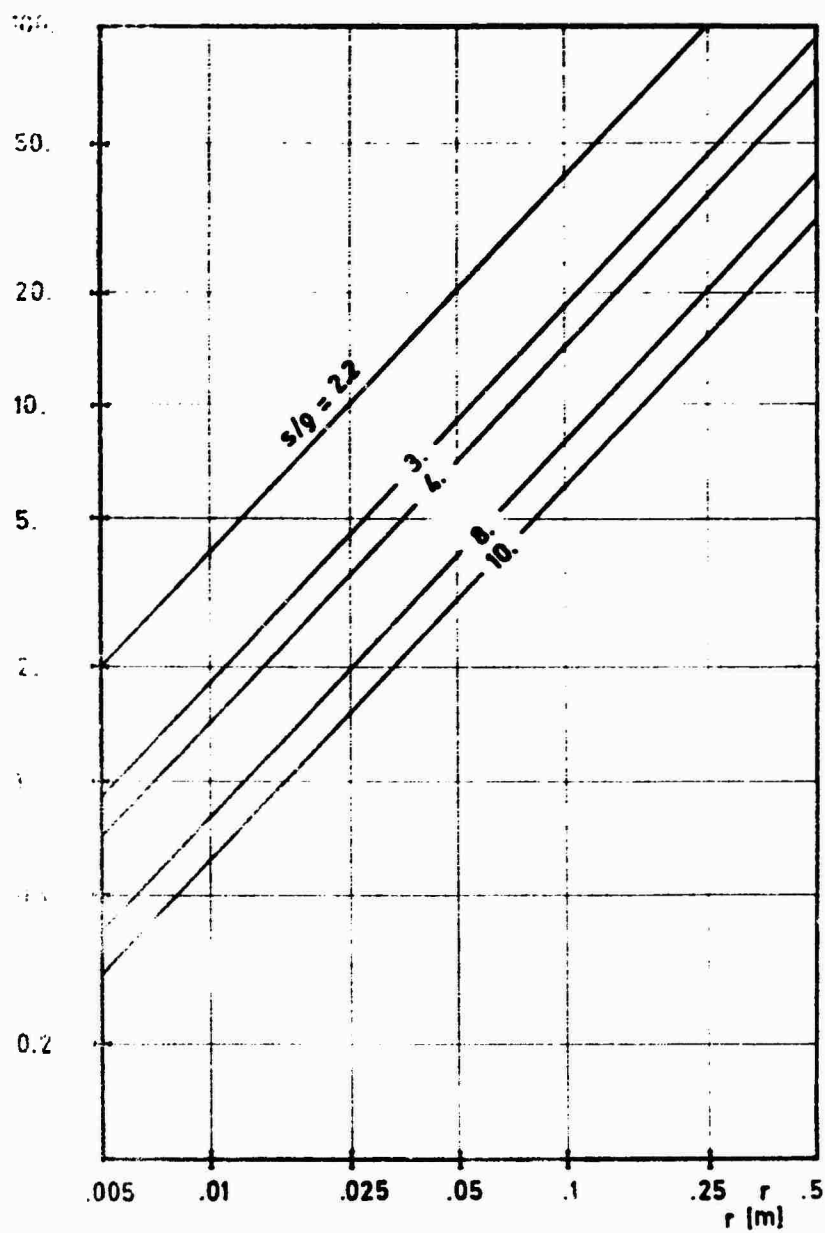
FIG. 1.10

| capacitive antenna | $R_e = 80 \cdot \pi^2 \cdot \left(\frac{1}{\lambda}\right)^2$ | (1.29) |

| inductive antenna | $R_m = 80 \cdot \pi^2 \cdot \left(\frac{n \cdot A}{\lambda^2}\right)^2$ | (1.30) |

λ ..... wavelength

l ..... length of the electric dipole

$n \cdot A$ ... turn area of the magnetic dipole

R_e, R_m . radiation resistances

In every case, however, R_{rad} is essentially (several decimal powers) smaller than R_{wire} and R_{diel}, respectively.

With sufficiently large gallery cavity, $R_{eddy\ current}$ is as well much smaller than R_{wire} and R_{diel} on account of the low conductivity of the surrounding rock and the small dimensions of the used measuring devices.

Capacity C: For the calculation of C, the approximation formula for the static capacity of a symmetric cylindrical antenna has proved useful. According to /6/

$$C = \frac{2\pi\varepsilon_0 \cdot l}{\ln\left(\frac{l}{3r^2}\right)} = \frac{\pi \cdot \varepsilon_0 \cdot l}{\ln\left(\frac{l}{r}\right) - 0.55} = \frac{3.54 \cdot l}{\ln\left(\frac{l}{r}\right) - 0.55} \cdot 10^{-13} \ |F,m|$$

(1.31)

$2l$ .... total length of the antenna

r ..... radius of the cylinder $\qquad 2l > r$

In this simple form the equation is only valid with comparatively narrow windings (as e.g. at H 772, H 1362, H 1136 Cull, H 328 etc.).

C_p is calculated from the parallel connection of the capacity of the feed line and the capacity of the two inner windings:

$$C_p = C_k + C_i$$

According to /3/ the feed-line capacity appears as the capacity of the symmetric two-wire line and reads

$$C_k = \frac{\pi \cdot \varepsilon_0 \cdot \varepsilon_r \cdot 1}{\ln\left(\frac{D}{d}\right) + \sqrt{\frac{D^2}{d^2} - 1}} = \frac{0.121 \cdot \varepsilon_r \cdot 1}{\log\left(\frac{D}{d} + \sqrt{\frac{D^2}{d^2} - 1}\right)} \cdot 10^{-10} \quad |F,m| \tag{1.32}$$

D .... distance between wires

d .... diameter of the wires

1 .... length of the wires

Generally, the cable capacity is given by the manufacturers or can easily be determined by experiment.

The capacity C_i of the two inner windings of the antenna can be calculated according to /3/ as the capacity of two parallel wires of the length 1, of the antenna circumference $2r\pi$, the distance D and the diameter d:

$$C_i = \frac{0.121 \cdot \varepsilon_r \cdot 1}{\log\left(\frac{D}{d} + \sqrt{\frac{D^2}{d^2} - 1}\right)} \cdot 10^{-10} = \frac{0.754 \cdot \varepsilon_r \cdot r}{\log\left(\frac{D}{d} + \sqrt{\frac{D^2}{d^2} - 1}\right)} \cdot 10^{-10} \quad |F,m| \tag{1.33}$$

with ε_r to be determined experimentally on account of the influence of the wire isolation (ε not known with suffi-cient accuracy).

Numerical evaluation of the parameters of the equivalent circuit diagram for the antennas H 1136 Cull, H 328 I, H 328 II:

Table 1.3: Geometrical data

quantity	unit	H 1136 Cull	H 328 I	H 328 II	Remark
n		1136	328	328	
r	m	$1.43 \cdot 10^{-1}$	$5.5 \cdot 10^{-2}$	$5.5 \cdot 10^{-2}$	
s	m	$1.72 \cdot 10^{-3}$	$2.5 \cdot 10^{-3}$	$2.5 \cdot 10^{-3}$	
ρ	m	$0.75 \cdot 10^{-3}$	$5 \cdot 10^{-4}$	$5 \cdot 10^{-4}$	
l	m	0.977	0.41	0.41	loss factor
d_c		$4 \cdot 10^{-3}$	$4 \cdot 10^{-3}$	$4 \cdot 10^{-3}$	of the dielectric carrier material

Table 1.4: Results

quantity	unit	equation	H 1136 Cull	H 328 I	H 328 II
L	H	19, 20	$2.7 \cdot 10^{-2}$	$8.04 \cdot 10^{-4}$	$8.04 \cdot 10^{-4}$
R_{wire}	Ω	24, 25	57	16	16
+ $R_{diel.}$	Ω	28	332	24	24
= R_{total}	Ω		389	40	40
C	F	31	$20.1 \cdot 10^{-12}$	$7.8 \cdot 10^{-12}$	$7.8 \cdot 10^{-12}$
C_p	F	32, 33	$90 \cdot 10^{-12}$	$98 \cdot 10^{-12}$	$1.97 \cdot 10^{-9}$

H 328 II: Same data as for H 328 I, C_p artificially in-
creased by parallelling of a low-induction
ceramic drop capacitor.

The measurements, their evaluation and comparison with the equivalent circuit diagram

The measurements were executed in a larger cavity in the SO-gallery of the mine St. Gertraudi/Tyrol. The following measuring devices were used:

for the frequency range up to 600 kHz:

    selective levelmeter SPM-2, Wandel & Goltermann
    decade R-C-generator TG 66 A, Levell
    three-stage preamplifier, gain 80 dB, 50-1000 kHz,
        transistorized, constructed in the VLF-lab

for the frequency range over 600 kHz:

    L-C-generator, transistorized, constructed in the
        VLF-lab
    selective heterodyne voltmeter 2006, Brüel & Kjaer

for both frequency ranges:

    R-C-L-bridge LE 300/A 1, Hatfield
    frequency counter, type 100A, Monsanto

The values of RE Z (exp) and IM Z (exp) were computed according to the formulas given in /1/ and listed in tables 1.5 to 1.7.

The columns mean from the left to the right:

f	kHz	working frequency
RE Z (exp)	kΩ	real part of impedance calculated from experiment
RE Z (th)	kΩ	real part of impedance calculated from the equivalent circuit diagram
DRE Z		ratio RE Z (exp) / RE Z (th)
IM Z (exp)	kΩ	imaginary part of impedance calculated from experiment
IM Z (th)	kΩ	imaginary part of impedance calculated from the equivalent circuit diagram
DIM Z		ratio IM Z (exp) / IM Z (th)

A graphical representation of the measuring results is shown in Figs. 1.11 to 1.16.

Tab. 1.5

F	RE Z (EXP)	RE Z (TH)	ORE Z	IM Z (EXP)	IM Z (TH)	DIM Z
50.0	0.1327E-...	0.1648E+01	124.16	-0.2893E+02	-0.2687E+02	0.93
100.0	0.1757E...	0.5574E+00	31.73	-0.1399E+02	-0.1324E+02	0.95
120.0	0.2114...1	0.4642E+00	21.96	-0.1135E+02	-0.1076E+02	0.95
150.0	0.31..E-01	0.3358E+00	10.72	-0.8495E+01	-0.8086E+01	0....
180.0	0....E-01	0.2392E+00	4.12	-0.6088E+01	-0.5965E+01	0....
200.0	0....E+00	0.1775E+00	1.60	-0.4190E+01	-0.3971E+01	0.92
210.0	0....66E+00	0.1837E+00	1.04	-0.2836E+01	-0.2600E+01	0.87
215.0	0....361E+00	0.2224E+00	0.94	-0.1918E+01	-0.1652E+01	0.47
218.	0.2886E+00	0.2673E+00	0.93	-0.1236E+01	-0.8761E+00	
2 0.	0.3345E+00	0.3740E+00	1.12	-0.7039E+00	-0.2171E+00	
22.0	0.3930E+00	0.5025E+00	1.28	-0.3990E-01	0.8075E+00	
240.0	0.8436E-01	0.9761E+01	1.16	0.25336E+02	0.1855E+02	0.56
250.0	0.5707E-01	0.6202E+01	1.09	-0.3314E+02	-0.2280E+02	0.79
300.0	0.4775E-01	0.1954E-01	0.41	-0.7928E+01	-0.4421E+01	0.81
350.0	0.1108E-01	0.1770E+00	15.97	-0.5892E+01	-0.4681E+01	0.82
400.0	0.4340E-02	0.1837E+00	42.33	-0.4881E+01	-0.3970E+01	0.74
450.0	0.2140E-02	0.1464E+00	68.40	-0.4217E+01	-0.3461E+01	
500.0	0.1204E-02	0.1389E+00	115.36	-0.3731E+01	-0.2761E+01	

Tab. 1.6

F	RE Z (EXP)	RE Z (TH)	DRE Z	IM Z (EXP)	IM Z (TH)	DIM Z
1000.0	0.402?E-03	0.15A3E-02	3.93	-0.1466E+01	-0.3979E+01	2.71
1500.0	0.9?.?E-03	0.7036E-03	0.71	-0.9181E+00	-0.2653E+01	2.89
1800.0	0.?.?2E-02	0.1909E-03	0.06	-0.65227E+00	-0.1382E+01	2.12
1900.0	0.?922E-02	0.6744E-04	0.01	-0.51133E+00	-0.8212E+00	1.60
1950.0	0.?173E-01	0.1167E-01	0.99	-0.4001E+00	-0.4182E+00	1.05
2000.0	0.2462E-01	0.2419E-01	0.98	-0.2014E+00	-0.2544E+00	1.26
2020.0	0.3684E-01	0.3653E-01	0.99	-0.649AE-01	-0.7487E-01	1.15
2030.0	0.4676E-01	0.4676E-01	1.00	-0.2808E-01	0.3435E-01	1.22
2040.0	0.6138E-01	0.5043E-01	0.82	0.1474E+00	0.1810E+00	1.2?
2050.0	0.8424E-01	0.5072E-01	0.60	0.3067E+00	0.3224E+00	1.05
2080.0	0.3618E+00	0.5383E-01	0.15	0.1440E+01	0.8970E+00	0.62
2100.0	0.3880E+01	0.2836E-01	0.01	0.5407E+01	0.1684E+01	0.31
2200.0	0.2968E-01	0.5815E-01	1.96	-0.1346E+01	-0.2411E+02	17.92
2500.0	0.1454E-02	0.3958E-03	0.27	-0.7676E+00	-0.1989E+01	2.59
3000.0	0.2292E-03	0.2171E-01	94.72	-0.5800E+00	-0.1473E+01	2.54
4000.0	0.3567E-04	0.9894E-02	277.37	-0.4172E+00	-0.9946E+00	2.38

Tab. 1.7

F	RE Z (EXP)	RE Z (TH)	DRE Z	IM Z (EXP)	IM Z (TH)	DIM Z
1500.0	0.3342E-05	0.1441E-02	431.12	-0.5323E-01	-0.8486E-01	1.59
1800.0	0.1499E-04	0.1478E-02	98.61	-0.4392E-01	-0.6546E-01	1.49
1900.0	0.4424E-04	0.1213E-02	27.42	-0.4104E-01	-0.5981E-01	1.46
1950.0	0.1126E-03	0.1138E-02	10.11	-0.3921E-01	-0.5439E-01	1.39
2000.0	0.7361E-03	0.1923E-02	2.61	-0.3509E-01	-0.4202E-01	1.20
2020.0	0.5069E-02	0.8723E-02	1.72	-0.2724E-01	-0.2511E-01	0.92
2030.0	0.3434E-01	0.5318E-01	1.55	-0.3171E-01	0.6593E-02	-0.21
2040.0	0.7071E-02	0.3920E-01	5.54	-0.5374E-01	-0.1121E+00	2.09
2050.0	0.1858E-02	0.8138E-02	4.38	-0.4719E-01	-0.8178E-01	1.73
2100.0	0.1441E-03	0.1246E-02	8.65	-0.4056E-01	-0.6313E-01	1.56
2200.0	0.2297E-04	0.2429E-03	10.57	-0.3745E-01	-0.5399E-01	1.44
2500.0	0.2602E-05	0.1453E-06	0.06	-0.3247E-01	-0.3812E-01	1.17
3000.0	0.4944E-06	0.7402E-07	0.15	-0.2694E-01	-0.2721E-01	1.01
4000.0	0.8332E-07	0.1759E-07	0.21	-0.2016E-01	-0.1326E-01	0.66
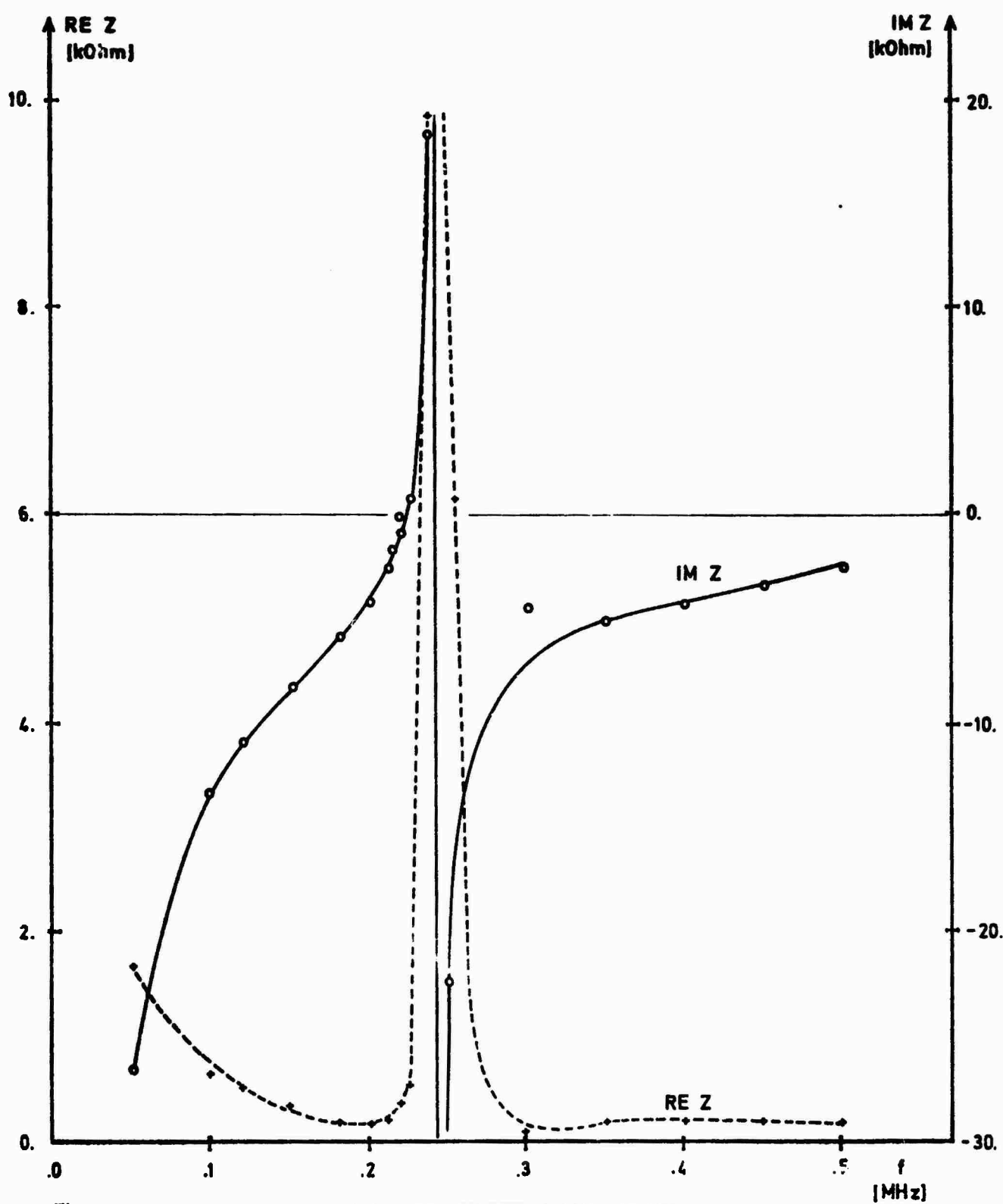
Fig. 1.11   H 1136 CuLL: EXPERIMENTAL VALUES
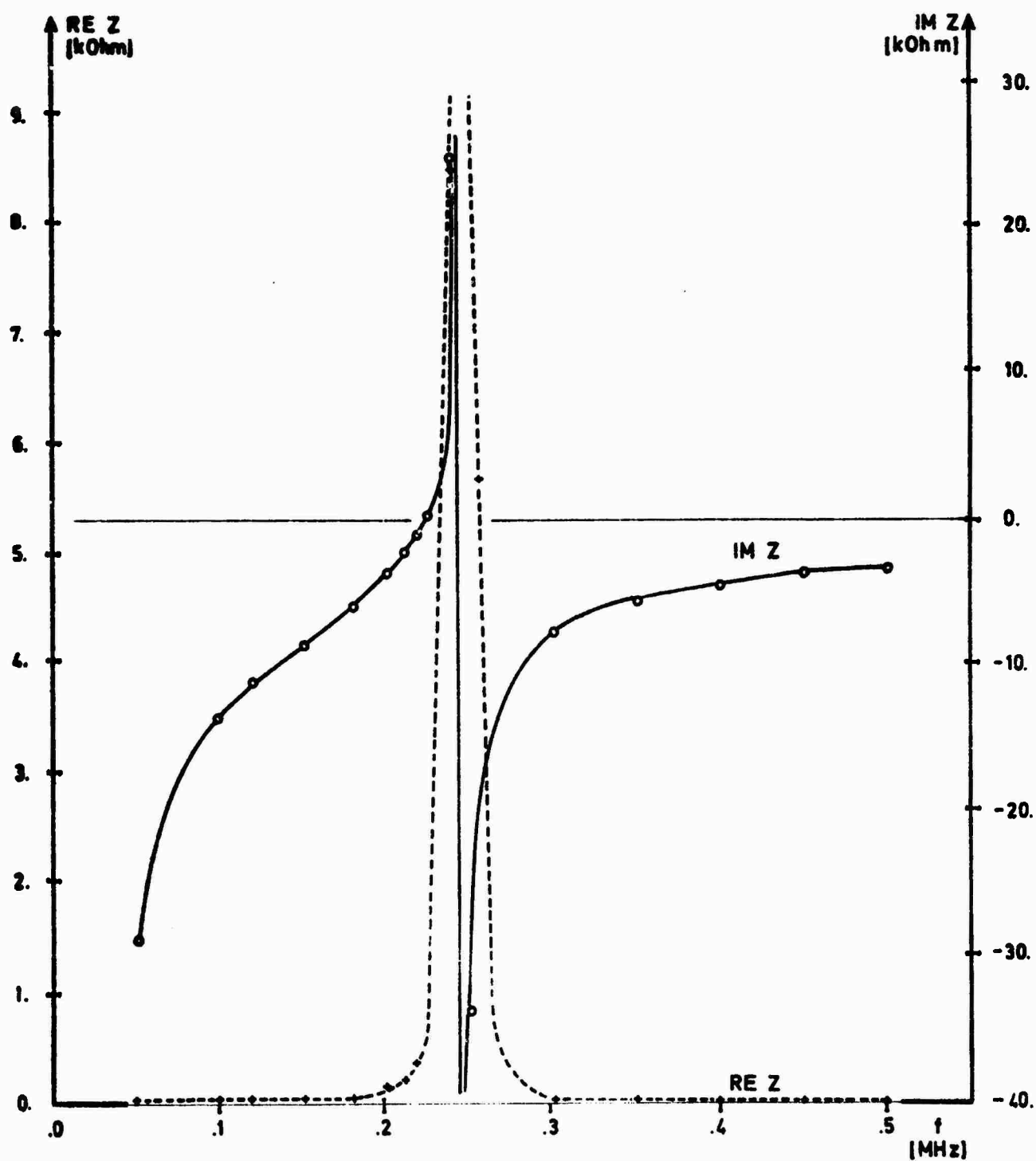
Fig. 1.12   H 1136 CuLL : THEORETICAL VALUES
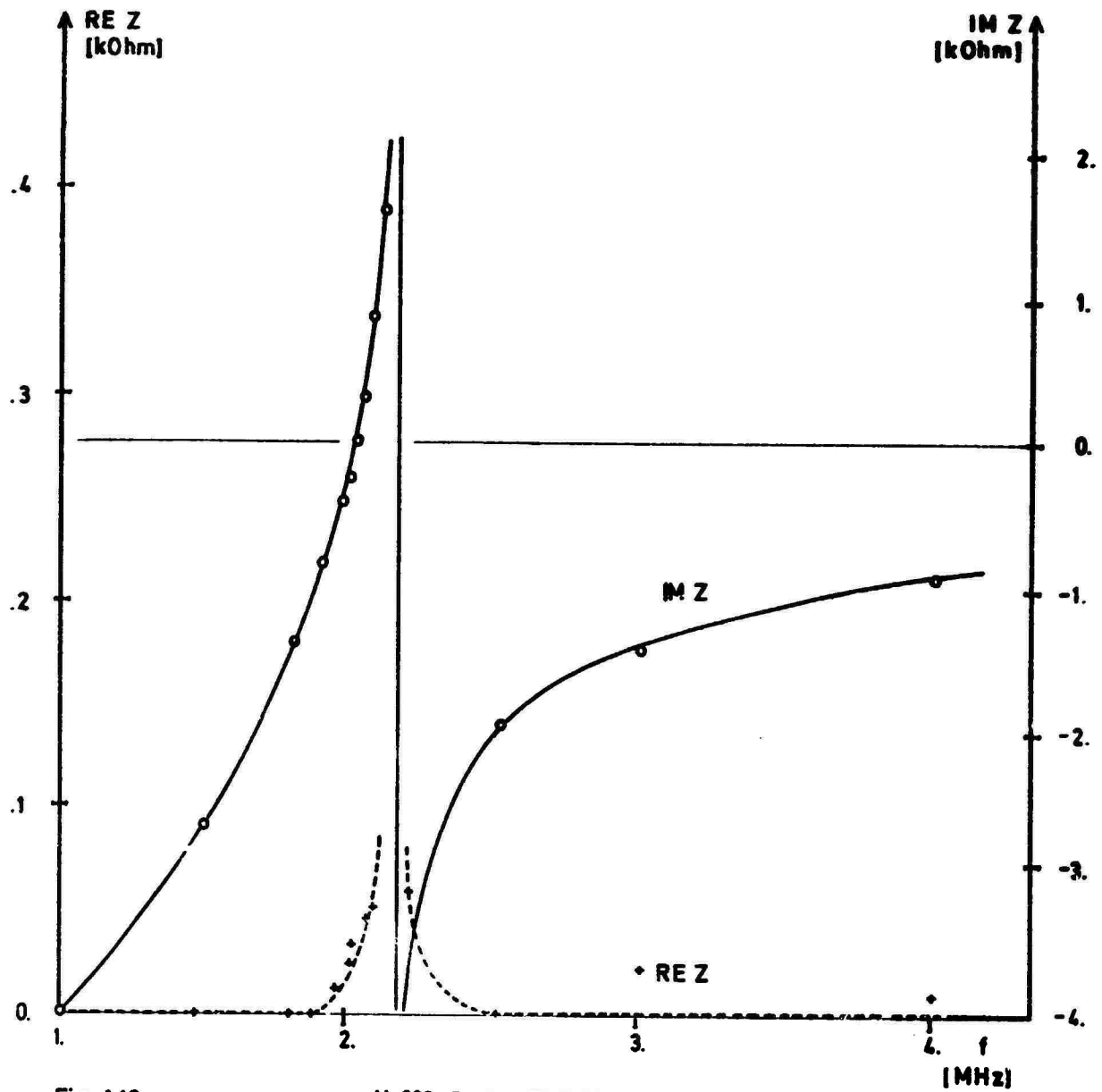
Fig. 1.13   H 328 Test : EXPERIMENTAL VALUES I

Fig. 1.14   H 328 Test : THEORETICAL VALUES 1
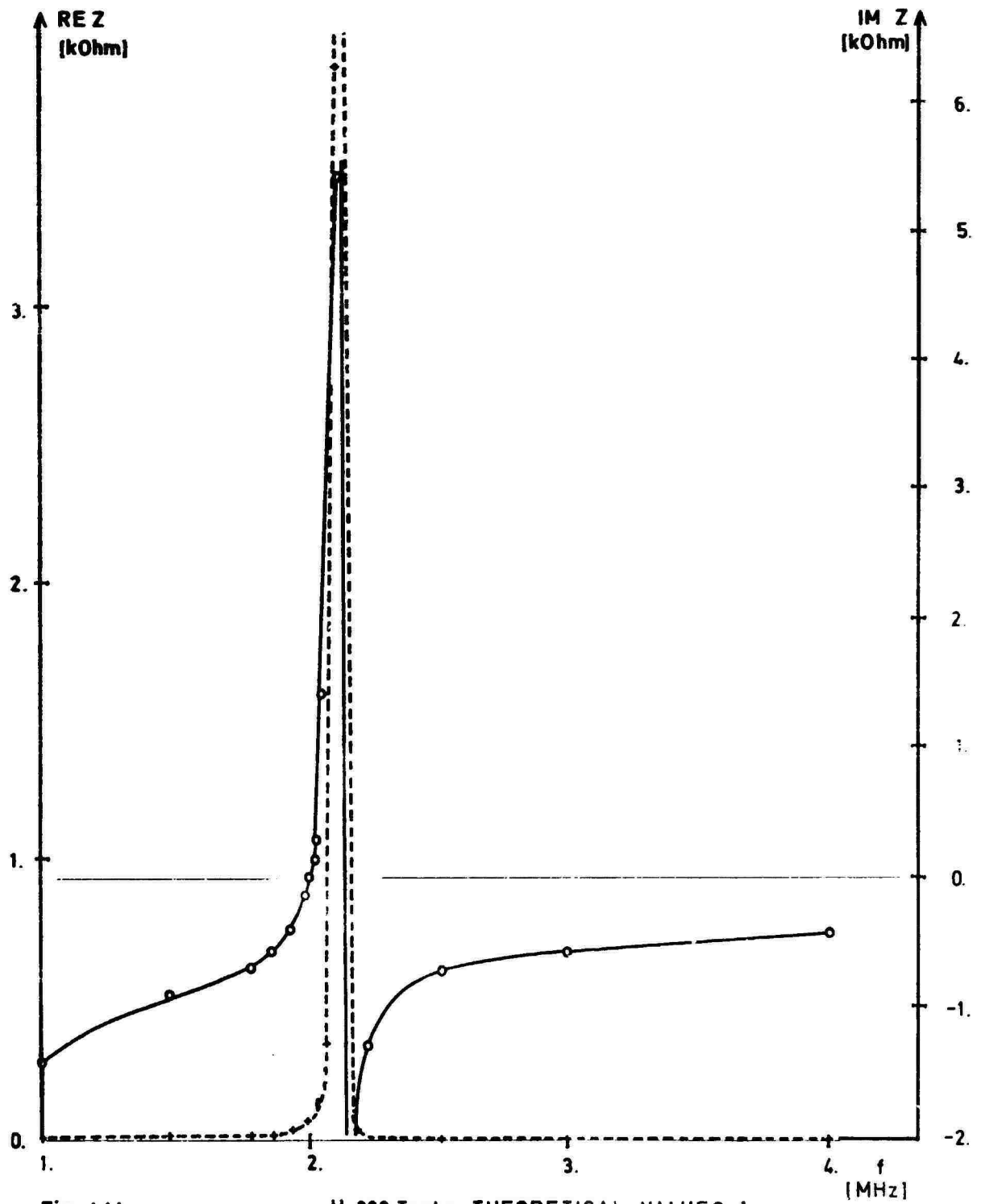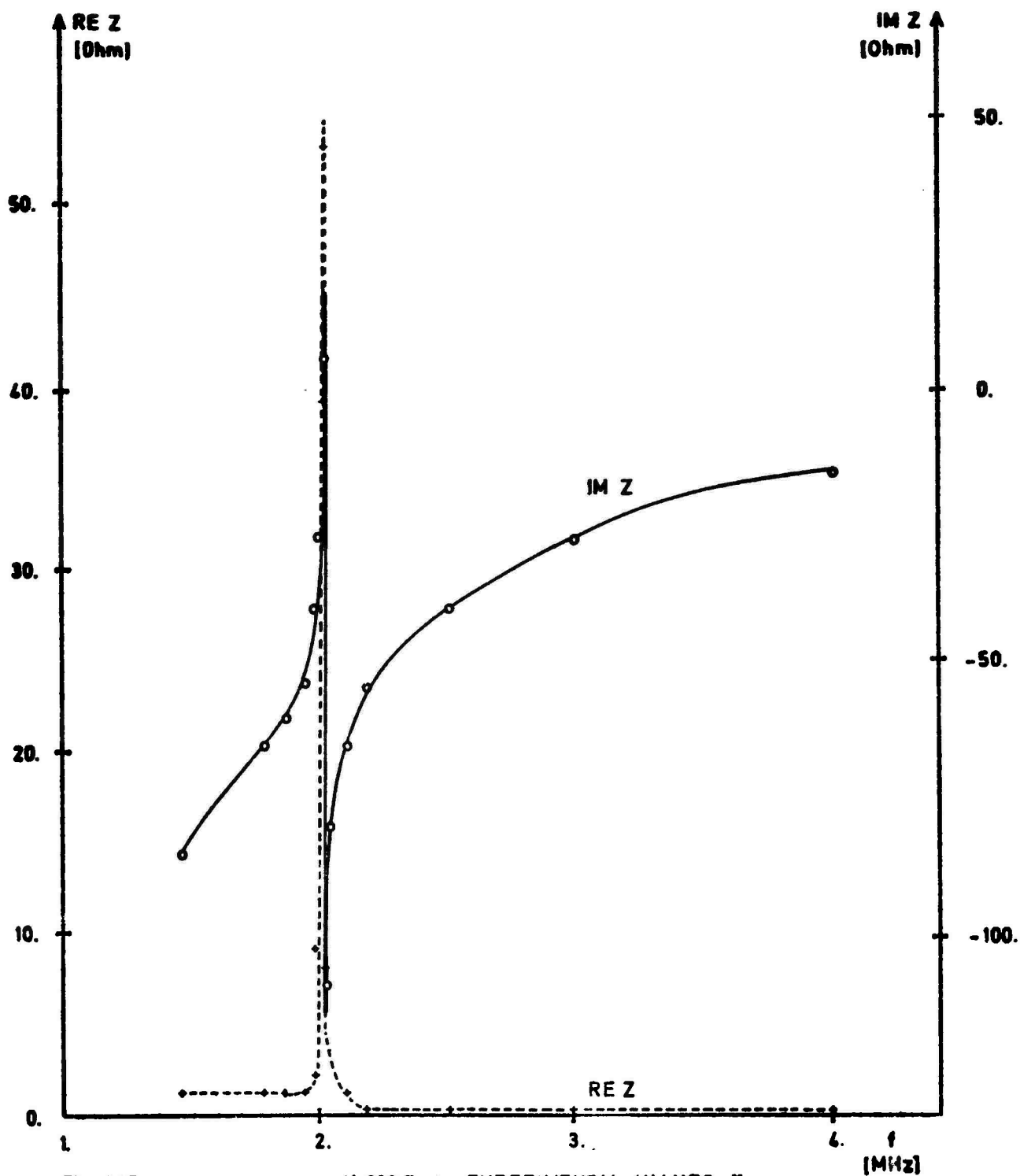
Fig. 1.15   H 328 Test : EXPERIMENTAL VALUES II
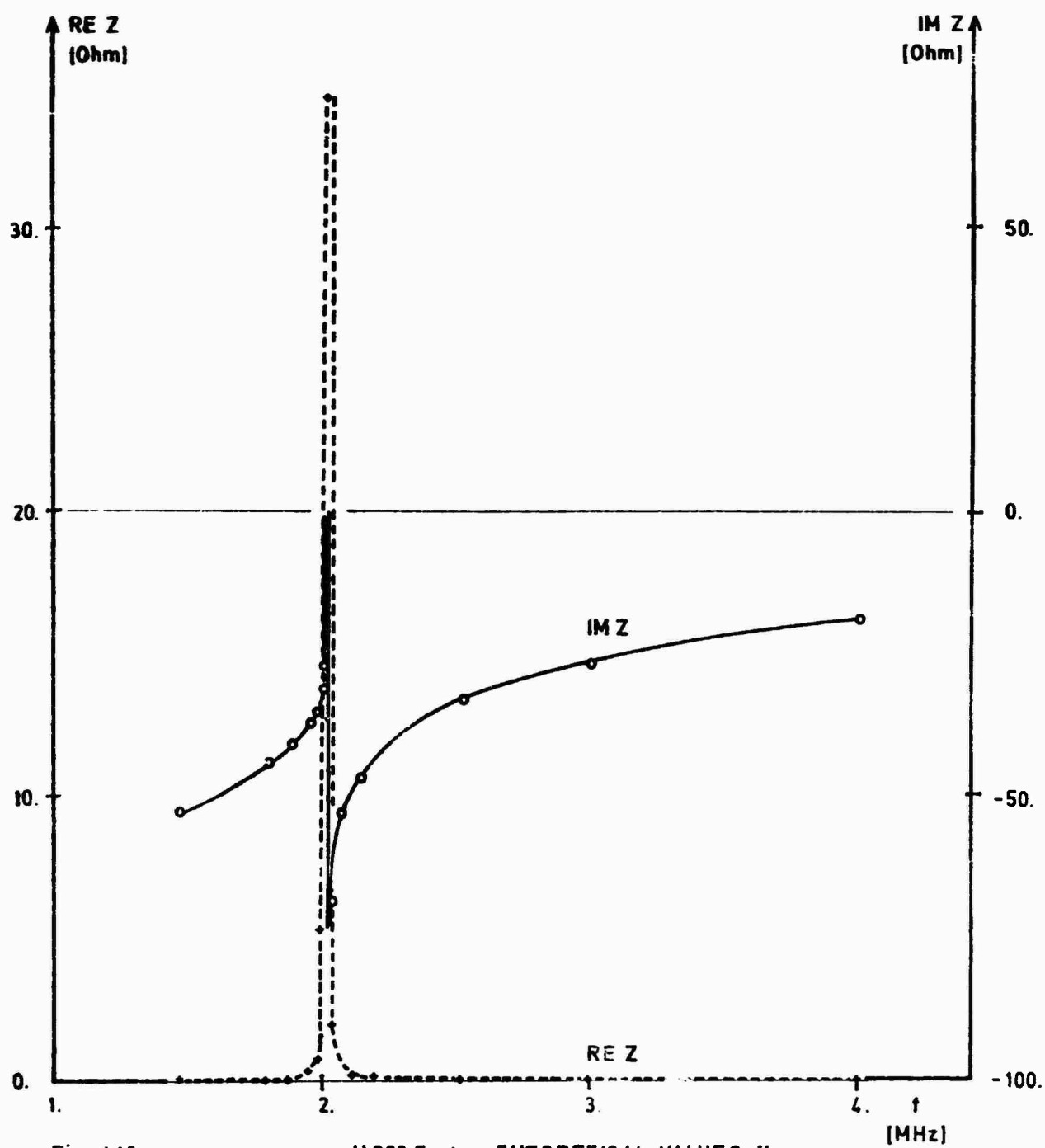
Fig. 1.16   H 328 Test :   THEORETICAL VALUES II

Discussion of results

The deviations still appearing between experiment and theory can be explained on account of the following considerations:

1. The equivalent circuit diagram is calculated with a constant resistance R_{total} which, however, changes with frequency (skin-effect, dielectric losses). The influence of the surrounding medium on the eddy-current resistance is virtually incalculable.

2. Due to the high humidity in the mine the parameters R_{diel} and C change in a way not yet investigated (measurements in the mine have, however, among others the advantage of an essentially lower noise level!).

3. The parameters L, R, C, C_p cannot be calculated with the required accuracy (approximation formulas) because there are quantities (e.g. ε) that are not known exactly enough.

4. The calculation of RE Z (exp), IN Z (exp) is subject to an error of measurement, yet not exceeding 10 %.

The equivalent circuit diagram gives, however, a good interpretation of some effects, that have not been able to be cleared satisfactorily up to now:

1. In the equations of /1/ C_i is contained in the calculation of the series resonance frequency. This is, however, in variance with present experiments, where the decrease of C_i by raising the distance between the two inner windings has no influence on the series resonance. The equivalent circuit diagram shows definitely that C_i is only affecting the parallel resonance. This is proved by the experiment with the antenna H 328 II, with C_i

being artificially increased by parallelling a capacitor.
The series resonance frequency remained constant whereas
the parallel resonance approached the series resonance.

2. Body effect: The small static capacity C is essen-
tially changed (increase of ϵ_r) by approaching a hand
especially at the two ends of the antenna, whereas it is
relatively insensitive in the middle.

3. Influence of humidity: Water vapour deposits on the
antenna on account of the high humidity thus influencing
both loss resistance and capacity C. This gives a good
explanation for the difficulties occurring with earlier
experiments using wood as carrier material. Water-re-
pellent materials such as epoxy, PVC etc. proved more
favorable.

Finally the qualitative agreement of the impedance curve
in experiment and theory can be regarded as best proof
for the validity of the equivalent circuit diagram which,
however, holds only in the range of the first (deepest)
series and parallel resonances. At higher frequencies
additional effects of the individual windings occur and
the simple model described here fails.

Considerations on the efficiency of the antennas in air

According to /7/, the distant field of a small self-
resonant helix with many windings may be regarded as a
combination of an electric with a magnetic dipole. The
length of the helix corresponds to the length of the
electric dipole, the turn area corresponds to the
magnetic dipole $n \cdot A = n \cdot r^2 \cdot \pi$.

For these dipoles the efficiency can be calculated with
given radiation frequency (here the first resonance fre-
quency) according to /5/:

$$\eta = \frac{P_{radiation}}{P_{rad} + P_{loss}} = \frac{I^2 R_{radiation}}{I^2 (R_{rad} + R_{loss})} \qquad (1.34)$$

As mentioned already the radiation resistance is smaller than the loss resistance by several decimal periods, so that R_{rad} can be neglected in the denominator:

$$\eta = \frac{I^2 R_{rad}}{I^2 R_{loss}} = \frac{R_{rad}}{R_{loss}} = \frac{P_{rad}}{P_{loss}} \qquad (1.35)$$

R_{rad} can be calculated according to Eqs. (1.29) and (1.30). Eqs. (1.34) and (1.35) are only valid with antenna dimensions $\ll \lambda$ (which is certainly the case for the antennas described). Table 1.7 gives a survey of these calculations for the antennas H 1136 Cull, H 328, and H 1136 in water.

Table 1.7

	R_{loss} Ω	R_e	η dB	R_m	η dB	f_{res} kHz
H 1136 Cull	400	$1.6 \cdot 10^{-3}$	-74	$40 \cdot 10^{-6}$	-70	220
H 328	40	0.24	-22	$5.6 \cdot 10^{-4}$	-48	2020
H 1136 Cull in water	35	$4.4 \cdot 10^{-8}$	-71	$2.8 \cdot 10^{-6}$	-89	1.1

Discussion: Antennas with a relatively low resonance frequency in air (e.g. H 1136, H 772) show a decrease of resonance frequency caused by a narrower winding and thus increased inductance. As regards efficiency these "inductive" antennas are by far less favorable than "capacitive" antennas as is shown in the table. Thus, for any application we have to make a compromise between antenna efficiency and favorable frequency for the transmission in the dissipative medium, which is thoroughly dealt with in /8/.

Propagation measurements

Diagram 1.17 shows the characteristic course of a propagation measurement. In this case, antenna H 1136 Cull was operated in water in the mine St. Gertraudi.

Curve $\underline{a}$ shows the curvature of field strength in dependence on the distance. The antenna was situated in the water-filled "Mabuse-gallery", measurements were executed along the west-gallery.

Measuring data of this experiment:
    frequency f = 1.1 kHz
    antenna current I = 1 A
    applied power P_i = 100 W

Transmission was detected unobjectably in a distance of 1 km with a signal-to-noise-ratio of 7 dB. The components B_r, B_ϕ could be determined. B_θ vanished in the noise at greater distances.
This result indicates the predomination of the part of the electric dipole.

Stimulated by this experiment the same antenna was once more fed in water, this time, however, in a lower water-filled gallery near the VLF-laboratory. For this experiment, the VLF-transmitter (Savage) in the lab was used.

Measuring data of the experiment:
    frequency f = 1.1 kHz
    antenna current I = 3.5 A
    applied power P_i = 700 W

The power could not be increased on account of sparkovers at the ends of the antenna that would surely have influenced the measurement.
Surprisingly, the signal was to be detected unobjectably even in a distance of more than 7 km on the earth surface.
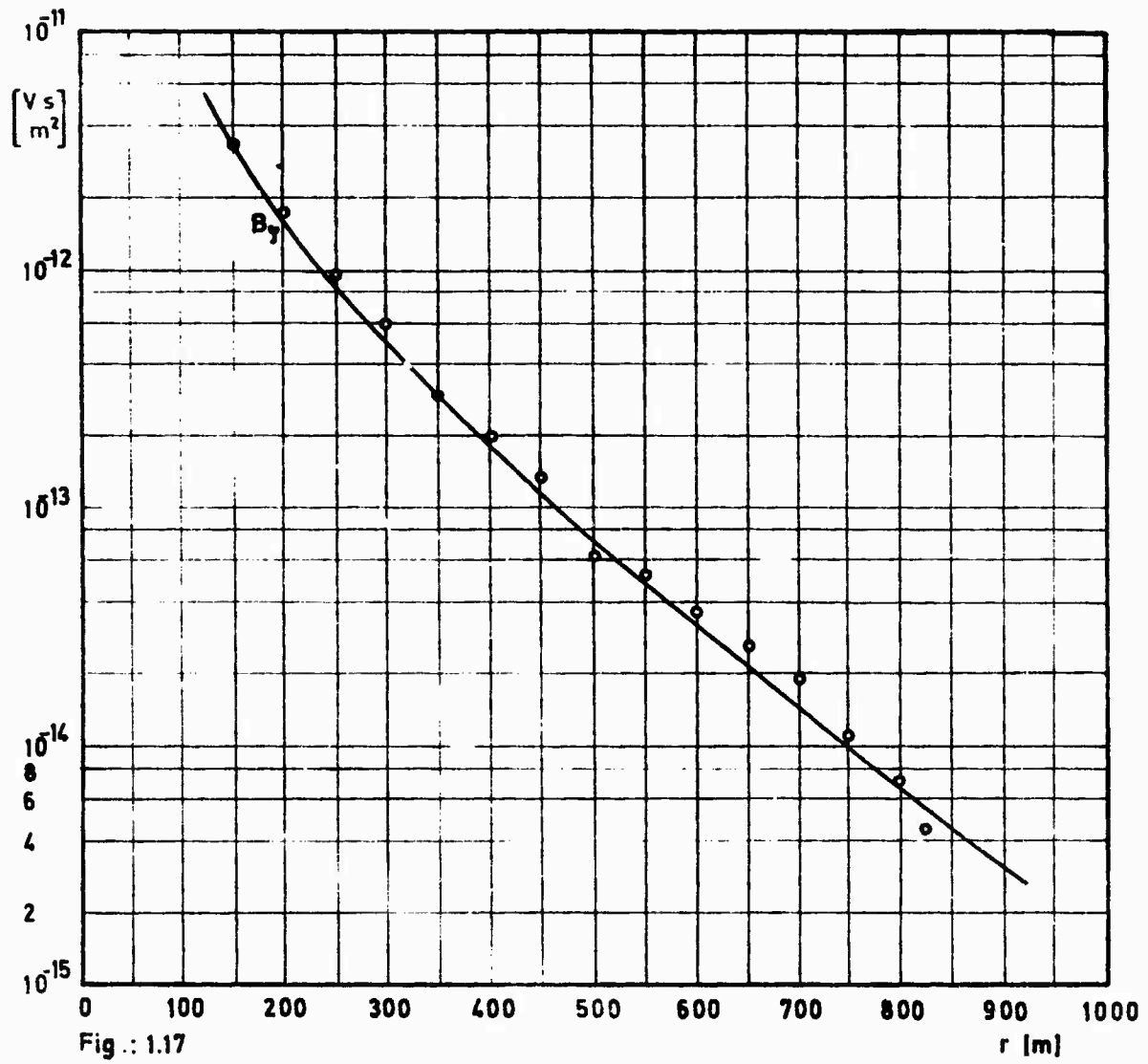
Fig.: 1.17

CHAPTER 2

MEASURING THE ROTARY FIELD ELLIPSE BY A
FERRITE ROD ANTENNA - "PEDAL LOCUS CURVE"

In the magnetic alternating field a coil (frame) receives
an e.m.f. being proportional to the area A, the number of
turns n and the change velocity of the magnetic induc-
tion B, the latter being proportional to the projection
of the field direction to the frame axis. The desired
high e.m.f. is reached by a high μ of the ferrite mate-
rial, filled into the coil and A. Technical problems re-
strict the two values. Comprehensive investigations /9/
showed the use of a ferrite rod to be optimal with the
dimensions given. This ferrite rod coaxial to the re-
ceiving coil represents the coil axis and thereby the
direction of the receiving antenna for all further con-
siderations.

An alternating field constant in space induces an e.m.f.
in the ferrite antenna according to

$$e.m.f._{ind.}(t) = K \cdot B \sin\omega t \cos\psi \qquad (2.1)$$

K ... calibration factor, specific for electric and
geometric properties of the ferrite antenna

ψ ... angle between ferrite rod and field direction

If the field consists not only of one vector, but is an
elliptical field, then the projection of the instantaneous
field vector on the antenna direction is a direct measure
for the e.m.f.

2.1 Two-dimensional case

At first, the three-dimensional problem is confined to
a two-dimensional one by moving the antenna only in the
plane of the rotary field ellipse. Let the x-y plane of
the coordinate system coincide with this plane.

It could be shown in /11/ that always only one planar
ellipse will result, even if more than two components
with different phase and direction in space are super-
posed.

On account of the continuous change of direction and
value of the field vector the instantaneous vector in the
antenna direction generally does **not** yield the maximum
amount of projection and thus maximum e.m.f. In Fig. 2.1a
the maximum e.m.f. is plotted as radius for each position
of angle ψ of the receiving antenna (dashed curve "pedal
locus curve") and reduced to the same scale the rotary
field ellipse is plotted. It can be realized that always
that point T of the ellipse produces one point of the
pedal locus curve F in which a normal to the antenna di-
rection contacts the ellipse.

In vector form the analytic description of this pedal
locus curve measured in earlier studies /10,11/ reads as
follows:

$$\vec{X}_F = \sqrt{a^2\cos^2\psi + b^2\sin^2\psi}\begin{pmatrix} \cos\psi \\ \sin\psi \end{pmatrix} \qquad (2.2)$$

being the basis for further calculations.

Special cases:

For a = b (circular polarization)

$$\vec{X}_F = a\begin{pmatrix} \cos\psi \\ \sin\psi \end{pmatrix}$$
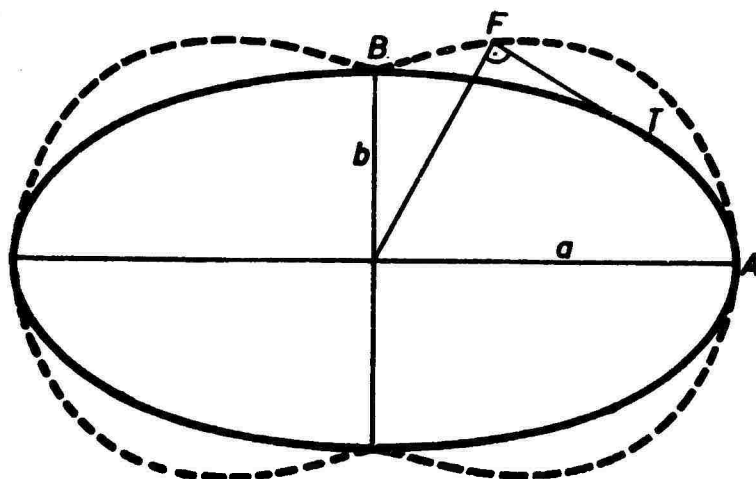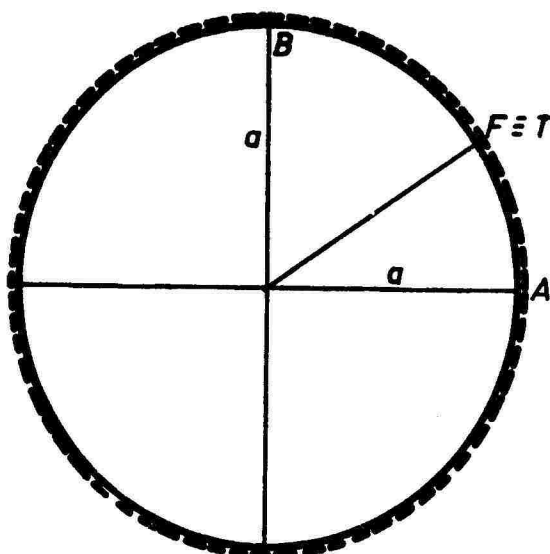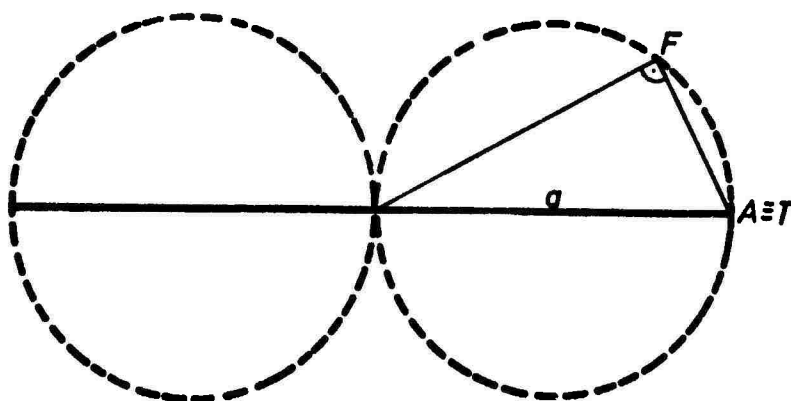
Fig . 2.1

or without parameter

$$x^2 + y^2 = a^2 \quad \text{(circle is counted twice)}$$

The receiving e.m.f. is independent on the direction (see Fig. 2.1b).

For b = 0 (linear polarization)

$$\vec{X}_F = a \cos\psi \begin{pmatrix} \cos\psi \\ \sin\psi \end{pmatrix}$$

or without parameter

$$x^2 + y^2 \pm ax = 0$$

and

$$(x \pm \frac{a}{2})^2 + y^2 = \frac{a^2}{4} \quad \text{(2 circles shifted by } \pm a/2 \text{ including the origin)}$$

in the standard form, resp., reflecting the figure-eight pattern of the pure cosine-dependency (see Fig. 2.1c).

2.2 Phase relation

Assuming linear polarization (only one vector instead of the rotary field ellipse) it becomes evident that the induced voltage U_{ind} is in phase with the alternating field, independently of the angle ψ between field vector and antenna direction (cf. Fig. 2.1c). If there exists a rotary field ellipse, each rotation of the instantaneous vector at the same time means a continuous phase rotation on 2π. With the phase position of the major axis of ellipse as zero point we measure a phase for each antenna direction corresponding precisely to that instantaneous vector that induces maximum amplitude into the antenna. With the exception of the case when the antenna is oriented in the main

axes of the ellipse the phase of the e.m.f. in the antenna
is not identical with the phase of the instantaneous vector
in antenna direction.

Corresponding to the definition of the pedal locus curve,
the phase-determining contact points T (cf. Fig. 2.1a) of
the tangent lines normal to the antenna move close together
near the major axis but move away from the minor axis.
This means that the phase of a dominates in quite a large
angular sector around A. In the neighborhood of B, how-
ever, the phase position changes much more than in A even
at the same change of space angle. This is of great im-
portance for the phase measurement described later on: the
phase errors caused by errors of angular adjustment are
lowest at maximum amplitude.

2.3 Technology of measurement

For measuring the rotary field ellipse, a ferrite antenna
with Cardanic suspension is used. Fig. 2.2 shows the gonio-
meter that had been used earlier and is described in /10/.
This special construction allows to turn the top-most
plane C (on which the ferrite rod is pivoted) into any
direction. The scale has a reading accuracy of 1/2 degree.

If the position of the ellipse plane is known, e.g. let
it be horizontal, a and b are comparatively easy to measure.
The top-most plane of the goniometer is adjusted in the
direction of the ellipse plane and the minimum and maximum
voltages are measured. For determining the directions of
a and b, "minimum" adjustment (= b) is preferred, yielding
higher accuracy (cf. Fig. 2.1a).

It is much more difficult to measure the rotary field
ellipse if the latter is oriented arbitrarily in space,
orientation being unknown.

There are five independent, unknown quantities to be determined:

Orientation of ellipse plane in space	2 angles
Orientation of the major (or minor) axis in the ellipse plane	1 angle
Size of axes	2 voltages

In /10/, two different methods were developed for measuring these quantities by means of the goniometer.

Assumption for method 1: When rotating the ferrite rod in a plane arbitrarily inclined to the ellipse the minimum reception voltage always occurs in the plane normal to $\underline{a}$, i.e., the plane given by the z-axis and the minor axis b. Proceeding on this assumption the 5 desired quantities can be measured as follows in 5 definite steps (cf. Fig. 2.2).

1. Starting position: plane A horizontal, plane B in northern direction $\Longrightarrow \alpha = 0^{\circ}$, $\gamma = 0^{\circ}$, ferrite rod in plane B

2. $\beta = 0^{\circ}$, $\gamma = 90^{\circ}$, turn α as far as $U_{ind} = $ min; fix $\underline{\alpha}$

3. $\gamma = 0^{\circ}$, turn β as far as $U_{ind} = $ min; fix $\underline{\beta}$

4. Turn γ as far as $U_{ind} = $ min $\Longrightarrow U_3$, $\underline{\gamma}$
   The angles α, β, γ resulting therefrom are listed.

5. $\gamma \pm 90^{\circ}$, $U_{ind} \Longrightarrow \underline{U_2}$

6. $\gamma = 0^{\circ}$, $\beta \pm 90^{\circ}$, $U_{ind} \Longrightarrow \underline{U_1}$

U_1 ... proportional to major axis a

U_2 ... proportional to minor axis b

U_3 ... should be zero (noise level)

A correction of the angles α or β for an accurate adjustment of U_3 can be done after step 4. The minimum voltage U_3 must be as small as possible compared to U_1 thereby constituting a measure for the accuracy of the angular measurement.

As is shown in the following calculation, the basic
assumption for method 1 only yields an approximation
that is fulfilled the better the narrower the allipse,
i.e. the higher the rat:o a/b and the smaller the incli-
nation of the ellipse plane to the horizontal one from
which the measurement starts.

Method 2 is based on the fact that there is always one
space direction where an absolute minimum of reception
voltage can be measured: the normal to the ellipse
(z-direction) which is reached within several steps of
asymptotic adjustment. If the normal to the ellipse and
thus the position of the ellipse plane is determined,
subsequent measurements are performed as described earlier.

Method 2 is always successive except for b = 0 and will
be preferred in such cases where method 1 delivers in-
accurate results.

With method 1 being technologically much more favorable
(5 definite steps of adjustment on the one hand, asymp-
totic finding of the first adjustment on the other hand),
an antenna pattern is first measured in the horizontal
plane. Assuming random position in space of the rotary
field ellipse, the horizontal pattern means an inclined,
plane, central sectio.. through the pedaloid.

For the mathematical description of this measuring
technology a detailed calculation of receiving charac-
teristics is necessary. In the general case, the basic
element of the curves and surfaces listed in the fol-
lowing is the ellipse.
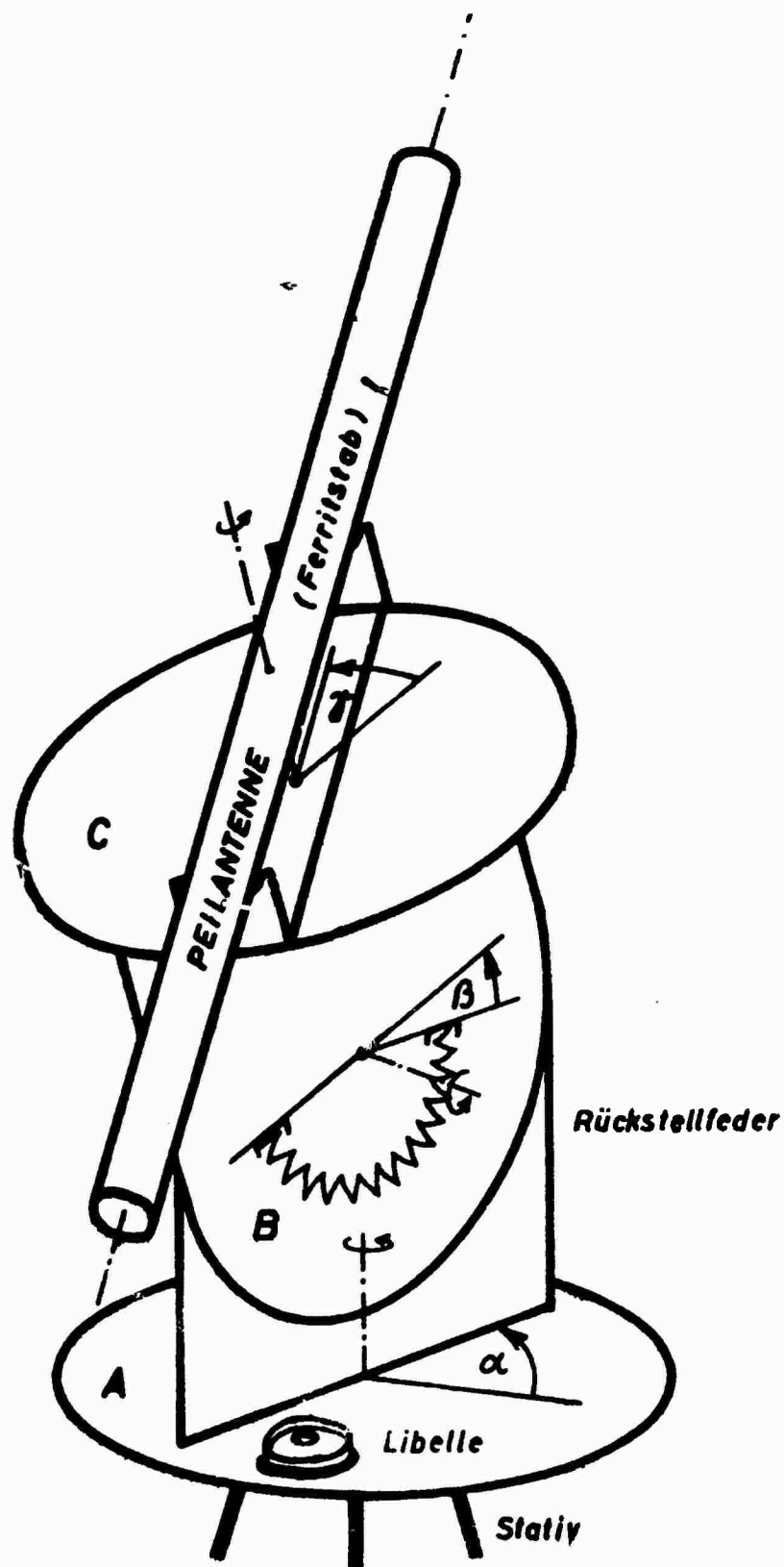
Peilkopf (schematisch)

Empfangsantenne FA6

Fig.: 22

2.4 Pedal locus curve of the ellipse

General definition for a pedal locus curve (cf. /12/):

The pedal locus curve of a given curve related to a pole O is the geometrical locus of the pedal loci F of those perpendicular lines that can be dropped from O on to the tangents of the curve.

Examples:

a) cardioid - pedal locus curve of the circle for one of its points on the periphery as a pole (Fig. 2.3a)

b) lemniscate or figure-of-eight curve - pedal locus curve of an equilateral hyperbola with the center as a pole (Fig. 2.3b).

For the ellipse the pedal locus curve takes the form as is illustrated in Fig. 2.3c with the center as a pole.

Two essential features are
1. that the pedal locus curve differs the less from its ellipse the more circular the latter becomes, and
2. that the pedal locus curve contacts the ellipse in the end points of the major and minor axes.

From the parametric representation in Eq. (2.2) the arbitrary radius r_p of the pedal locus curve can be derived. This calculus was done by /13/ and /14/.

$$r_p = \sqrt{a^2\cos^2\alpha + b^2\sin^2\alpha} = \sqrt{\frac{a^2 + b^2}{2} \quad \frac{a^2 - b^2}{2}\cos 2\alpha}$$

$$(2.3)$$

Therefrom, the parameter-free representation of the pedal locus curve (Fig. 2.3c) in Cartesian coordinates can be derived:

$$a^2x^2 + b^2y^2 = (x^2 + y^2)^2 \qquad (2.4)$$

2.5 The triaxial pedaloid

constitutes the three-dimensional counterpart to the pedal locus curve of the ellipse and can be derived from the ellipsoid on account of the definition of the pedal locus curve.

The derivation of the parameter-free representation of the pedaloid is done in the same way as with the ellipsoid, i.e., in the arbitrary radius of the pedaloid

$$r_{ped} = \sqrt{r_p^2 \cos^2\beta + c^2 \sin^2\beta} \qquad (2.5)$$

r_p is substituted by Eq. (2.3) and the angular functions by the relations mentioned above. The following equation results:

$$a^2x^2 + b^2y^2 + c^2z^2 = (x^2 + y^2 + z^2)^2 \quad (2.6)$$

Special case 1:
revolution pedaloid - it develops by rotating a pedal locus curve of an allipse e.g. on its major axis. Since $b = c$ in this case,

$$a^2x^2 + b^2(y^2 + z^2) = (x^2 + y^2 + z^2)^2 \qquad (2.7)$$

is valid.

Note: Pedaloid and revolution pedaloid occur in optics at the description of the double refraction of the light. The ray surface or wave surface of the extraordinary ray is a (revolution) ellipsoid. To be able to apply SNELLIUS' law of refraction for this extraordinary ray, the term "wavelength standard velocity" is introduced instead of "ray velocity", which is no longer equal to the amount of the radius of the (revolution) ellipsoid but equal to the amount of the radius of the pertinent (revolution) pedaloid.

CARDIOID

LEMNISCATE

a)

b)

PEDAL LOCUS CURVE
OF AN ELLIPSE
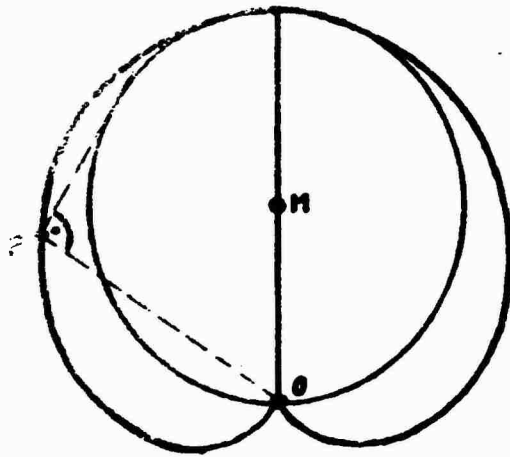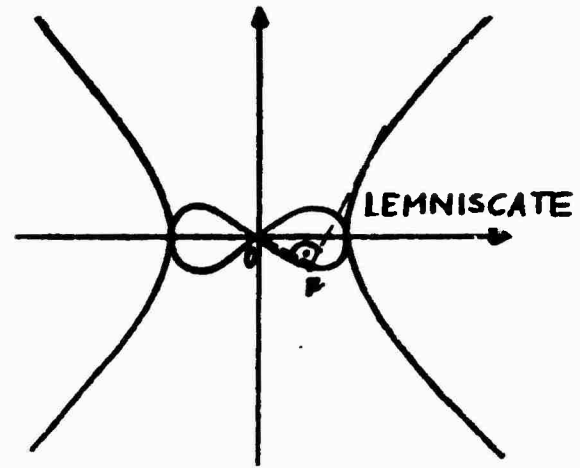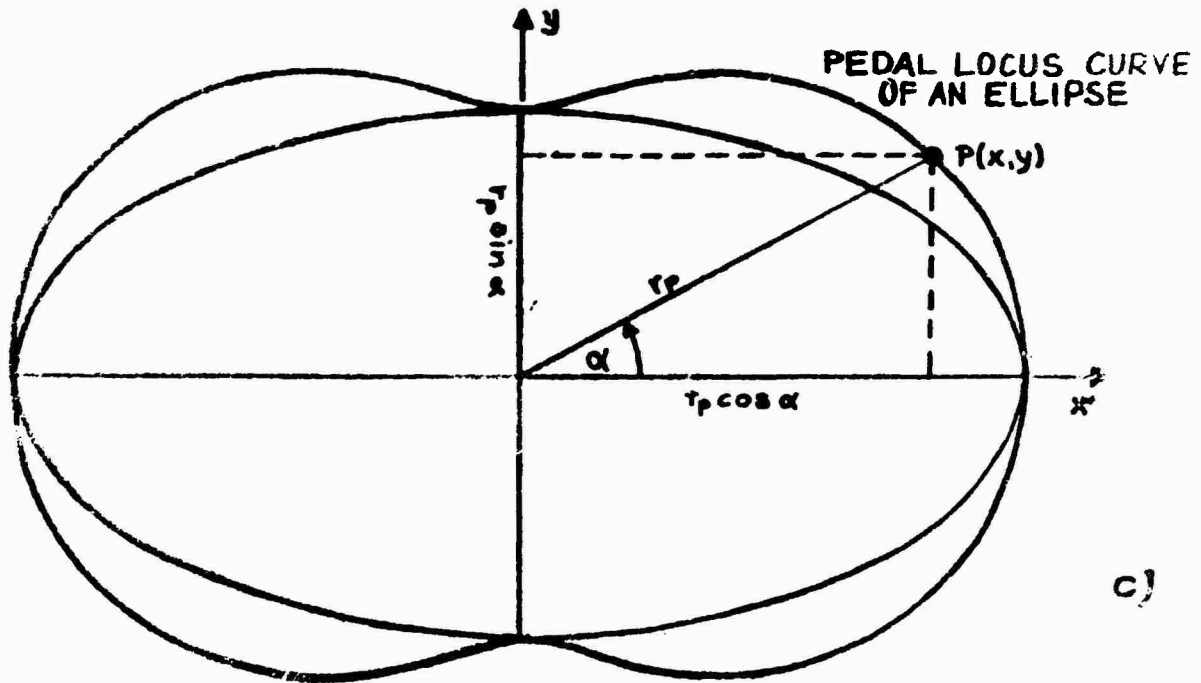
c)

FIG.23

In /15/ formula (2.7) is quoted and the surface is termed "(revolution) ovaloid", the pedal locus curve of the ellipse is termed "oval", since in the above mentioned case of double refraction, the axes of the ellipse etc. differ only slightly. The shape of the pedal locus curve of the ellipse deviates only slightly from that of an ellipse, that is why this term ovaloid is used.

Special case 2:

sphere - if all three axes are equal, i.e., $a = b = c$, both the ellipsoid and the triaxial pedaloid become spheres.

If the passage to the limit $c \rightarrow 0$ is affected, the ellipsoid degenerated to its main sectional ellipse.

2.6 The (true) pedaloid

When keeping to this systematic mathematical classification the receiving characteristic in the elliptically polarized field can be interpreted as being the degenerate case of a triaxial pedaloid by setting the third axis $c = 0$. In contrast to the ellipsoid, the three-dimensional character of the formation thereby developing is preserved in this case.

The parameter-free representation can be obtained quite similarly to that of the ellipsoid. The arbitrary radius r_{pe} results from the radius of the pedal locus curve r_p (cf. Eq. (2.3)) by multiplying by the cosine of the angle of elevation β

$$r_{pe} = r_p \cos\beta = \sqrt{a^2\cos^2\alpha + b^2\sin^2\alpha} \cdot \cos\beta \qquad (2.8)$$

By substituting the angular functions as mentioned before the equation of the (true) pedaloid

$$a^2x^2 + b^2y^2 = (x^2 + y^2 + z^2)^2 \qquad (2.9)$$

is obtained which is most important for measurements in the elliptically polarized field. The families of pedaloids are listed in Fig. 2.4.

Special case:

Circular ring (torus) with the inner radius being zero; occurs with circular polarization of the field (a = b). Eq. (2.9) then reads

$$a^2(x^2 + y^2) = (x^2 + y^2 + z^2)^2 \qquad (2.10)$$

The arbitrary radius r_{tor}

$$r_{tor} = a \cdot \cos \beta \qquad (2.11)$$

Degenerate case:

Double sphere - representing the three-dimensional receiving characteristic in the linearly polarized field. On account of b = 0, its equation reads

$$ax = x^2 + y^2 + z^2 \qquad (2.12)$$

The arbitrary radius

$$r_{ds} = a \cos \alpha \cdot \cos \beta \qquad (2.13)$$

2.7 Intersection of the pedaloid with a plane

Owing to the measuring technique it is important to know the sections of the pedaloid involved. To find them, a new coordinate system x', y', z' is introduced resulting

THE FAMILIES OF ELLIPSOIDS
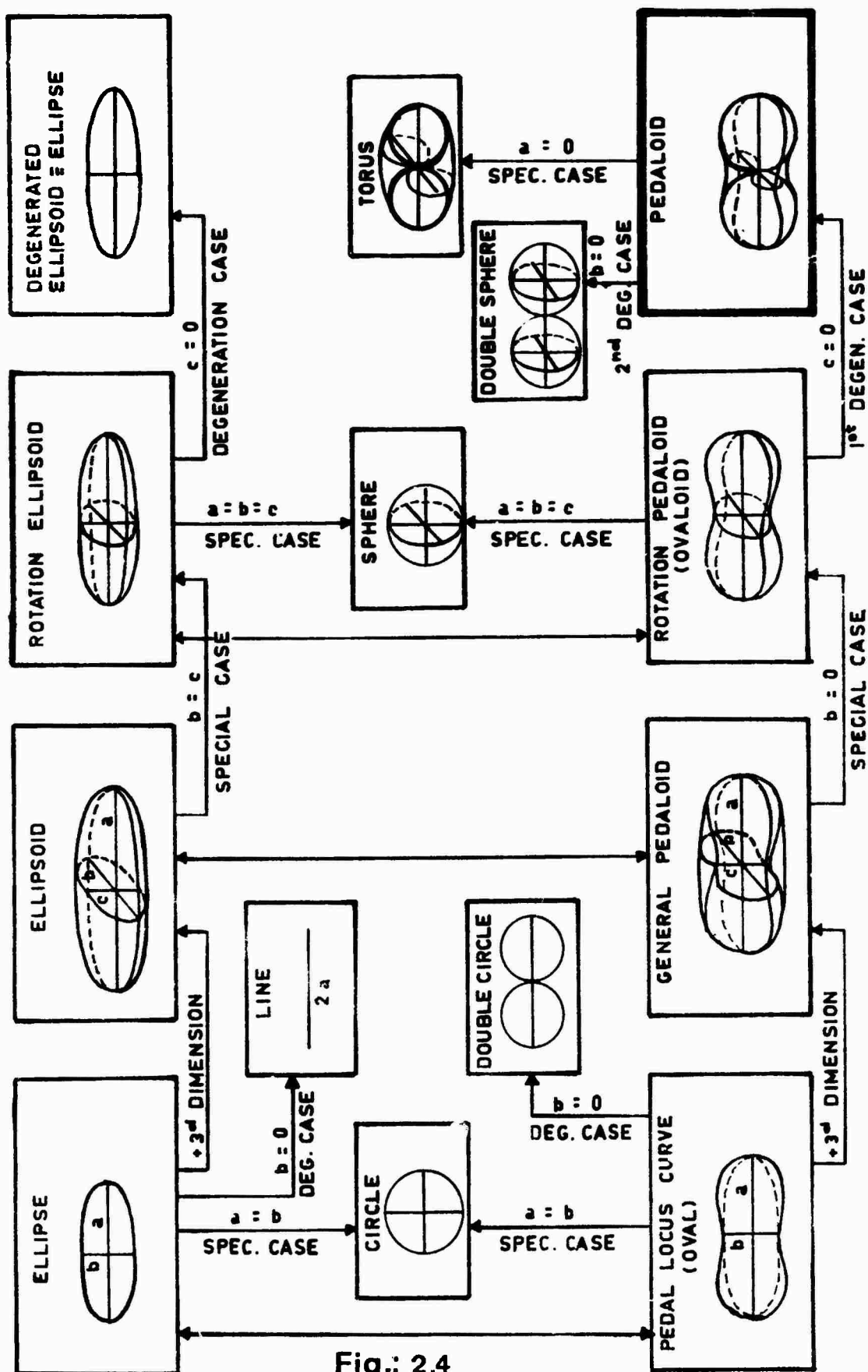
Fig.: 2.4

from the original one by successive rotation by the angles u, v, w (Eulerian angles). The origin remains constant. Setting z' = 0, we obtain the cross-sectional area lying in the plane (x', y').

The following equation describes this rotation

$$\vec{r} = a_{ik}\vec{r}' \qquad \begin{aligned} \vec{r} &= (x, y, z) \\ \vec{r}' &= (x',y',z') \end{aligned} \qquad (2.14)$$

$\vec{r}$ and $\vec{r}'$ are position vectors. The elements of the matrix a_{ik} are the direction cosines and read

$$a_{11} = \cos v \cdot \cos w$$

$$a_{12} = -\cos u \cdot \sin w$$

$$a_{13} = \sin v$$

$$a_{21} = \cos u \cdot \sin w + \sin u \cdot \sin v \cdot \sin w$$

$$a_{22} = \cos u \cdot \cos w - \sin u \cdot \sin v \cdot \sin w \qquad (2.15)$$

$$a_{23} = -\sin u \cdot \cos v$$

$$a_{31} = \sin u \cdot \sin w - \cos u \cdot \sin v \cdot \cos w$$

$$a_{32} = \sin u \cdot \cos w + \cos u \cdot \sin v \cdot \sin w$$

$$a_{33} = \cos u \cdot \cos v$$

In Eq. (2.9) x, y, z are substituted by x', y', z'. On account of the above relation the pedaloid in the dashed coordinates is obtained:

$$a^2(a_{11}x' + a_{12}y' + a_{13}z')^2 + b^2(a_{21}x' + a_{22}y' + a_{23}z')^2 =$$

$$= \left[(a_{11}x' + a_{12}y' + a_{13}z')^2 + (a_{21}x' + a_{22}y' + a_{23}z')^2 + \right.$$

$$\left. + (a_{31}x' + a_{32}y' + a_{33}z')^2 \right]^2 \qquad (2.16)$$

Since only the intersection is of interest here, $z' = 0$.
By squaring the brackets in Eq. (2.16) we obtain

$$a^2(a_{11}^2 x'^2 + 2a_{11}a_{12}x'y + a_{12}^2 y'^2) + b^2(a_{21}^2 x'^2 +$$

$$+ 2a_{21}a_{22}x'y' + a_{22}^2 y'^2) = |(a_{11}^2 + a_{21}^2 + a_{31}^2)x'^2 +$$

$$+ (a_{12}^2 + a_{22}^2 + a_{32}^2)y'^2 + 2(a_{11}a_{12} + a_{21}a_{22} + a_{31}a_{32})x'y'|^2$$

$$(2.17)$$

If the left side is rearranged and if we further consider
on the right side that the sum of the squares of the
direction cosines is equal to 1 and the sum of the com-
posite products is equal to zero, we obtain

$$(a^2 a_{11}^2 + b^2 a_{21}^2)x'^2 + (a^2 a_{12}^2 + b^2 a_{22}^2)y'^2 +$$

$$+ 2(a^2 a_{11}a_{12} + b^2 a_{21}a_{22})x'y' = (x'^2 + y'^2)^2 \quad (2.18)$$

This equation again represents a pedal locus curve of an
ellipse in relation to the coordinate system x', y'. On
account of the term with the composite elements, major
and minor axes of the pedal locus curve are not lying in
the direction of the coordinate axes. The sections on
the x' and y' axes are

$$A' = \sqrt{a^2 a_{11}^2 + b^2 a_{21}^2} \quad \text{and} \quad B' = \sqrt{a^2 a_{12}^2 + b^2 a_{22}^2} \quad (2.19)$$

Proceeding from the general equation of sections (2.18)
the various special cases can be derived.

Special case 1: (plane vertical to main pedal locus curve)

a) plane vertical to the original pedal locus plane
through the major axis a, $u = 90^\circ$, $v = 0^\circ$

Note: Rotation by the two angles u and v is sufficient
to reach any desired direction in space. The matrix
of rotation is simplified to a 2 x 2 matrix: the
angular functions for w = 0 must be equal to 1 or 0.

The matrix of rotation therefore reads

$$a_{ik} = \begin{Vmatrix} 1 & 0 \\ 0 & 0 \end{Vmatrix} \qquad (2.20)$$

Eq. (2.18) is reduced to

$$ax' = x'^2 + y'^2 \qquad \text{or} \qquad y'^2 = ax' - x'^2 \qquad (2.21)$$

which is well known to be the vertex equation of the
circle with the radius a/2, where x' is pointing into
the direction of x and y' into that of z.

b) plane vertical through minor axis b, $u = 0^0$, $v = 90^0$

$$\text{matrix} \qquad a_{ik} = \begin{Vmatrix} 0 & 0 \\ 0 & 1 \end{Vmatrix} \qquad (2.22)$$

In this case,

$$by' = x'^2 + y'^2 \qquad \text{or} \qquad x'^2 = by' - y'^2 \qquad (2.23)$$

is the vertex equation of the circle with the radius b/2,
where x' is pointing into the direction of z and y'
into that of y.

c) arbitrary plane vertical to main pedal locus curve,
$u = 90^0$, $0 < v < 90^0$

$$\text{matrix} \qquad a_{ik} = \begin{Vmatrix} \cos v & 0 \\ \sin v & 0 \end{Vmatrix} \qquad (2.24)$$

yields

$$y'^2 = x' \sqrt{a^2\cos^2 v + b^2\sin^2 v} - x'^2 \qquad (2.25)$$

The radical represents the radius of the intersected pedal locus curve and is equal to the diameter of the vertex circle represented by Eq. (2.25).

Result from 1 a) - c): All surfaces of intersection vertical to the main pedal locus curve of the pedaloid are vertex circles in relation to the center of the pedaloid.

Special case 2:

Intersections through the minor axis b, $u = 0^O$, $0 < v < 90^\circ$

$$\text{matrix} \qquad a_{ik} = \begin{Vmatrix} \cos v & 0 \\ 0 & 1 \end{Vmatrix} \qquad (2.26)$$

We obtain the pedal locus equations

$$a^2 a_{11}^2 x'^2 + b^2 y'^2 = (x'^2 + y'^2)^2 \qquad (2.27)$$

The condition $a_{11} = \cos v = b/a$ yields a circle with the radius b as surface of intersection.

Proof:

$$a^2 \frac{b^2}{a^2} x'^2 + b^2 y'^2 = (x'^2 + y'^2)^2$$

$$b^2(x'^2 + y'^2) = (x'^2 + y'^2)^2$$

$$x'^2 + y'^2 = b$$

If $\cos v = \frac{b}{a}$, $b > a^2 a_{11}^2$ and forms the major axis of the curve of intersection which is again a pedal locus curve.

Special case 3:

Intersections through the major axis a, $0 < u < 90^\circ$, $v = 0^\circ$

matrix $\qquad a_{ik} = \begin{Vmatrix} 1 & 0 \\ 0 & \cos u \end{Vmatrix}$ $\qquad$ (2.28)

We obtain the pedal locus equation

$$a^2 x'^2 + b^2 a_{22}^2 y'^2 = (x'^2 + y'^2)^2 \qquad (2.29)$$

Summarizing the following characteristic properties of the pedaloid can be given:

1. The main intersection (containing the axes a and b of the ellipse) is the pedal locus curve with the largest area.

2. The radius vector vertical through the center O of the main intersection is equal to zero.

3. All intersections vertical to the main pedal locus surface have the shape of a figure eight. The largest area of this kind occurs at the intersection containing the major axis $\underline{a}$, the smallest area arises at the intersection containing the minor axis $\underline{b}$.

4. That intersection area that contains the minor axis and is inclined to the main pedal locus curve by the angle v, so that
$$\cos v = a/b$$
is valid, is a circle with the radius $r_{pe} = b$.

2.8 Calculation of the squint at polarization ellipses lying arbitrarily in space

If the polarization ellipse is not lying in the horizontal plane of measurement and if the direction finder for the

detection of the maximum and minimum of field strength
is rotated only in this plane, a specific error of
measurement arises which can be determined by the fol-
lowing extreme value problem.

If the coordinate system in which the major axis of the
pedaloid is pointing in the direction of the x-axis and
the minor axis in y-axis direction, is revolved on the
x-axis by the angle u and consequently on the new
y_1-axis by the angle v, any arbitrary intersection area
can be obtained as x'y'-plane. Let this intersection area
of the pedaloid be the pedal locus curve measured hori-
zontally; the question arises, what size the angle w must
assume to make the newly developed axes x' and y' point
in the directions of a' and b', respectively; a' and b'
are the major and minor axes of the pedal locus curve in
the intersection. This angle is at the same time that
squint that is made with the above described direction
finding.

Proceeding from the equation of the pedaloid in the dash
system, the coefficient of x' giving the length of the
section A' on the x'-axis reads as follows:

$$A' \quad (a^2 a_{11}^2 + b' a_{..}) \quad$$

$$= a' \cos^2 v \cdot \cos w + b^2 (\cos^2 u \cdot \sin^2 w +$$

$$+ \sin^2 u \cdot \sin^2 v \cdot \cos^2 w + \sin u \cdot \cos u \cdot \sin v \cdot \sin 2$$

$$(2.30)$$

The derivation with respect to w is formed and set zero
resulting

$$\frac{\sin 2w}{\cos 2w} = \tan 2 = \frac{\sin 2u \cdot \sin v}{\frac{a^2}{b^2} \cos^2 v + \sin^2 u \cdot \sin^2 v - \cos^2 u} \quad (2. \quad)$$
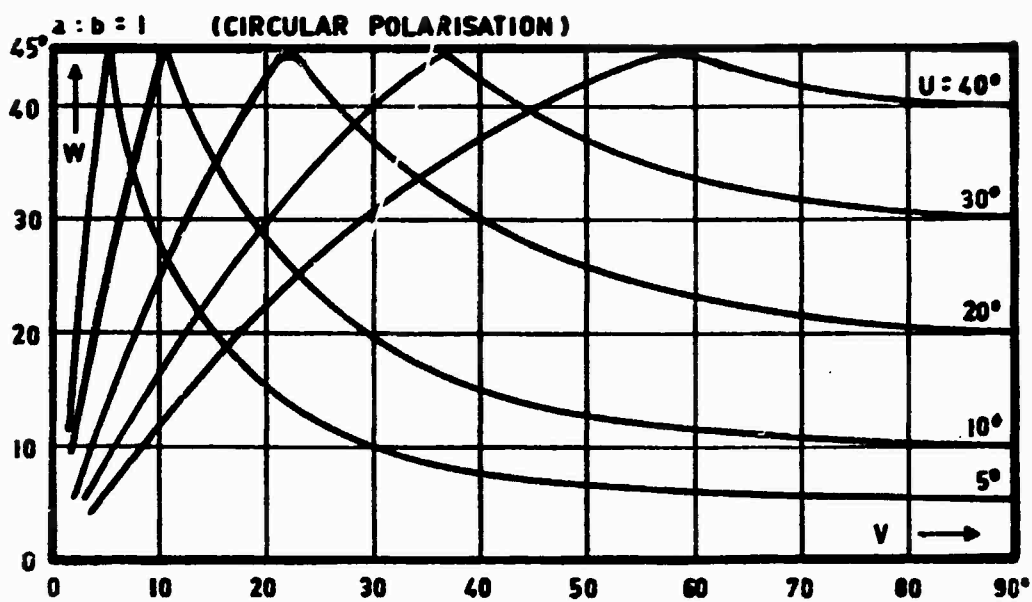
BEARING ERROR W

FIG. 2.5
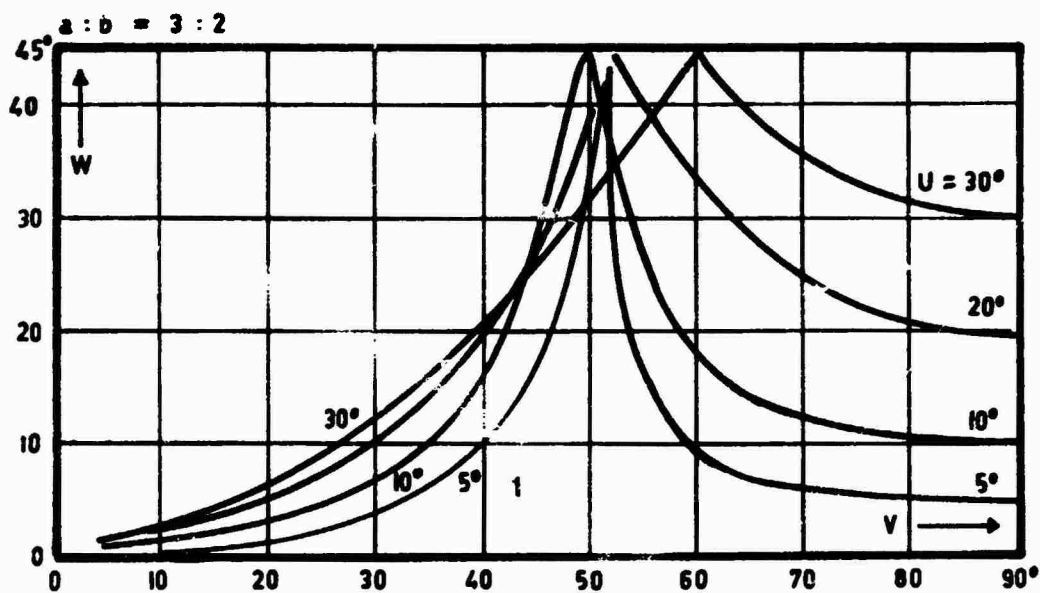
FIG. 2.6

BEARING ERROR W
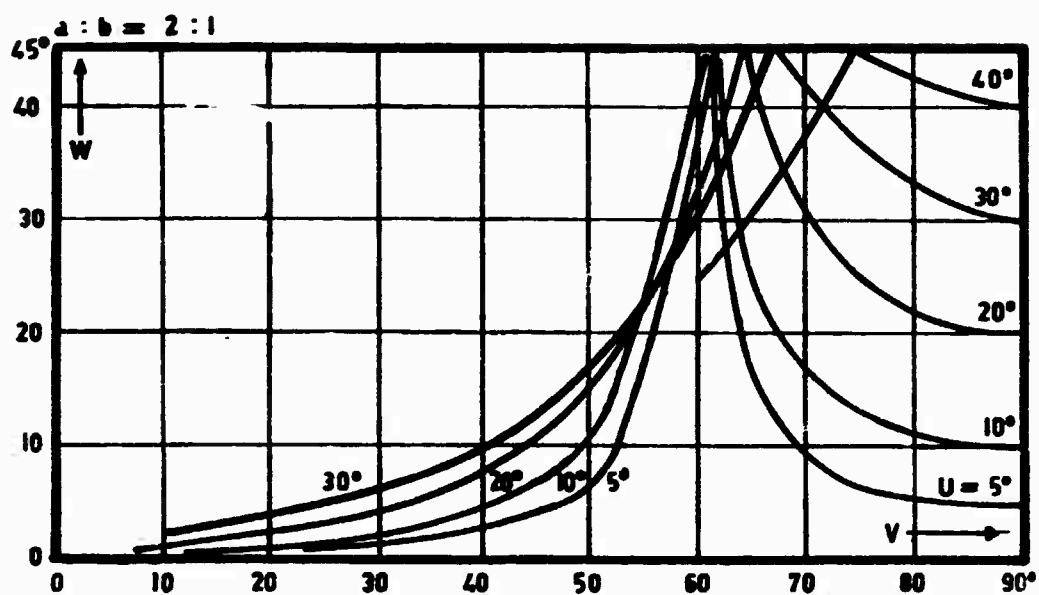
FIG. 2.7
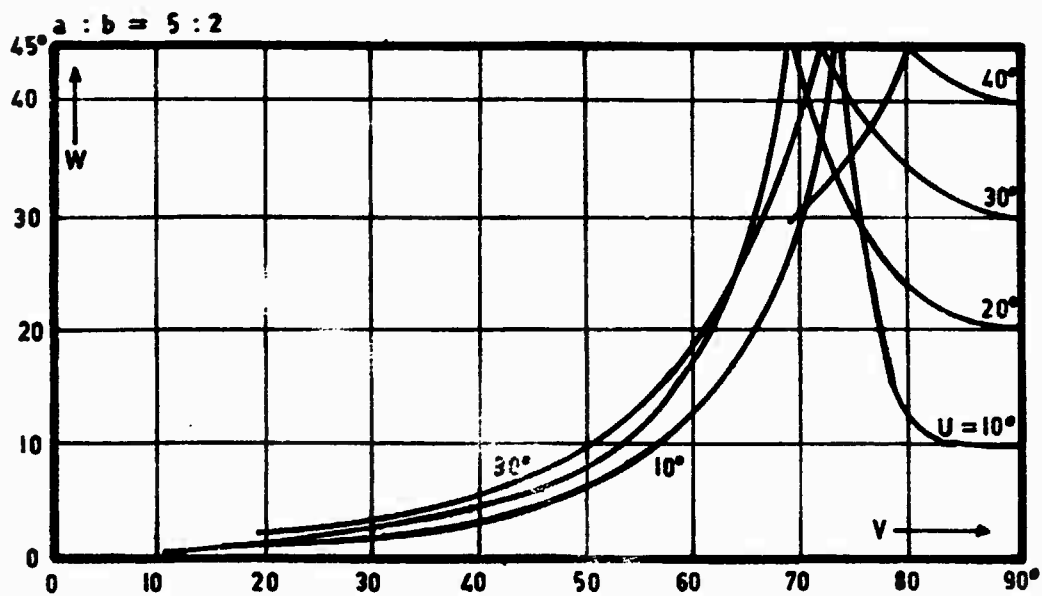
FIG. 2.8

For a check the angle obtained from the above equation can be inserted into the coefficient of the "term of rotation" of Eq. (2.18) which then has to vanish. The easier way is to set the coefficient C' of the term of rotation equal to zero and calculate w therefrom and compare it with the above result proving it.

The angle w was consequently computed for the following parameters:

Q (= a : b) = 1; 1.5; 2; 2.5; 3; 3.5; 4; 4.5; 5

$$\left.\begin{array}{l} u \\ v \end{array}\right\} = 1, 2, 3, 4, 5, 6, 7, 8, 9, 10, 20, 30, \ldots, 80^{\circ}$$

The results are represented graphically in Figs. 2.5 - 2.8 for different ratios of axis a : b of the polarization ellipse. Fig. 2.5 is valid for a circularly polarized field (a = b). From the other diagrams it is to be seen that only for great angles u and v the squint is essential, e.g. for u = v = 30°, w = 12° (a : b = 3 : 2), cf. Fig. 2.6. For ellipses with a smaller ratio of axes this squint becomes less important. Fig. 2.8 shows that a distortion of the ellipse u = v = 30° yields the negligible angle w = 4°.

2.9 Conclusions

With the mathematical representation of the receiving characteristic in an elliptically polarized electromagnetic field (= pedaloid) it is possible to calculate every arbitrary section plane of this pedaloid. This fact involved many advantages for field strength measurements. One of the most important things is that we are able to calculate the squint that arises when the direction finder is rotated only in the horizontal plane when measuring the maximum, the polarization ellipse, however, lies arbitrarily in space.

CHAPTER 3

A NEW METHOD TO DETERMINE THE SPATIAL POSITION
OF THE MAGNETIC ROTARY FIELD ELLIPSE

3.1 Introduction

For many experiments concerning VLF-reception it is
necessary to know the exact position of the rotary field
ellipse. N. NESSLER described a method to determine the
pedaloid in his thesis /10/. This method, however, showed
to be time-wasting and in some cases unexact; the error
made by this method is calculated by R. Klein /16, 17/.
The problem was to find a new method using all charac-
teristics of the pedaloid for a better and non-subjective
calculation. All the quantities of the rotary field
ellipse had to be measured by means of an antenna system
constant in space instead of using the direction finding
antenna of former experiments.

3.2 The pedaloid

The measurement of a rotary field ellipse always leads
to "pedal locus curves" when using ferrite-rod direction
finding antennas.

Let us now briefly consider this effect mathematically:

> a ... maximum voltage - major axis
>
> b ... minimum voltage - minor axis
>
> ω ... angular frequency
>
> ϕ ... angle of inclination between major axis
>   and antenna
>
> θ ... angle between the normal of the ellipse
>   plane and the antenna
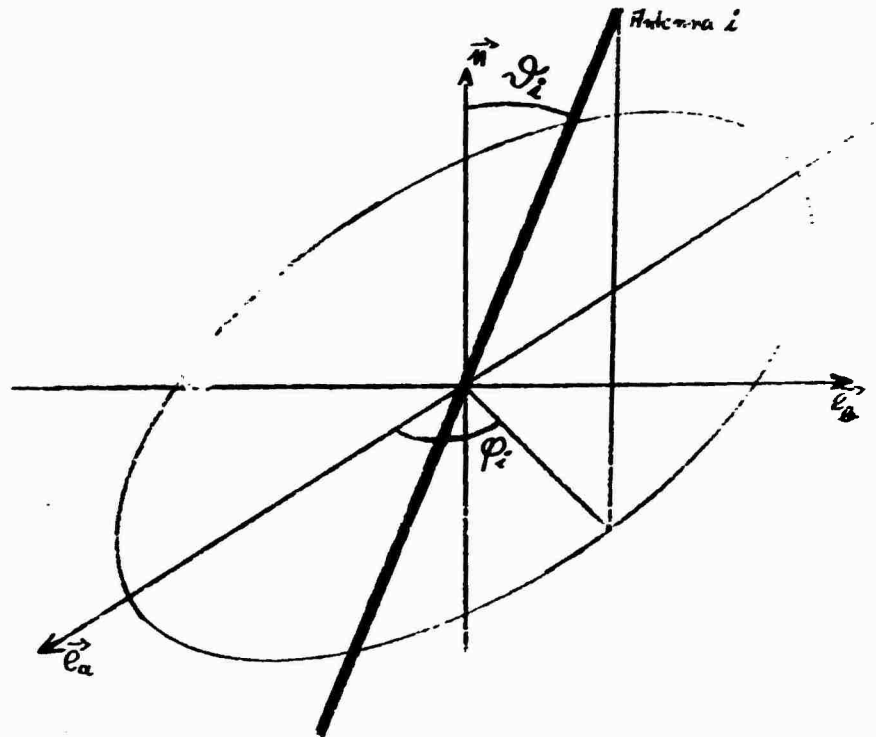
Fig. 3.1

The voltage induced into an antenna in dependence on ω, ϕ, and θ is given by

$$U = (a \cdot \cos\phi \cdot \cos\omega t + b \cdot \sin\phi \cdot \sin\omega t)\sin\theta \qquad (3.1)$$

with a and b containing all conversion factors between magnetic field strength and voltage.

The temporal maximum (minimum) of the voltage is reached when

$$\left.\frac{dU}{dt}\right|_{t=t_0} = 0 = \omega(-a \cdot \cos\phi \cdot \sin\omega t_0 + b \cdot \sin\phi \cdot \cos\omega t_0)\sin\theta \qquad (3.2)$$

resulting

$$\frac{b}{a} \cdot \tan\phi = \tan\omega t_0 \qquad (3.3)$$

Which further on will be referred to as "pedaloid-condition".

It can be seen that the phase angle relative to the
major axis is not identical with the spatial angle,
except for the case a = b. And the antenna does not
reproduce the ellipse, but a pedal locus curve or a
pedaloid.

3.3 Theory of the new method

The antenna combination consists of three electrically
identical ferrite-rod antennas perpendicular to one
another thereby forming an orthogonal trihedral. The
three axes of the pedaloid are represented by the vectors
$\vec{e_a}$, $\vec{e_b}$, and $\vec{n}$, with the subscripts a and b standing for
the major and minor axes of the ellipse, respectively,
and n being the normal vector of the rotary field ellipse.
The arbitrary position of the rotary field ellipse in
respect to an other Cartesian system is given by the
three Eulerian angles ϕ, ψ, θ. Besides, two more unknown
quantities are requested for a complete description of
the ellipse in space, namely the two main voltages of
the ellipse. If we succeed in measuring these five
quantities position and size of the ellipse arbitrary
in space are definitely determined.

3.4 Calculation

Fig. 2 shows the normal of the ellipse in reference to
the antenna system.

Let the directions of the antennas be $\vec{i}$, $\vec{j}$, and $\vec{k}$,
the following conditions can be calculated (antenna
directions expressed by direction cosines in respect
to $\vec{e_a}$, $\vec{e_b}$, and $\vec{n}$):
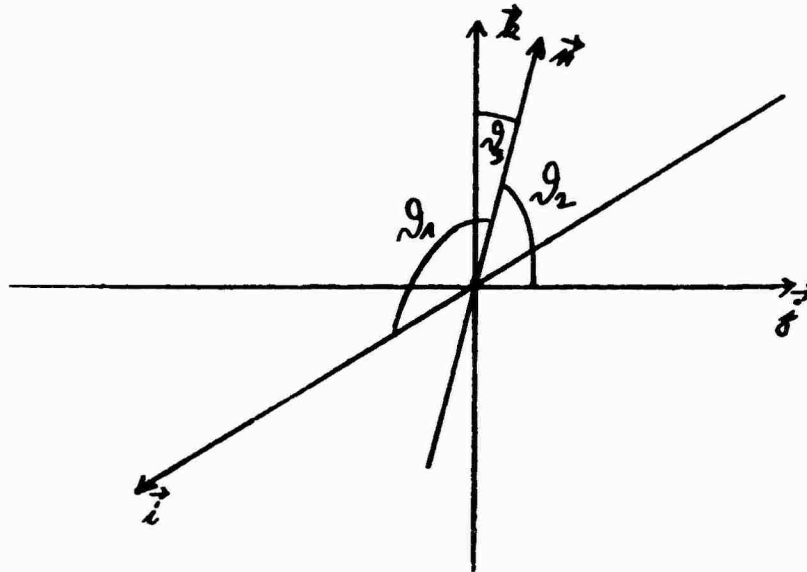
Fig. 3.2

$$\vec{i} = \begin{pmatrix} \cos\phi_1 \cdot \sin\theta_1 \\ \sin\phi_1 \cdot \sin\theta_1 \\ \cos\theta_1 \end{pmatrix} ; \quad \vec{j} = \begin{pmatrix} \cos\phi_2 \cdot \sin\theta_2 \\ \sin\phi_2 \cdot \sin\theta_2 \\ \cos\theta_2 \end{pmatrix} ; \quad \vec{k} = \begin{pmatrix} \cos\phi_3 \cdot \sin\theta_3 \\ \sin\phi_3 \cdot \sin\theta_3 \\ \cos\theta_3 \end{pmatrix}$$

$$(3.4)$$

As $\vec{i}$, $\vec{j}$, and $\vec{k}$ form an orthogonal trihedral the following conditions are valid, too.

$$
\begin{aligned}
\vec{i} \times \vec{j} &= \vec{k} \\
\vec{j} \times \vec{k} &= \vec{i} \\
\vec{k} \times \vec{i} &= \vec{j}
\end{aligned}
\qquad (3.5)
$$

Together with the pedaloid condition (3.3) we get from (3.1) the voltages in terms of ϕ_i and θ_i:

$$U_i = (a^2 \cdot \cos^2\phi_i + b^2 \cdot \sin^2\phi_i)^{1/2} \cdot \sin\theta_i \qquad (3.6)$$

and with the abbreviation $\omega t_o = \Omega$ we obtain

$$U_i = a \cdot b \cdot (a^2 \cdot \sin^2\Omega_i + b^2 \cdot \cos^2\Omega_i)^{-1/2} \cdot \sin\theta_i \quad (3.7)$$

and thereby the voltages expressed by the phase angles Ω_i. These three voltages form a vector with a constant amount, e.g.

$$\sum_{i=1}^{3} U_i^2 = a^2 (\cos^2\phi_1 \cdot \sin^2\theta_1 + \cos^2\phi_2 \cdot \sin^2\theta_2 + \cos^2\phi_3 \cdot \sin\theta_3) +$$
$$b^2 (\sin^2\phi_1 \cdot \sin^2\theta_1 + \sin^2\phi_2 \cdot \sin^2\theta_2 + \sin^2\phi_3 \cdot \sin\theta_3)$$
$$(3.8)$$

From Eq. (3.4) we know that $\cos\phi_i \cdot \sin\theta_i$ and $\sin\phi_i \cdot \sin\theta_i$ are the direction cosines of the pedaloid axes $\vec{e_a}$ and $\vec{e_b}$ in reference to the antenna system. As the sum of the squares of direction cosines always equals 1 we may write formula (3.8) shortly as

$$\sum_{i=1}^{3} U_i^2 = a^2 + b^2 \quad (3.9)$$

On the other hand, the condition of orthogonality delivers the following formula:

$$\vec{k} = \vec{i} \times \vec{j} =$$

$$\begin{pmatrix} k_1 \\ k_2 \\ \cos\theta_3 \end{pmatrix} = \begin{pmatrix} i_2 j_3 - i_3 j_2 \\ i_3 j_1 - i_1 j_3 \\ (\cos\phi_1 \cdot \sin\phi_2 - \cos\phi_2 \cdot \sin\phi_1)\sin\theta_1 \cdot \sin\theta_2 \end{pmatrix}$$
$$(3.10)$$

The main result of this formula is:

$$\cos\theta_3 = -\sin(\phi_1 - \phi_2)\sin\theta_1 \cdot \sin\theta_2$$
$$\cos\theta_2 = -\sin(\phi_2 - \phi_1)\sin\theta_1 \cdot \sin\theta_3 \quad (3.11)$$
$$\cos\theta_1 = -\sin(\phi_3 - \phi_3)\sin\theta_2 \cdot \sin\theta_3$$

With the pedaloid condition (3.3) we derive

$$\sin(\phi_1 - \phi_2) = \sin\phi_1 \cdot \cos\phi_2 - \sin\phi_2 \cdot \cos\phi_1 =$$

$$= \frac{\frac{a}{b} \tan\Omega_1}{\sqrt{1 + \frac{a^2}{b^2} \tan^2\Omega_1}} \cdot \frac{1}{\sqrt{1 + \frac{a^2}{b^2} \tan^2\Omega_2}} -$$

$$- \frac{\frac{a}{b} \tan\Omega_2}{\sqrt{1 + \frac{a^2}{b^2} \tan^2\Omega_2}} \cdot \frac{1}{\sqrt{1 + \frac{a^2}{b^2} \tan^2\Omega_1}} \qquad (3.12)$$

We then obtain with Eq. (3.7)

$$\sin(\phi_1 - \phi_2) = \frac{\sin(\Omega_1 - \Omega_2)}{ab \cdot \sin\theta_1 \cdot \sin\theta_2} U_1 U_2 \qquad (3.13)$$

Consequently, Eq. (3.11) with the abbreviations $\Omega_1 - \Omega_2 = X_1$, $\Omega_2 - \Omega_3 = X_2$, $\Omega_3 - \Omega_1 = X_3$ (phase differences between two antennas) reads as follows:

$$\cos\theta_1 = - \frac{\sin X_2}{ab} U_2 U_3$$

$$\cos\theta_2 = - \frac{\sin X_3}{ab} U_3 U_1 \qquad (3.14)$$

$$\cos\theta_3 = - \frac{\sin X_1}{ab} U_1 U_2$$

Since these cosines $\cos\theta_i$ are the direction cosines of the normal of the ellipse in reference to the antenna system

$$\sum_{i=1}^{3} \cos^2\theta_i = 1 \qquad (3.15)$$

is valid, or, for further calculations

$$a^2 b^2 = \sin^2 X_1 U_1^2 U_2^2 + \sin^2 X_2 U_2^2 U_3^2 + \sin^2 X_3 U_3^2 U_1^2 \qquad (3.16)$$

Formulas (3.9) and (3.16) together allow the evaluation of a and b.

$$P^2 = a^2 + b^2 = \sum_{i=1}^{3} U_i^2 \tag{3.17}$$

$$Q^2 = a^2 \cdot b^2 = \sum_{i=1}^{3} \sin^2 X_i U_i^2 \cdot U_{i+1}^2 \tag{3.18}$$

and therefrom

$$a^2 = \frac{P^2}{2} + \sqrt{\frac{P^4}{4} - Q^2} \tag{3.19}$$

and

$$b^2 = \frac{P^2}{2} - \sqrt{\frac{P^4}{4} - Q^2} \tag{3.20}$$

So the two main voltages are known in terms of the measured quantities!

3.5 Calculation of the Eulerian angles

The three Eulerian angles are θ, ψ, and ϕ.

θ ... angle of nutation (between ellipse normal $\vec{n}$ and the direction $\vec{k}$)

ψ ... angle of precession (between axis i and intersection line $\vec{x}$ of the $\vec{e}_a$-$\vec{e}_b$-plane and the i-j-plane)

ϕ ... angle of torsion (between the intersection line $\vec{x}$ and the axis $\vec{e}_a$)

<u>θ:</u> It is evident (Fig. 3.2) that

$$\theta \equiv \theta_3 \tag{3.21}$$

<u>ψ:</u> First we have to determine the intersection line $\vec{x}$.
So we form the cross product of the vectors $\vec{k}$ and $\vec{n}$.

$$\vec{k} \times \vec{u} = \begin{pmatrix} \sin\phi_3 \\ -\cos\phi_3 \\ 0 \end{pmatrix} = \vec{x} \tag{3.22}$$

Now the requested angles are easily to be calculated:

$$(\vec{X} \cdot \vec{i}) = \cos\psi = \cos\phi_1 \cdot \sin\theta_1 \cdot \sin\phi_3 - \sin\phi_1 \cdot \sin\theta_1 \cdot \cos\phi_3 \tag{3.23}$$

As there are certain conditions valid between the direction cosines in the matrix of torsion we can write Eq. (3.23) as follows:

$$(\vec{X} \cdot \vec{i}) = \cos\psi = -\frac{\cos\theta_2}{\sin\theta_3} \tag{3.24}$$

Together with (3.15)

$$\sin\psi = \frac{\cos\theta_1}{\sin\theta_3} \tag{3.25}$$

follows.

$\underline{\phi:}$ The angle ϕ follows from the scalar product of the vectors $\vec{x}$ and $\vec{e_a}$.

$$\vec{x} \cdot \vec{e_a} = \cos\phi = \sin\phi_3 \tag{3.26}$$

$\sin\phi$ follows from the cross product of these two vectors:

$$\left| \left| \vec{x} \times e_a \right| \right| = \sin\phi = \cos\phi_3 \tag{3.27}$$

We now have to write the Eulerian angles in terms of the voltages U_1, U_2, U_3 and the phase angles X_1, X_2, X_3.

$\underline{\theta:}$
$$\cos\theta \equiv \cos\theta_3 = -\frac{\sin X_1}{ab} \cdot U_1 U_2 \tag{3.28}$$

As ab is evaluated in Eq. (3.16), $\cos\theta$ is known.

$\underline{\psi:}$

$$\cos\psi = -\frac{\cos\theta_2}{\sin\theta_3} \tag{3.29}$$

$$\cos\theta_2 = - \frac{\sin_3}{ab} U_3 U_1 \tag{3.30}$$

$$\sin\theta_3 = \sqrt{1 - \cos^2\theta_3} = \frac{1}{ab} \cdot \sqrt{\sin^2 X_2 U_2^2 U_3^2 + \sin^2 X_3 U_3^2 U_1^2} \tag{3.31}$$

$$\cos\psi = \frac{1}{\sqrt{\frac{\sin^2 X_2 U_2^2}{\sin^2 X_3 U_1^2} + 1}} \tag{3.32}$$

$$\sin\psi = \frac{\cos\theta_1}{\sin\theta_3} \tag{3.33}$$

$$\cos\theta_1 = - \frac{\sin X_1 U_1 U_2}{ab} \tag{3.34}$$

$$\sin\psi = \frac{-1}{\sqrt{1 + \frac{\sin^2 X_3 U_1^2}{\sin^2 X_2 U_2^2}}} \tag{3.35}$$

So the angle ψ is known, too.

ϕ: From Eq. (3.6) we get:

$$\cos\phi = \sin\phi_3 \tag{3.36}$$

$$U_3^2 = (a^2\cos^2\phi_3 + b^2\sin^2\phi_3)\sin^2\theta_3 \tag{3.37}$$

$$\sin^2\phi_3 = \frac{\frac{U_3^2}{\sin^2\theta_3} - a^2}{b^2 - a^2} \tag{3.38}$$

$$\sin\phi = \cos\phi_3 \tag{3.39}$$

$$\cos\phi_3 = \frac{\frac{U_3^2}{\sin^2\theta_3} - b^2}{a^2 - b^2} \tag{3.40}$$

As a, b, and $\sin\theta_s$ are known from Eqs. (3.19), (3.20),
(3.14), all Eulerian angles are known in terms of the
measured quantities.

3.6 Conclusion

It is possible to determine the exact spatial position
of the rotary field ellipse by measuring three voltages
and three phase angles. The results can be computed.
This new method has the advantage of being quick and free
of errors of adjustment (measurement possible at any
trihedral position!) and can be done automatically with-
out any further adjustment of the antenna position.

CHAPTER 4

EXTERNALLY KEYED PHASE-LOCK DEVICE

4.1 Equipment

The externally keyed (by VLF-wave propagation) phase-lock device described in /11/ measures the phase difference between a VLF wave with the frequency of 2.667 kHz in the near field and the GBR signal (16.0 kHz) in the far field. The measuring principle shall be briefly repeated (cf. Fig. 4.1, 4.2, 4.3).

The GBR signal (A2 or F2 keyed) is received by ferrite rod antennas and used for phase-stable triggering of an extremely stable balance oscillator. The lock-in range is only 20 Hz so that only the 16,000 Hz-signal is used for phase triggering during the FM-keyed time (16,000 and 15,950 Hz), thus avoiding influences of keying effects and giving a stable, extremely exact time normal at any arbitrary point of reception.

This type of time normal is used to trigger both the transmitter and the receiver of a VLF-signal transmission chain. Before triggering the frequency must be changed in order not to affect the original "clock-triggering" signal. To get the required high accuracy only a digital frequency change is allowed. In the described equipment a divide-by-6-mode is used so that the frequency of 2.667 Hz results.

In the transmitting equipment this signal is amplified and sent by a frame antenna.

The receiving equipment uses two ferrite rod antennas for the reception of the VLF signal and of the GBR synchronous signal, respectively. The two signals (VLF signal and the divided 16 kHz signal) are compared in the phase detector. The result is a DC-signal changing with phase difference which may act as phase proportional voltage on the one hand or as rectified signal of a receiver with extremely small bandwidth (depending on integration time constant; here 0.2 Hz!) on the other hand.

The measuring practice showed the necessity of some changes and supplements in circuit design, e.g.:
1) a special Schmitt-trigger to make the triggering correspond with the zero-axis crossing of the GBR signal, thus ensuring that the phase relation is independent on the amplitude (further details see Fig. 4.1 or /11/);
2) a measuring amplifier for measuring the incoming VLF signal combined with an attenuator providing a unique signal amplitude at the phase detector independent on the input voltage (cf. Fig. 4.2 and 4.3);
3) a main operation mode switch with the positions "off / battery control / GBR amplitude / VLF amplitude / phase".
A number of test jacks were added at the front panels of both the transmitting and receiving parts for operation control and the possibility of connecting external devices (e.g. line recorder).

The complete electrical and mechanical design is shown in Figs. C, D, E, F.

4.2 Measurements

The measurements were scheduled for the first quarter of 1977 but could not be done in time because GBR stopped transmitting in January for a longer period of time.

After GBR had started again, the phase measurements were conducted in St. Gertraudi mine / Tyrol. The measuring series proved to be correct because it was repeated twice.

The barage amplifier (1 kW maximum output) was used as the emitter in connection with the big loop (40x40 m, 10 windings) which was tuned to resonance by capacitors. Although there is a stopper circuit for the VLF frequency the current in the antenna (15 A) produces such a high magnetic field in the very near measuring points, that the ferrite rod antenna for the reception of the synchronizing GBR signal had to be oriented very exactly in minimum field strength direction of the VLF signal in order to prevent an overload of the input.

The measuring points were situated along the "West-schlag" gallery which is nearly parallel to the Inn valley. Table 4.1 gives the measuring results.
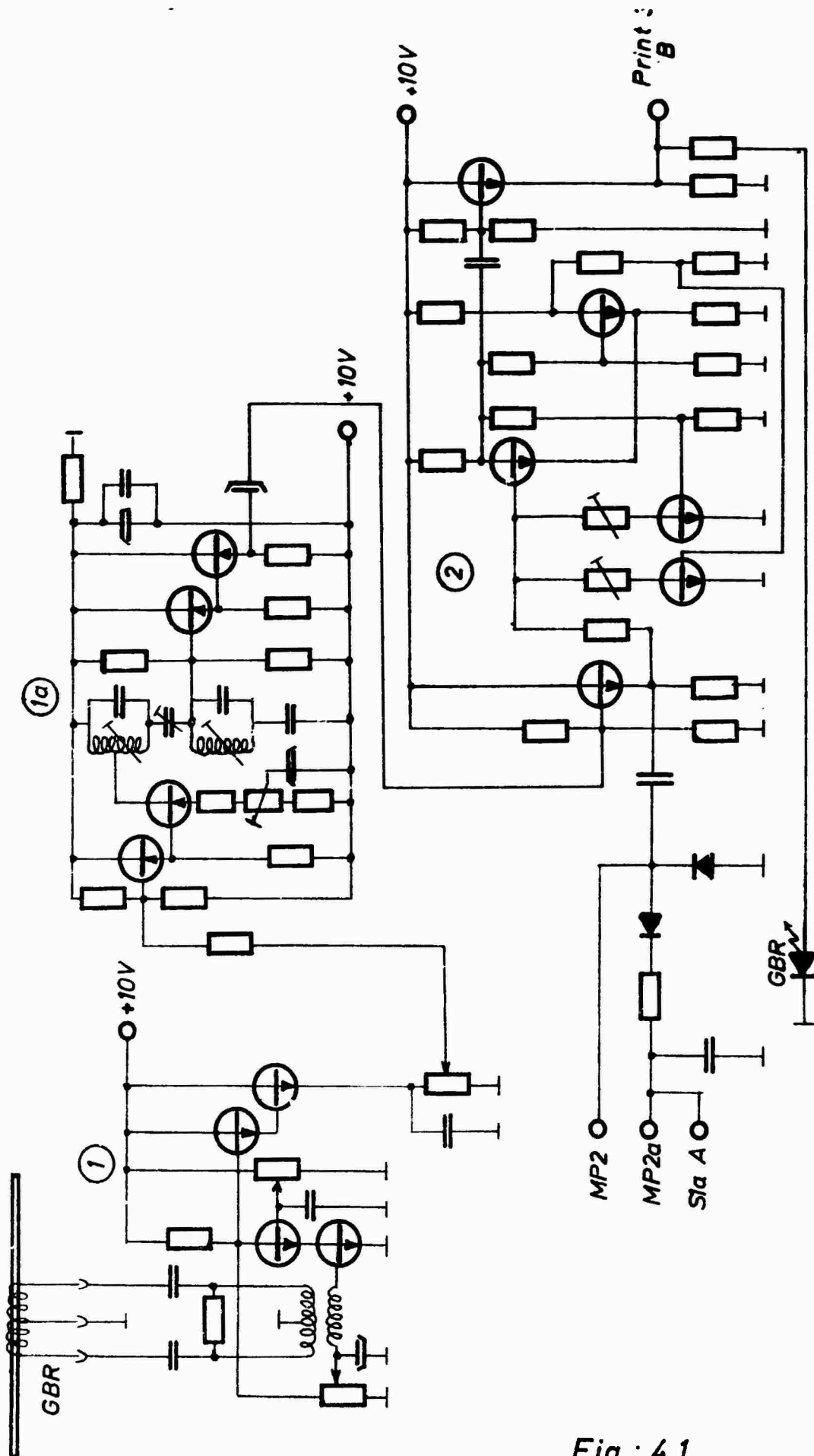
Fig.: 4.1
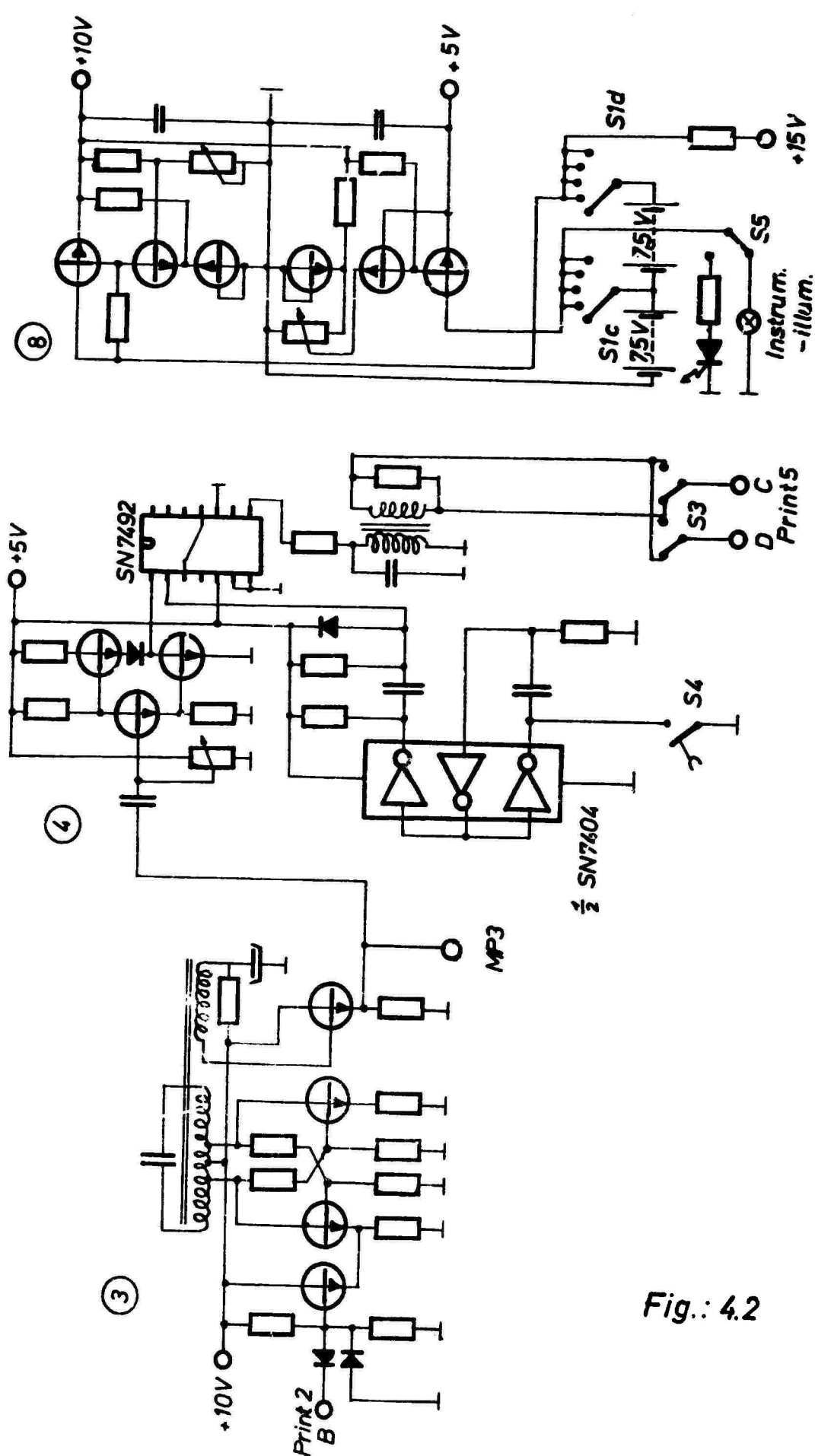
Fig.: 4.2
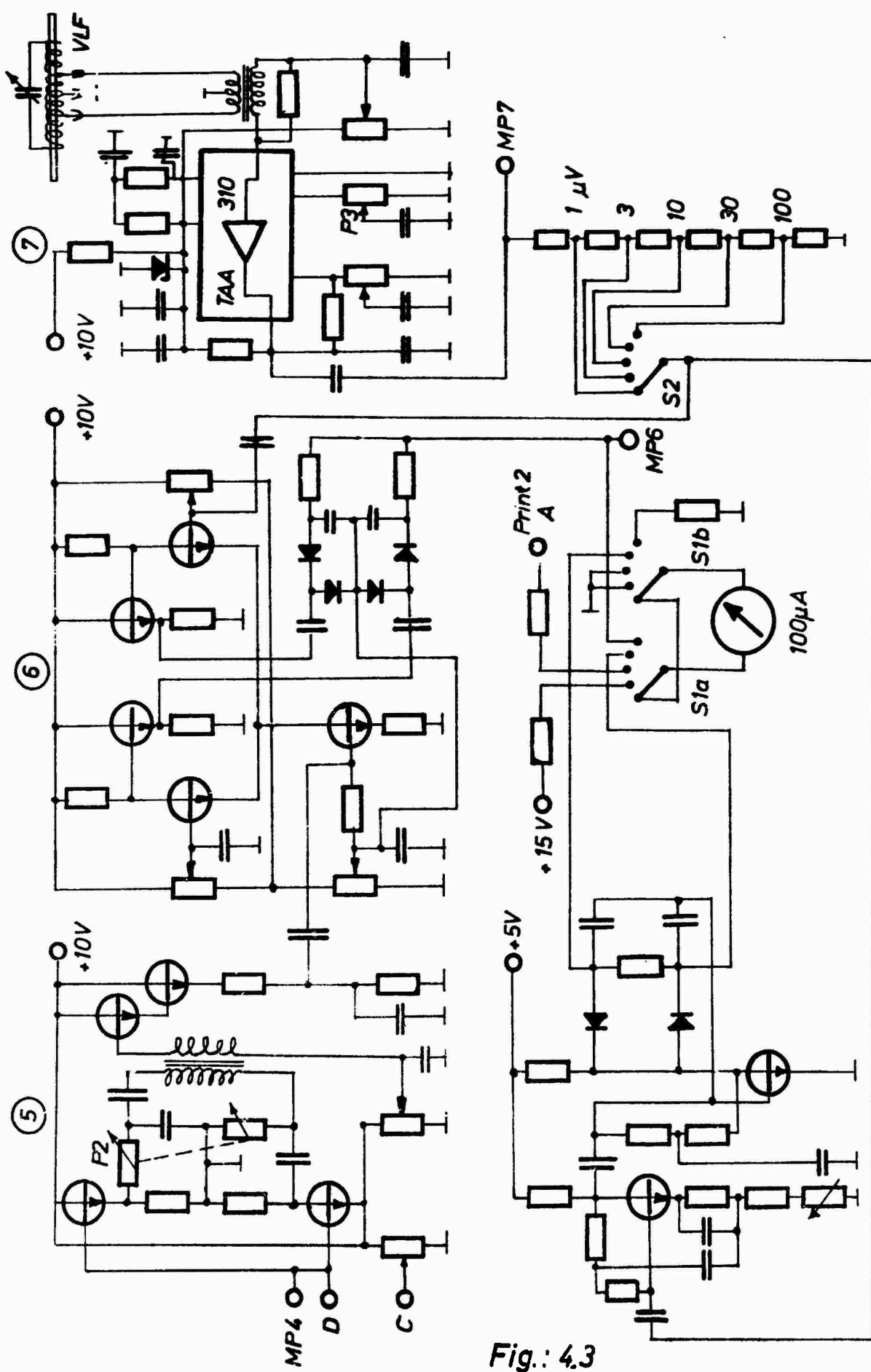
Fig.: 4.3
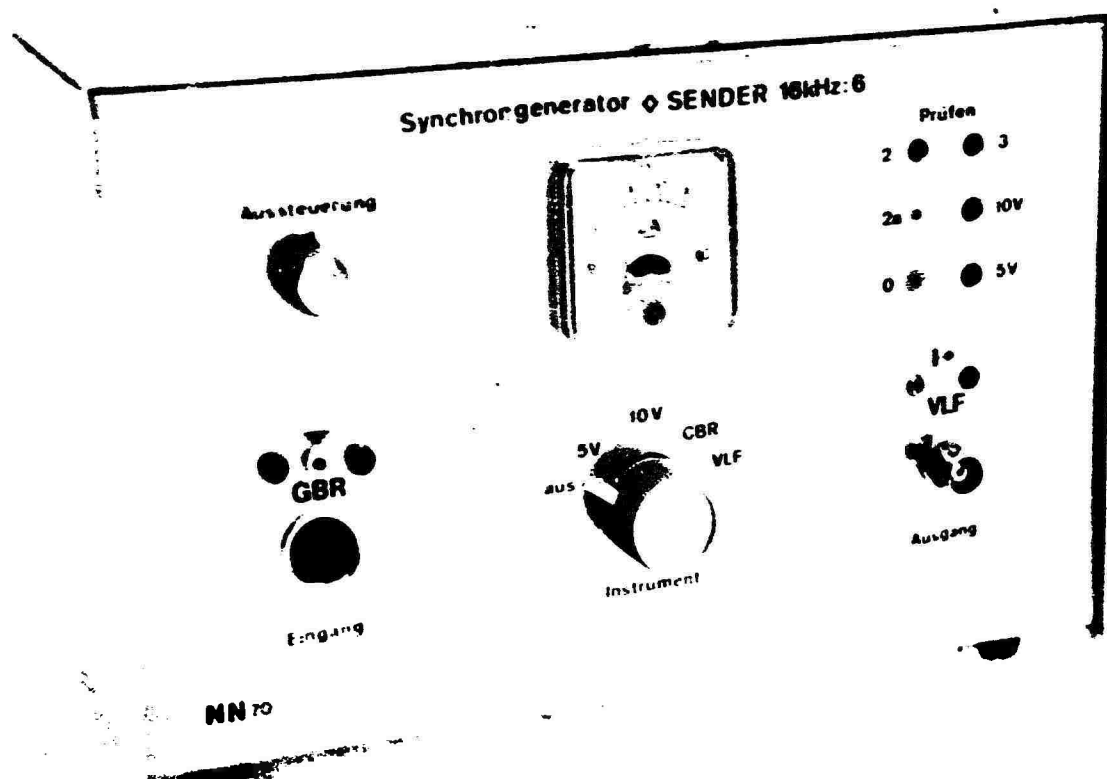
Bild C

Bild D
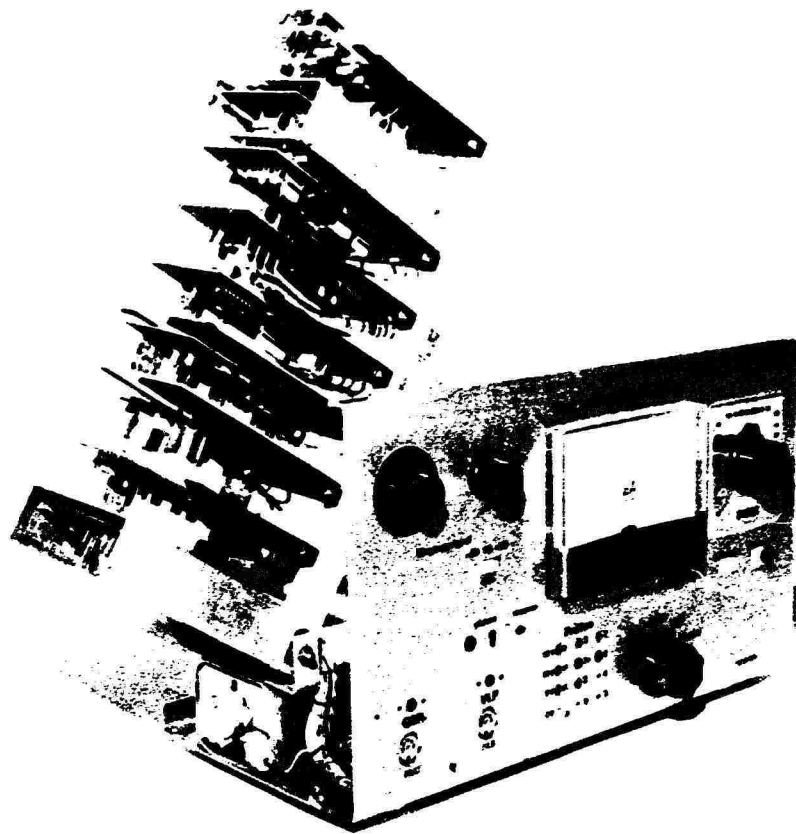
Bild E
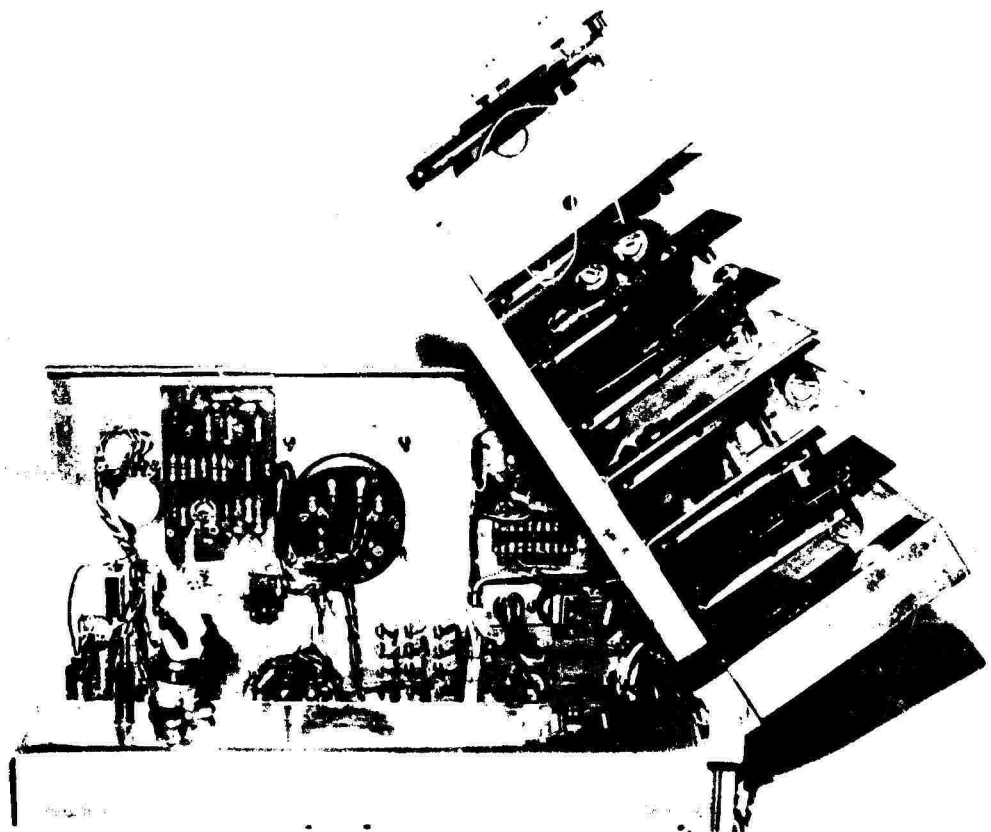
Table 4.1

d $|m|$	U_{VLF} $|\mu V|$	Phase $|°|$
100	27	20
150	21	15
200	14	15
250	7.4	15
300	5.0	20
350	2.5	20
400	1.9	20
450	1.5	25
500	1.1	30
550	0.9	20
600	0.77	18
650	0.63	22
700	0.54	15
750	0.47	0

d ..... distance between transmitter and receiver

U_{VLF} .. voltage proportional to received VLF signal

Phase . phase difference between synchronization
signal GBR and transmitted VLF signal reduced
modulo 60° (because of the 6 : 1 reduction of
the GBR frequency)

Result: Primarily it was assumed that the GBR incoming
direction is vertical to the line transmitter - re-
ceiver so that there is no phase difference between
these two points. Therefore the difference was ex-
pected to rise with increasing distance.

4.3 Conclusion

This phase measuring device measures the phase dif-
ference between the synchronization signal and the
VLF signal, and has the disadvantage that for measuring
the phase of one channel the phase shift of the other
channel must be known. If transmitter and receiver are
exchanged the phase shifts between VLF and GBR signal
can be added and subtracted, respectively. Thus, it is
possible to eliminate the phase shift of the GBR signal.
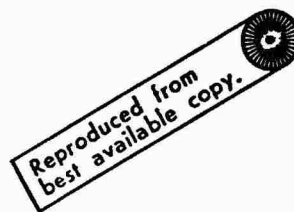
CHAPTER 5

A DIGITAL PHASE MEASURING DEVICE

5.1 Introduction

To be able to measure phases at the propagation of
electromagnetic waves in the VLF range a device was
developed by Dr. N. NESSLER /20/ showing the possibi-
lity of phase measurements within this frequency range
for the first time. For the synchronization between
transmitter and receiver a further external transmitter
was used. This existing equipment allows phase measure-
ments only at a certain frequency, and in some special
cases indication is amplitude-dependent. A new phase
measuring device comparing two incoming signals (measuring
signal and reference signal) completely independent on
frequency and amplitude is now being built.

The requirements which should be fulfilled by this de-
vice are rather high: current consumption must be very
small to enable battery operation; the device should
have little weight and volume and be insensitive to heavy
pushes and high atmospheric humidity to be able to be
operated in the mine; production cost must be kept low
(since the main part of the device is intended to be
used as well for a special measuring equipment of the
rotary field ellipse).

Thorough information showed that no commercial device
fulfills all these requirements, that is why it was con-
sidered most efficient to build it in our own laboratory.

The device is to indicate the phase digitally independent-
ly on amplitude and frequency within the frequency range

of 100 Hz - 100 kHz over a liquid crystal display
counting from -180° to +180°.

5.2 Basic construction

Fig. 5.1 shows the block diagram of the device without
a representation of receiving antennas and preamplifiers.
The two receiving signals the mutual phase position of
which is to be measured are connected to the inputs A
and B. The two Schmitt trigger units transform the sine
signal at the input to a square-wave signal with the
pulse duty factor 1 : 2 (pulse duration : pulse period).
The two square-wave signals are compared as to their
coincidence in the discriminator. The pulse duration
of the output signal at the discriminator is a direct
measure for the phase shift. In the logic unity this
phase-proportional signal cuts in a counting oscillator
(10 MHz) the number of pulses of which is counted. This
number within a definite time is a direct measure for the
phase angle independent on input amplitude and input fre-
quency and is indicated at the liquid crystal display.

5.3 Description of circuit
5.3.1 Input Schmitt trigger with null hysteresis

Fig. 5.2 shows the circuit for channel A. The sine signal
is connected to input A (about 30 mV$_{pp}$ - 5 V$_{pp}$). In the
upper branch an impedance transformer follows (T 1) and
connected thereto the one "half-Schmitt trigger". In the
bottom branch the sine signal is inverted by a T 2 and
the gain of the transistor is set to 1 by a P 3. The
succeeding T 3 works as an emitter follower and controls
the second half-Schmitt trigger. Such a half-Schmitt
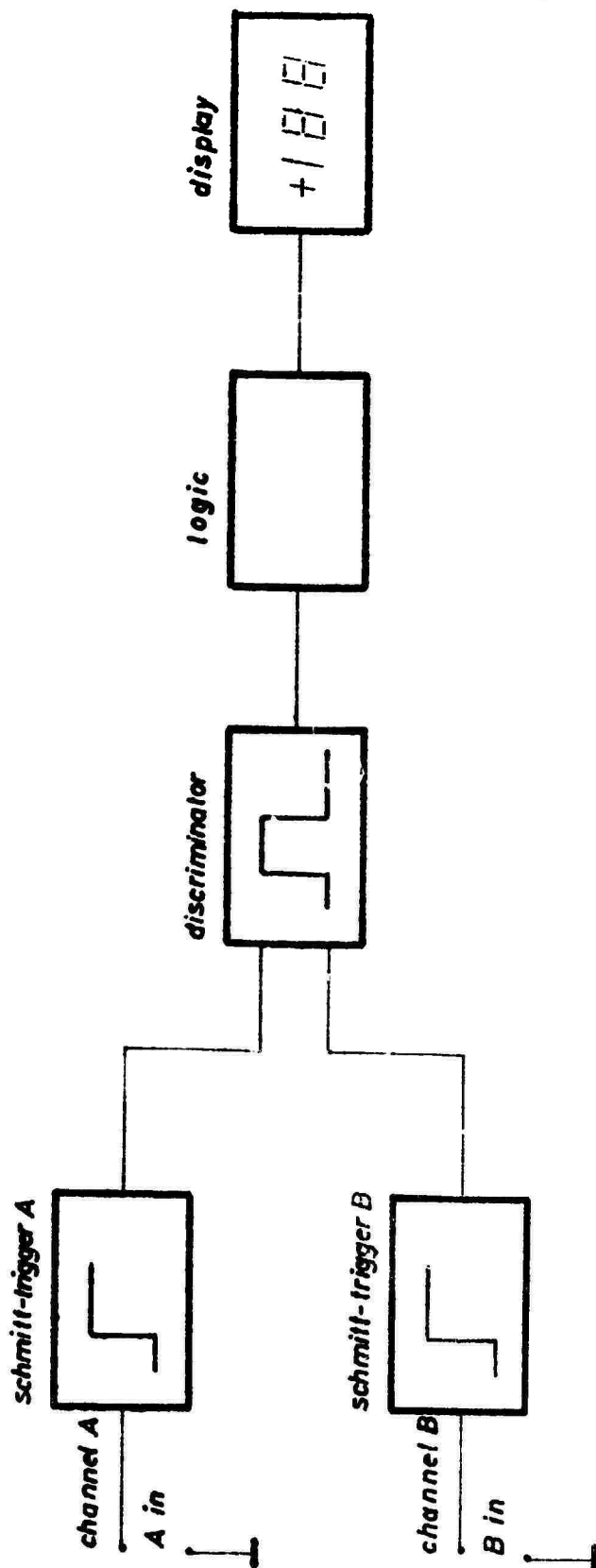
FIG. 5.1.
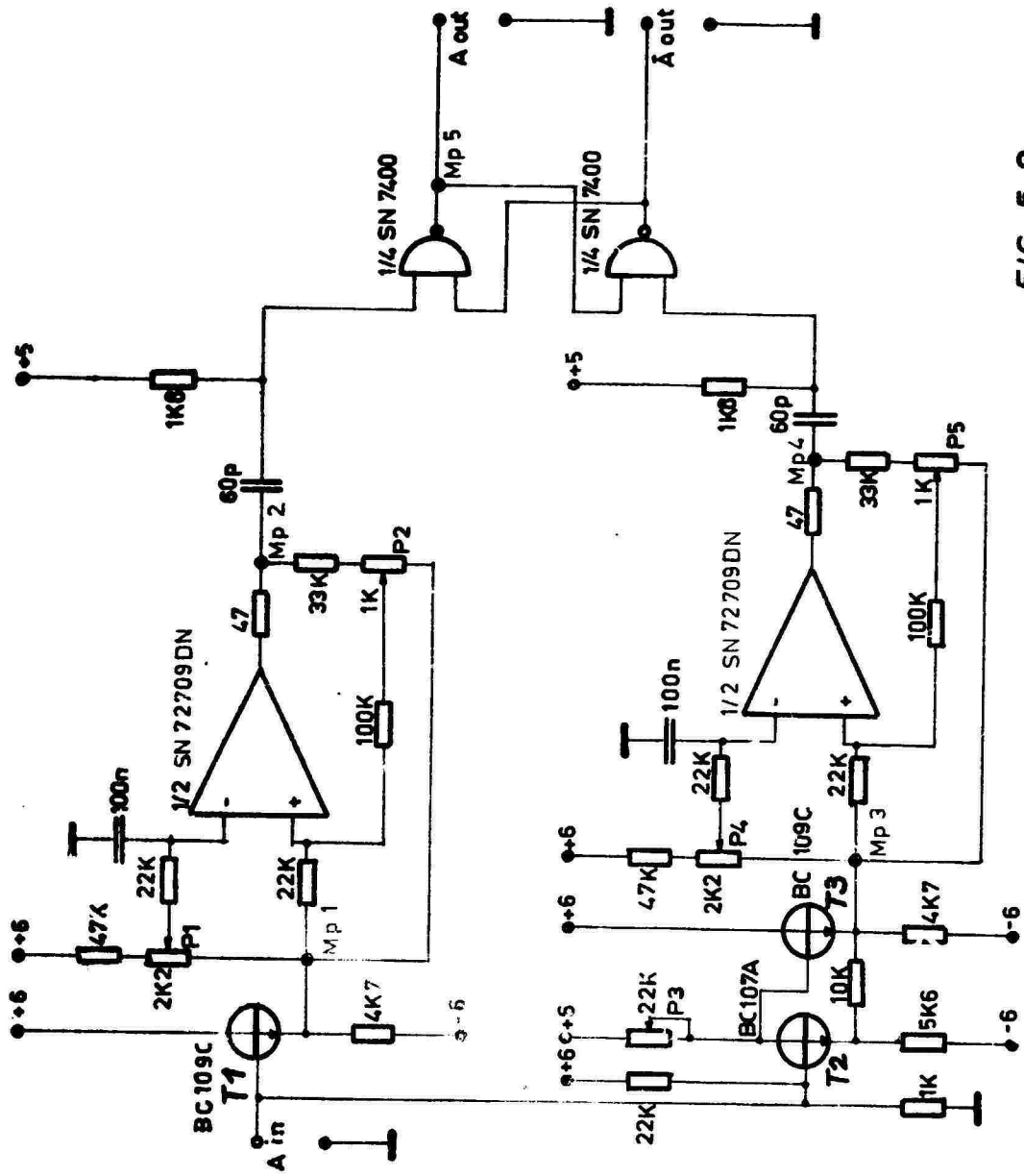
FIG. 5.2.
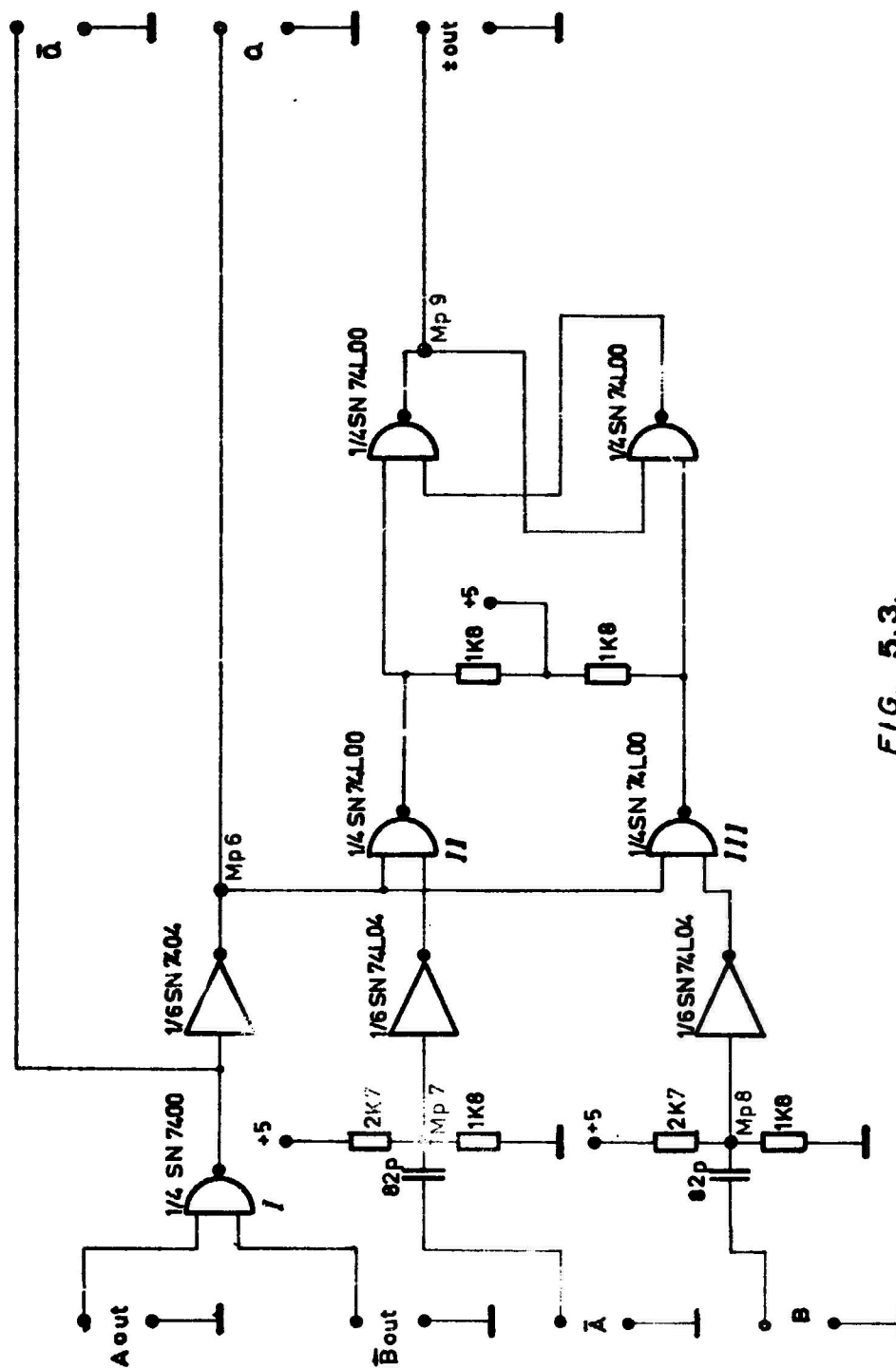
FIG. 5.3.
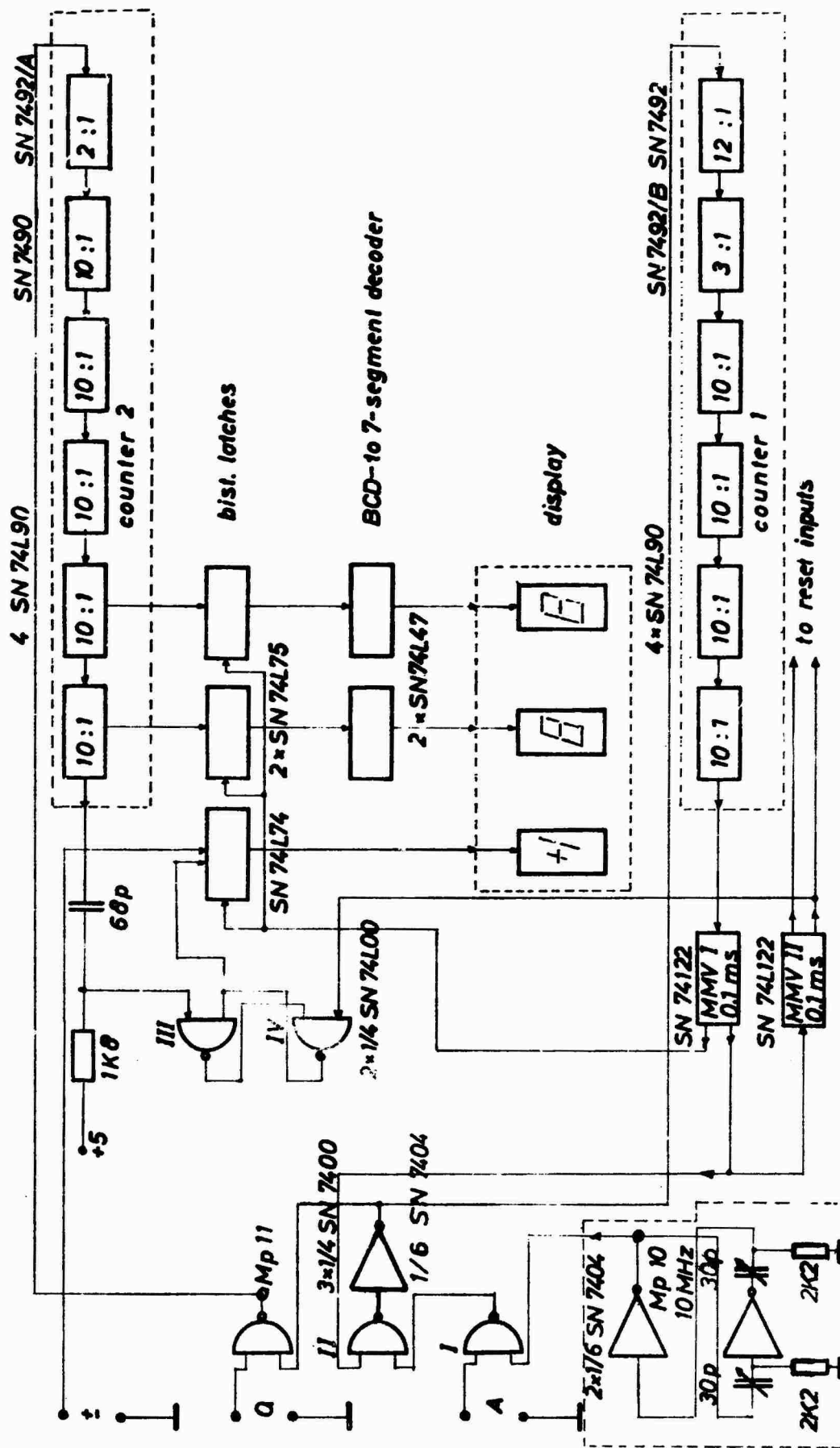
FIG. 5.4.

through. This interruption is necessary when the input-
signal becomes discontinuous as it is the case with
keyed transmitters. Counter 2 can reach 360000 at most
since the two counters only work when A = L (pulse duty
factor of A is 1 : 2).

After dividing this number by two and cancellation of
the last three decimal places the content of the counter
corresponds to the phase shift measured in angular
degrees. The end of one counting cycle sets the mono-
stable multivibrator I to a logical 'L' which blocks the
10 MHz clock pulse over NAND gate II. At the same time
the bistable latches are switched through. The first two
decimal places of counter 2 and the carry over of counter
2 are directly transferred to the indicator. The falling
slope of MMV I switches a second monostable multivibrator
(MMV II) to the quasistable position. Consequently all
counters and the flip-flop for the carry-over (NAND gates
III and IV) are zeroed; a new counting cycle can start.

The above described arrangement allows a phase indica-
tion independent of the input frequency and independent
of the 10 MHz clock frequency.

5.3.4 The display unit

A 2 1/2-place liquid crystal display (L.C.D.) is used
which has the advantage of an extremely low power con-
sumption (about $40 \mu W$/segment, i.e. less than 1/1000 of
the power requirement of a segment of an L.E.D. The drive
of the L.C.D. is more laborious than triggering the L.E.D.,
since the L.C.D. can only be operated by alternating
current from about 15 V_{eff} at 20 - 100 Hz. A special
circuit was now developed producing an a-c voltage of
60 V_{pp} which is shown in Fig. 5.5.

The a-c voltage is produced by a self-starting multi-vibrator /22/ oscillating at a frequency of about 80 Hz. The three coil windings were bridged by capacitors (C2, C3, C4) to avoid dangerous voltage peaks at the output. The output voltage becomes sinusoidal and nearly in-dependent on the load. This output voltage is now recti-fied over C5 and D1. With this circuit (Villard-doubling) the a-c-component is maintained but is increased by $1/2$ V_{pp} (pulsating d-c voltage between 0 V and 60 V). The transistors are special high-blocking types with $U_{CEO} \geq 60$ V. Only the a-c-component is coupled out over C6-C21 and laid onto the segment of the L.C.D.

By using this circuit we can operate the display with the required a-c voltage of about 20 V_{eff} and 80 Hz, which grants a high lifetime of the segments. At the development of this circuit it was taken into account to keep power consumption low. The current input for the whole display unit is not more than 3 mA at 5 V.

5.3.5 Power supply

The device is operated by 2 batteries. For the linear circuits a 12 V accumulator is used. The voltage of ± 6V for the operational amplifier is obtained by voltage di-vision. The logic is operated by a separate battery (Fig. 5.6). An estimation of the power consumption when using normal ICs showed, that the logic would take about 3300 mW. Consequently, it is advisable to use low-power ICs wherever possible to reduce power consumption to about one half. In spite of the high prime costs the use of low-power ICs is justified, since it will then be possible to take smaller and cheaper batteries and to reduce weight and volume of the device. Since the switching time of the 'L'-series is longer than that of the normal series, low-power ICs can only be used where the limiting frequency is below 1 MHz.
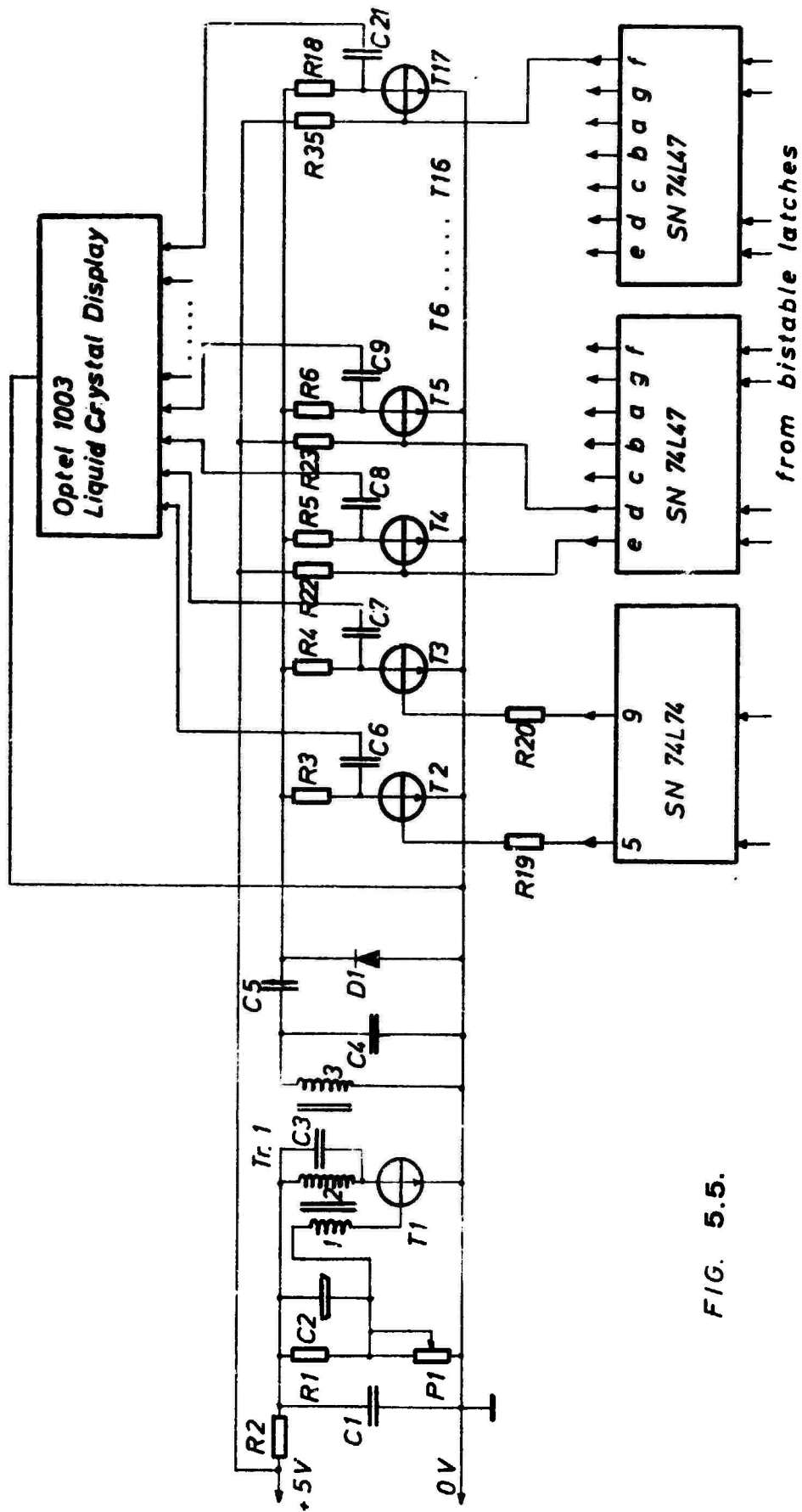
FIG. 5.5.
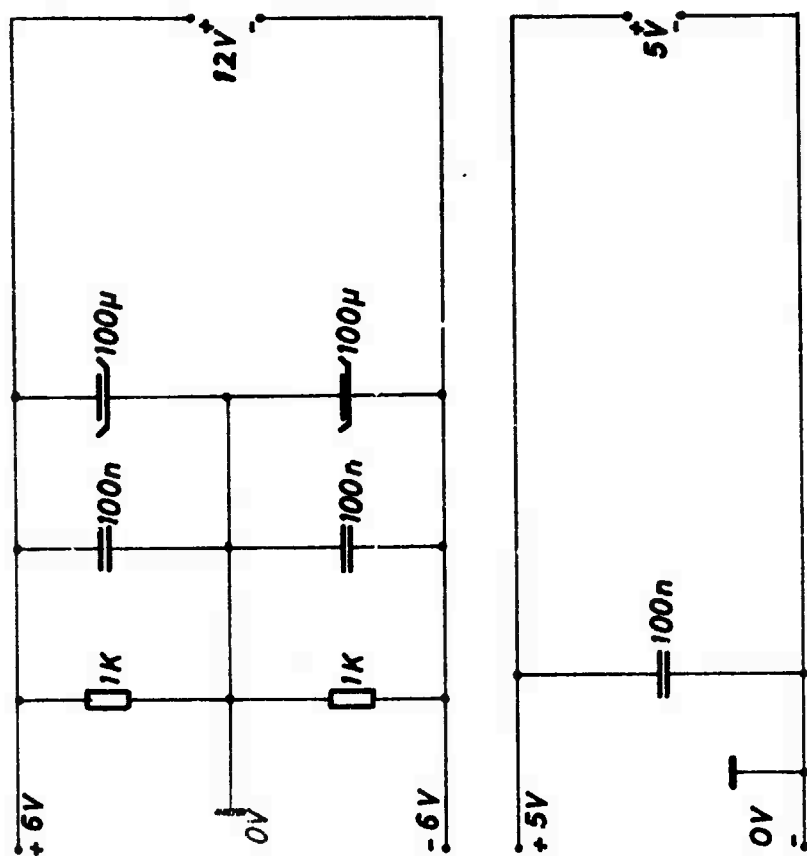
FIG. 5.6.
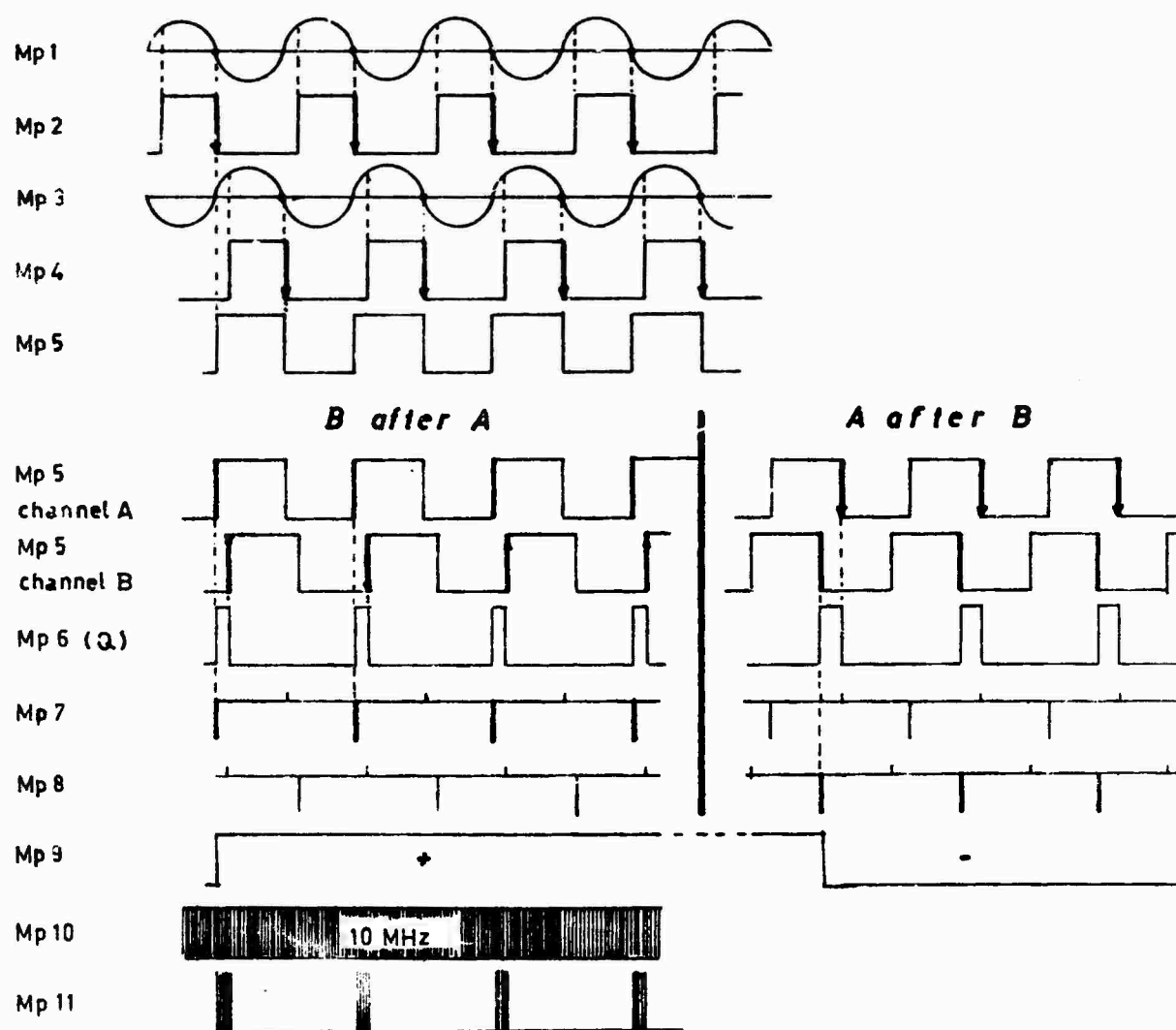
FIG. 5.7.

5.4 Error estimation

The kind of logic causes 2 errors to arise at counting the Q signal.

Error 1

At counting the Q signal by means of the 10 MHz signal the number of clock pulses has an inaccuracy of ± 1 pulse per impulse train (Fig. 5.8). During one counting cycle

$$n_1 = t \cdot v_1$$

t ... duration of a counting cycle (sec)

v_1 .. measuring frequency (Hz)

of such impulse trains occur. The content of counter 2 has a variation of $\pm n_1$ in the most unfavorable case.

Translated to angular degrees the indication error amounts to

$$\Delta\phi_1 = \pm t \cdot v_1 \cdot 360/a$$

$\Delta\phi_1$ .. error 1 (^{O})

a .... maximum content of counter 1
(in this case fixed to 360000)

With

$$t = a/v_2$$

v_2 ... clock frequency (Hz)

we have a final result for error 1

$$\Delta\phi_1 = \pm v_1/v_2 \cdot 360 \qquad (5.1)$$

This shows that the error depends only on the ratio of input frequency to clock frequency. An improvement can be reached by increasing the clock frequency. In the present device $v_2 = 10^7 = 10$ MHz.

As is shown in Table 5.2, error 1 is relatively large.
A control at the ready-built device, however, showed
the real error to be smaller than in Table 5.2 by one
order of magnitude, which is due to the fact that the
excess and the lack of counted pulses neutralize each
other. An exact calculation by means of calculus of
probability confirms this measurement result.

Error 2
Fig. 9 shows the formation of error 2; we can distinguish
three cases:

Case a) is the ideal case. In the impulse interval of
the impulse train the MMV rebounces to the stable state
thereby starting the counting cycle as soon as A = L.
Let the ratio of clock frequency to measuring frequency
be a whole-number multiple modulo 360,000 of frequency A,
so that after a definite number of complete impulses A
360,000 clock impulses were counted in counter 1. This
means that every complete impulse train of the duration
t1 corresponds to a complete impulse train τ. Since the
ratio t1 : τ which is proportional to the phase is
maintained, no error of the second type arises in this
case.

Case b) Let the frequency of A be somewhat smaller than
for case a, so that the 360,000 impulses of counter 1
do not completely fill up the impulse groups A. Let the
counting cycle - turned on by the MMV - start just at
that moment when the impulse group τ in counter 2 cor-
responding exactly to a block t1 is over.

Case c) Let the frequency of A be slightly larger than
in case a, so that the 360,000 impulses of counter 1
need a bit more time than is corresponding to an integral
number of impulses A.   We may have the case that at

FIG. 5.8.
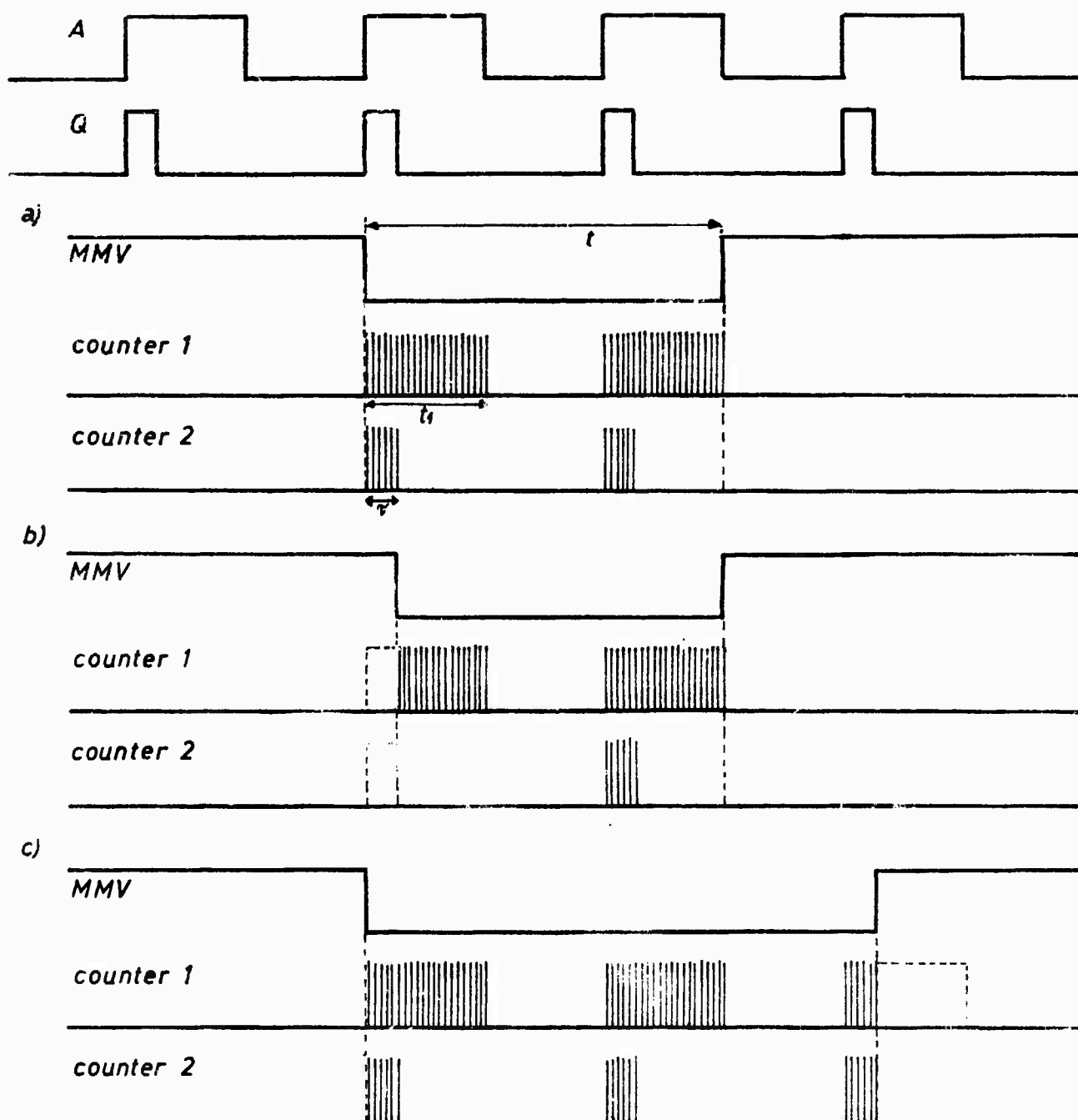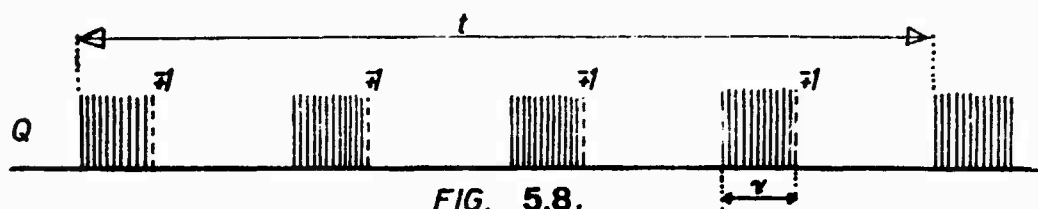
FIG. 5.9.

starting the counting according to case a) we count just
one additional impulse train τ in counter 2, whereas the
corresponding impulse group t1 in counter 1 is not
counted completely.

Calculation

To be able to conduct calculations the impulses coming
under the period τ must be distributed equally to the
time t1. Therefrom we can calculate the lack (case b)
or the excess (case c) of impulses in counter 2.

Case b: At first we calculate the number of impulses n
that were missing in counter 2 in relation to counter 1

$$n = \frac{\tau}{t1} (t_1 - \tau) \nu_2$$

From the definition of the impulse width τ

$$\tau : 2t_1 = \phi : 360$$

we get with

$$\Delta\phi_2 = n \cdot \frac{360}{a}$$

the equation for error 2

$$\Delta\phi_2 = \left(\phi - \frac{\phi^2}{360}\right) \frac{\nu_2}{\nu_1} \cdot \frac{2}{a}$$

$\Delta\phi_2$ ... error 2

ϕ ..... phase position

ν_1 .... measuring frequency

ν_2 .... clock frequency

a ..... maximum content of counter 1

For case c) the same calculation holds, but the error
is negative.

At the device described here the following values were

fixed for a and v_2

    a 360,000

    v_2 . . . 10^7 Hz

From Eq. (5.2) follows that this error becomes smallest

When either a becomes very high or the ratio of block

frequency to measuring frequency decreases.

Table 5.2 shows the values of the two errors in dependence

on phase and measuring frequency.

Table 5.2

v_1 |Hz|	ϕ |°|	$\Delta\phi_1$ |°|	$\angle\phi_2$ |°|
10^3	3.6	± 0.036	± 0.2
10^3	180.0	± 0.036	± 0
10^4	3.6	± 0.36	± 0.02
10^4	180.0	± 0.36	± 0
10^5	3.6	± 3.6	± 0.002
10^5	180.0	± 3.6	± 0

As can be seen from Fig. 5.9, error 2 is zero at 180°

and increases with decreasing phase.

It is to be mentioned that the duration of a counting

cycle is $3.6 \cdot 10^{-2}$ sec; this time can be easily increased

as required by means of the two MMV in Fig. 5.4.

CHAPTER 6

VALLEY MEASUREMENTS

The above-ground registration of VLF signals showed the
maximum magnetic field strength always to run in direc-
tion of the mountain valleys. This effect obviously
does not occur by chance because it could be proved in
all by-valleys of the Inn-Valley. A thorough explanation
will be given in a particular thesis.

In spring 1972 we started preparatory measurements.
Several frequencies were considered (15.1; 50; 128.25;
278 kHz) to be able to recognize a possible frequency
dependence. In fact, a new unexpected effect occurred.
For the higher frequencies the maximum magnetic field
strength was always normal to the valley direction. Fig. 1
shows these results. The contour lines show the course of
the valleys in the surroundings of Innsbruck and the vec-
tors show the direction of the maximum magnetic field
strength. If the valleys become too narrow all vectors
point into valley direction.

For a hollow waveguide the mode with the greatest wave-
length is a TE-mode, i.e., a mode with the maximum magne-
tic field strength following the waveguide axis. So we
tried to interprete the effects by a modified waveguide
theory. The only difficulty was to recognize the valleys
as hollow waveguides. In several publications /23, 24,
25/, the problem of waves over rough surfaces is solved by
expanding the irregularities of the surface in Fourier-
series. The wave equations are solved for sinoidal
modulated surfaces and then superponed. It is evident that
surface irregularities will induce new modes.

In /24/ we find waveguides of arbitrary cross section
being transformed into cylindrical waveguides by means
of conformal mapping. The problem now appeared rather
restricted: The shape of the valley has to be transformed
to a cylinder.

w = f(z)
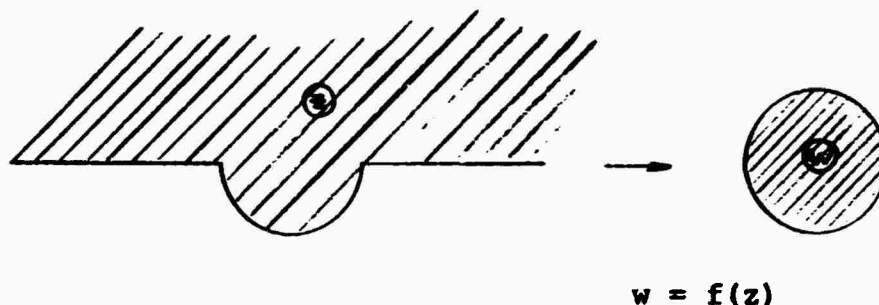
Fig. 6.2

The exact solution requires considerable numerical
expenditure. Besides, there is no plotter at Innsbruck
University so that the results cannot be plotted. For
the time being we have to be satisfied with an approxi-
mate solution which, however, shows good physical clear-
ness.

The transformation:
By means of the function $w = \dfrac{z-i}{z+i}$ the upper semi-plane
is represented onto the unit-circle of the w-plane
/18, 26/.

$$w = \frac{z-i}{z+i}$$
Fig. 6.3

a : 15.1 kHz   b: 50 kHz
c : 128.25"   d : 278 °
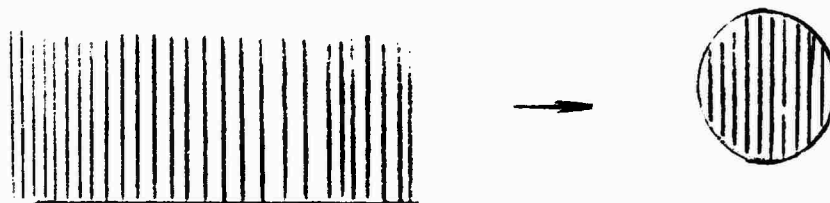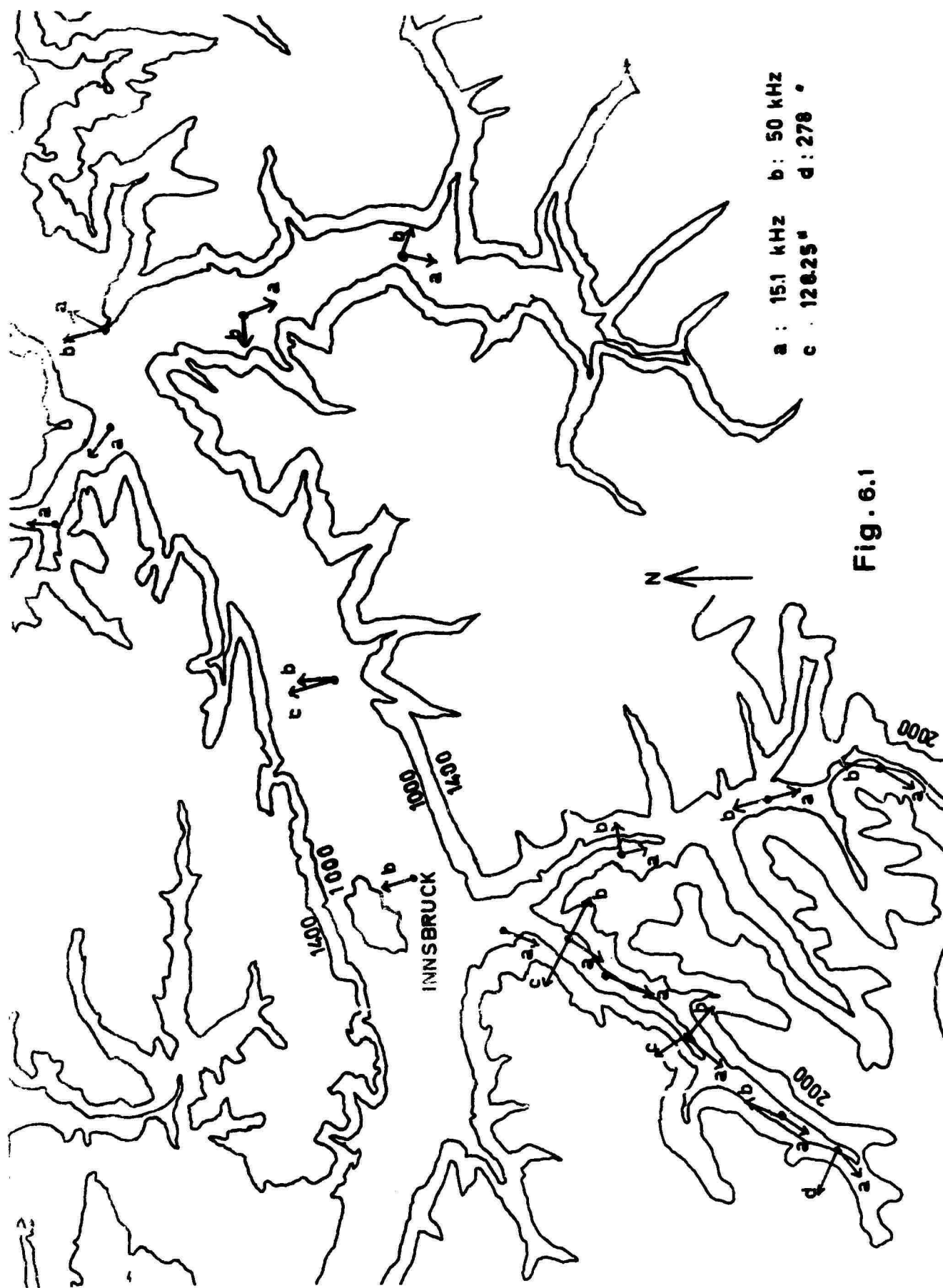
Fig. 6.1

We choose our valley cross section in a way that it falls completely into the upper semi-plane.

$$w = f(z)$$
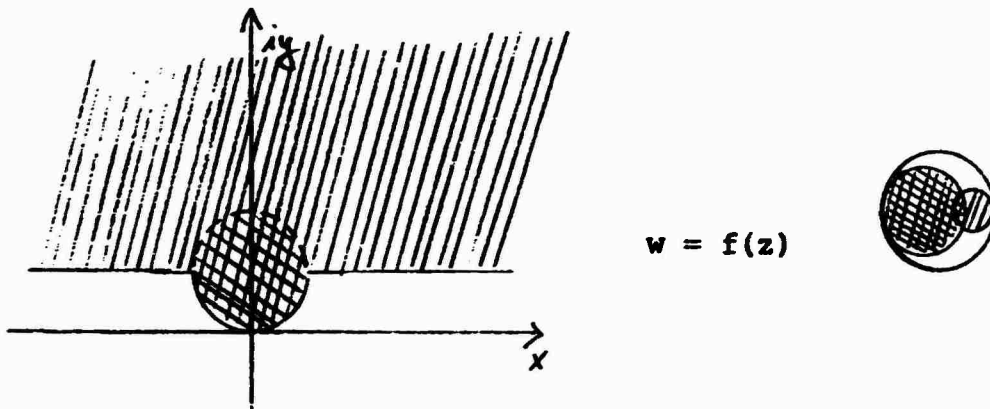
Fig. 6.4

Now the valley is transformed into the interior of two intersecting circles inside the unit circle which depend on the valley size.

Waveguides still can be described by the eigenfunctions of cylindrical waveguides, if the cross section varies slightly from a circle /24/. In our case, this means that the problem is solved principally when the valley is represented onto a fairly circular area.

The representation function reads

$$w = \frac{z - i}{z + i} \qquad (6.1)$$

The circle

$$|z - ia|^2 = a^2 \qquad (6.2)$$

in the z-plane is transformed into the circle

$$\left(u + \frac{1}{1 + 2a}\right)^2 + v^2 = \frac{4a^2}{(1 + 2a)^2} \qquad (6.3)$$

in the w-plane.

For the straight line $Im(z) = b$ we obtain in the w-plane

$$\left(u - \frac{b}{1+b}\right)^2 + v^2 = \left(\frac{1}{1+b}\right)^2 \qquad (6.4)$$

Considering e.g. the case a = b = 3, an approximately circular representation of the valley results in the w-plane. The concentric circles to the circle K in the w-plane are representing coordinate lines in the hollow waveguide.

$$\left|w + \frac{1}{7}\right|^2 = c^2 \qquad (6.5)$$

The inverse transformation of these circles produces

$$\left|z - \frac{48 + 49c^2}{64 - 49c^2}\right|^2 = \frac{7252c^2}{(64 - 49c^2)^2} \qquad (6.6)$$

in the z-plane. These circles are shown in Fig. 6.5.
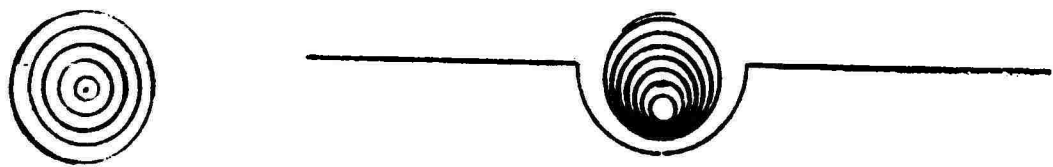
Fig. 6.5

The same results are obtained when using other values for a and b. So we can say that the transformation is independent on the size of the valley.

Conclusion

It is possible to describe a mountain valley by a cylindrical waveguide by means of conformal mapping. From Fig. 6.5 it is to be seen that near the bottom the field density is higher than in the upper regions of the valley.

An exact transformation of the valley cross section into a cylindrical waveguide is possible, but requires a computer with plotter because of the great numerical expenditure.

CHAPTER 7

A NEW METHOD OF DETERMINING
THE ELECTRIC ROCK PARAMETERS ϵ_r AND σ

7.1 General considerations

The procedures of determining ϵ_r and σ listed below are
based on the dependence of the field strength on

1) the dipole moment $\vec{m}$
2) the distance R between point of reception and
   transmitter
3) the frequency f
4) the dielectric constant ϵ_r
5) the conductivity σ

$$\vec{H} = \vec{H}(\vec{m}, r, f, \epsilon_r, \sigma) \tag{7.1}$$

$\vec{H}$ ... magnetic field strength vector

To restrict this complexity it is necessary to conduct
the measurement in a way that as many of these parameters
as possible are kept constant.

Furthermore, we have to consider the problem whether
and how much the individual parameters depend on each
other.

a) Since $|\vec{m}| = n \cdot I \cdot F$ can always be kept constant by read-
   justing the antenna current, the dependence

   $$|\vec{m}| = |\vec{m}|(\epsilon_r, \sigma)$$

   that might possibly arise by attenuating the trans-
   mitting antenna operated in resonance, is only of
   theoretical interest for our case.

b) It is obvious that

$$\epsilon_r \neq \epsilon_r(\vec{m}); \quad \sigma \neq \sigma(\vec{m}); \quad f \neq f(\vec{m}); \text{ and } R \neq R(\vec{m})$$

c) The question for the dependence

$$\epsilon_r \overset{?}{=} \epsilon_r(R) \quad \text{and} \quad \sigma \overset{?}{=} \sigma(R),$$

however, has to be discussed more thoroughly which is to be illustrated by means of the following figures (Figs. 7.1a and 7.1b).
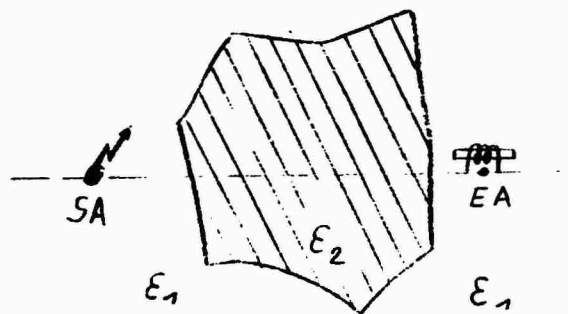
Fig. 7.1a

In the first case (Fig. 7.1a) transmitter and receiver are so close together that solely the dielectric constant ϵ_1 of the inhomogeneous island in between holds responsible for the field at the point of reception. If the measuring distance is enlarged the surrounding medium characterized by ϵ_2 becomes more and more effective. The resulting dielectric constant ϵ_{res} influencing the field of reception is composed of ϵ_1 and ϵ_2. Fig. 7.1b will illustrate this situation. It was on purpose that all disturbing bodies were drawn with equal magnitude and shape to make clear then even then ϵ_{res} is depending on the distance. In reality these islands will be of different size and have a different dielectric constant, too.

The distance dependence for ε_r and σ (of course, we can reflect in the same way on the conductivity) can thus be regarded as a fact. The dielectric constant (or conductivity, respectively) determined over a certain measuring distance is a mean value of all dielectric constants (or conductivities) of this region.

It is therefore senseless to compare specific values of dielectric constant (or conductivity), unless they are related to a certain distance. Consequently, listed values given by different authors can only be regarded as approximations and it is necessary to compare measuring methods and conditions, too.

d) The dependence

$$\varepsilon_r \overset{?}{=} \varepsilon_r(f) \quad \text{and} \quad \sigma \overset{?}{=} \sigma(f)$$

is of great importance with regard to the two-frequency method discussed below. The frequency dependence of ε_r and the consequent dependence of the index of refraction on the frequency is called "dispersion" in optics. In this case, however, wavelengths involved are so small that they can be compared with molecules and resonance vibrations occur. At low frequencies there are no such vibrations; the approximate limit lies at about 30 MHz ($\lambda_0 = 10$ m, SW-band). Below this frequency, calculations are performed with the static value of the dielectric constant.

In contrast to this assumption a certain frequency response was observed in the lower frequency range ($f < 100$ kHz) owing to the so-called partition polarization. Among others, STRUTT /27/ and recently WÖBKING /28/ and GRISSEMANN /29/ have observed this phenomenon. In /28/ and /29/, the (ε_r,f) and the (σ,f)-diagrams show a flattening of the curves towards higher frequencies ($f > 100$ kHz)
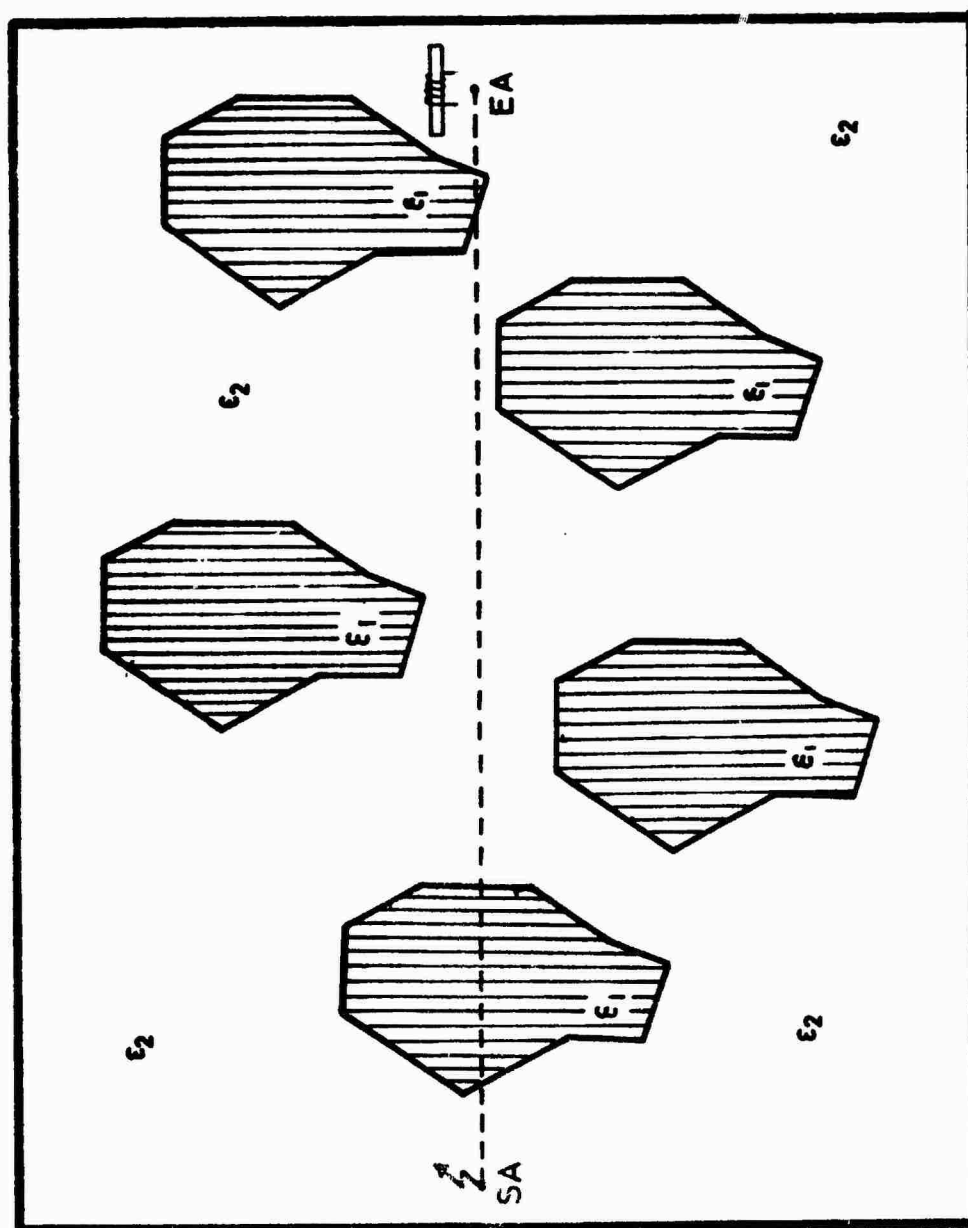
FIG. 7.1b

Whether or not the two-frequency method is admissible for the determination of ε_r and σ depends on the above conclusions.

For a comparison let us briefly refer to methods that have already been worked out by co-workers of the VLF-Project:

7.2 Method according to NESSLER /10/

If the relative value G (to be defined below) is plotted as ordinate for a definite frequency and a definite measuring distance every point in the diagram will constitute a pair of values (ε_r, σ) belonging together. To obtain H_{90} we must know exactly the properties of the receiving equipment, and the calibration factor establishing the interrelation between actual field strength and measured voltage must be determined as accurately as possible. Since the calibration factor comprises quite a number of measuring values, the uncertainty factor is rather high. The resolving power of the method is, however, good even at small measuring distances of about 20 m.

7.3 Method according to KELLNER /14/

Based on an adequate representation of the formulas for the vector components of the field strength, KELLNER /14/ found a possibility to determine the complex wave number from relative values and thereby calculate ε_r and σ.

The main disadvantage of this method is its failure in the inhomogeneous measuring site. According to the author, the method can only be used up to a frequency of about 350 kHz and a measuring distance of 50 m. This is due to the fact that with decreasing wave length the inhomogeni-

ties form an ever increasing hindrance for the field
which thus is more and more distorted. It is chiefly the
bearing angle ψ indicating the direction of maximum field
strength and playing a dominating role in the evaluation
formulas that is distorted, thus heavily falsifying the
result.

7.4 New Method according to KLEIN /17/
Two-frequency method

To be able to make quantitative statements on the beha-
vior of electromagnetic waves penetrating zones of in-
homogenity it is necessary to know the electric rock
parameters ε_r and σ. Real and imaginary parts of the com-
plex wave number k^* and of the complex refraction index
n^* can be calculated from these parameters. Therefore we
had to find a method delivering workable results even in
an inhomogeneous medium.

The following requirements had to be fulfilled:

1) The method must be practicable in inhomogeneous medium.
2) In its formulas and diagrams it should contain only
   quotients of absolute measuring values.

A favorable application of a possible method made us
request two more conditions:
3) Measurements should be able to be conducted easily
   and quickly.
4) The values ε_r and σ to be determined should possibly
   be readable at the measuring site thus enabling a
   short-time change in the measuring program.

A solution of these problems was found using the field
strength ratio G (as was done with the two methods
described above) considering, however, two different

measuring frequencies. According to /10/ G is defined
as

$$G = \frac{H_0}{H_{90}} = \frac{H_R}{H_\theta} \tan \theta \qquad (7.2)$$

H_0 ... field strength maximum at $\theta = 0^0$

H_{90} .. field strength maximum at $\theta = 90^0$

H_R ... field strength in the direction towards the
transmitting antenna

H_θ ... field strength vertical to H_R

θ ... angle between transmitting antenna and
radius vector

Since the field strength vector $\vec{H}$ and thus all its com-
ponents depend on frequency, dielectric constant, con-
ductivity, and distance to the transmitter

$$G = G(f, \ \epsilon_r, \ \sigma, \ R)$$

Owing to the above mentioned reasons the measuring distance
transmitter - point of reception must be kept constant, i.e.

$$G = G(f, \ \epsilon_r, \ \sigma)$$

The above mentioned frequency independence of ϵ_r and σ
at one and the same measuring distance reduces the de-
pendence of G to

$$G = G(f)$$

at ϵ_r = const. and σ = const.

If groups of curves with the parameters ϵ_r and σ, resp.,
are plotted in a diagram with the ordinate $G = G(\epsilon_r, \sigma)$
at a frequency f_1 and with the abscissa $G = G(\epsilon_r, \sigma)$ at
a frequency f_2, every point of intersection of the
ϵ_r-parameter group with the σ-parameter group constitutes
a (ϵ_r, σ)-pair of values belonging definitely together.

For our measurements, the following values were chosen:
f_1 = 500 kHz; f_2 = 1000 kHz; R = 100 m (50 m), thereby
taking into consideration the geometry of the gallery,
the resolving power at a definite measuring distance
(splitting of the curves of the diagram), and the power
of the transmitter. For G(500) (i.e. G at 500 kHz) and
G(1000) (i.e. G at 1000 kHz) determined by measurement,
dielectric constant and conductivity can be taken from
Fig. 7.2. For other measuring distances and frequencies
corresponding diagrams have to be plotted.

There are three possibilities to measure G:

a) With the relation

$$G = \frac{H_R}{H_\theta} \tan \theta$$

any angle position θ of the transmitting antenna is
admissible. For $\theta \to 90°$, $\tan \theta \to \infty$, i.e., the determi-
nation of G becomes inaccurate for large values of θ.

b) If = 45°

$$G = \frac{H_R}{H_\theta}$$

thus considerably reducing measuring expenditure,
because only the frequency has to be interchanged.

c) Using the relation

$$G = \frac{H_O}{H_{90}}$$

the transmitting antenna is first adjusted to $\theta = 0°$
and then to $\theta = 90°$. At both positions the maximum
field strength is measured for both frequencies.

Out of these three possibilities it is the third one that
offers the decisive advantage in comparison to the methods
by NESSLER and KELLNER.

FIG. 7.2
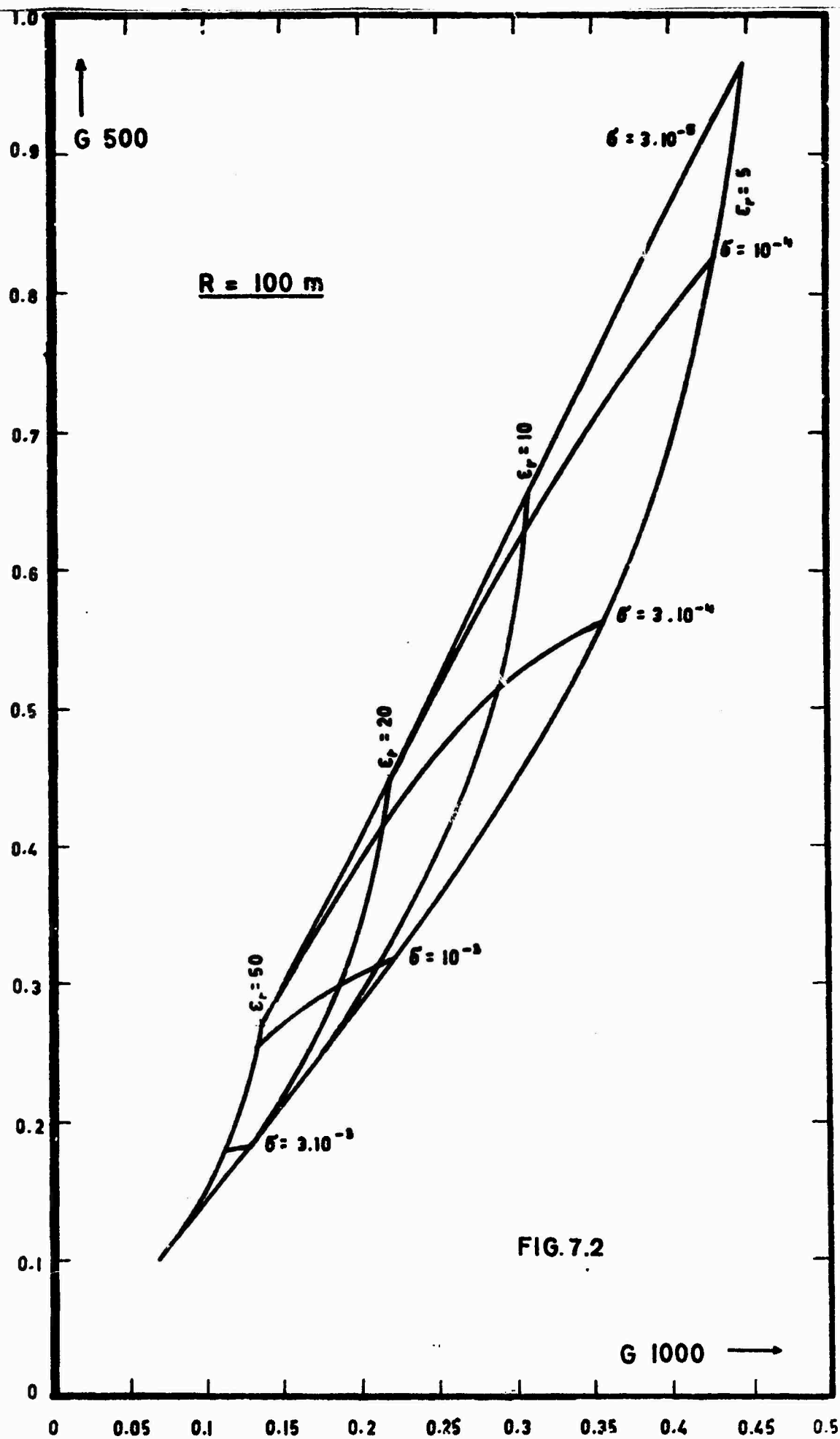
Both for $\theta = 0^O$ and for $\theta = 90^O$ the field is linearly polarized. When measuring, the H_O and H_{90} directions are sought and the amount is measured. That is why a deviation owing to disturbances can by no means influence the accuracy of the value $G = H_O/H_{90}$.

7.5 Practical application of the new method

Numerous measurements were executed in the mine of St.Gertraudi. Whereas for most measuring sites a homogeneous rock structure could be assumed, the measurements in "Morgenschlag" produced (cf. Fig. 7.3) surprisingly different values; results are listed in Table 1.

Table 1: R = 100 m

exp. no.	measuring distance	f [kHz]	U_0 [µV]	U_{90} [µV]	G(500) G(1000)	ε_r	σ [S/m]
97	M8.2 - M12	500 1000	290 78	880 420	0.33 0.19	20	$9 \cdot 10^{-4}$
101	M12 - M8.2	500 1000	505 165	1300 810	0.39 0.21	20	$5 \cdot 10^{-4}$
100	M11.3 - M9	500 1000	490 108	790 390	0.62 0.28	12	10^{-4}
104	M9 - M11.3	500 1000	485 120	780 400	0.62 0.30	10	10^{-4}
99	M11.3-M11	500 1000	125 55	138 143	0.91 0.39	8	$6 \cdot 10^{-5}$
103	M11-M11.3	500 1000	445 120	610 360	0.73 0.33	8	$8 \cdot 10^{-5}$
98	M11.3-M12	500 1000	530 92	510 205	1.04 0.45	4	$2 \cdot 10^{-5}$
102	M12-M11.3	500 1000	480 85	510 210	0.94 0.41	6	$5 \cdot 10^{-5}$

The number of experiment refers to Fig. 7.3. On comparing exp. no. 97 with exp. 98 perpendicular thereto we realize that the two dielectric constants are 5 : 1, the conductivities, however, nearly 50 : 1. From these remarkable differences we can draw the conclusion that a disturbance runs through the medium. The recognition of such disturbances means a real advantage for geological prospecting. The method described above together with the method of images thoroughly discussed in /17/ has already produced promising results.

7.6 A further possibility to locate disturbing zones in rock

The following characteristic resulted from the forementioned measurements for the determination of the electric rock parameters ϵ_r and σ in "Morgenschlag":

At the execution of measurement 106 (78) (cf. Fig. 7.3) from M8.2 to M12 the direction of maximum field strength (major axis of receiving ellipse) rotates by 180° together with the rotation of the transmitting antenna whereas at measurements perpendicular thereto the maximum field strength shows some kind of pendulous motion. The rotation occurring in one direction up to a certain angle of rotation θ of the transmitting antenna suddenly reverses so that the receiving antenna tilts back to the starting position without having done a 180°-rotation.

Fig. 7.4 illustrates quite clearly this extraordinary behavior. The curves do not proceed - as could be expected from theory - from the first to the third quadrant, but from the first to the second one at the forward measurement and from the fourth to the third quadrant at the backward measurement (with exchanged transmitter and receiver).
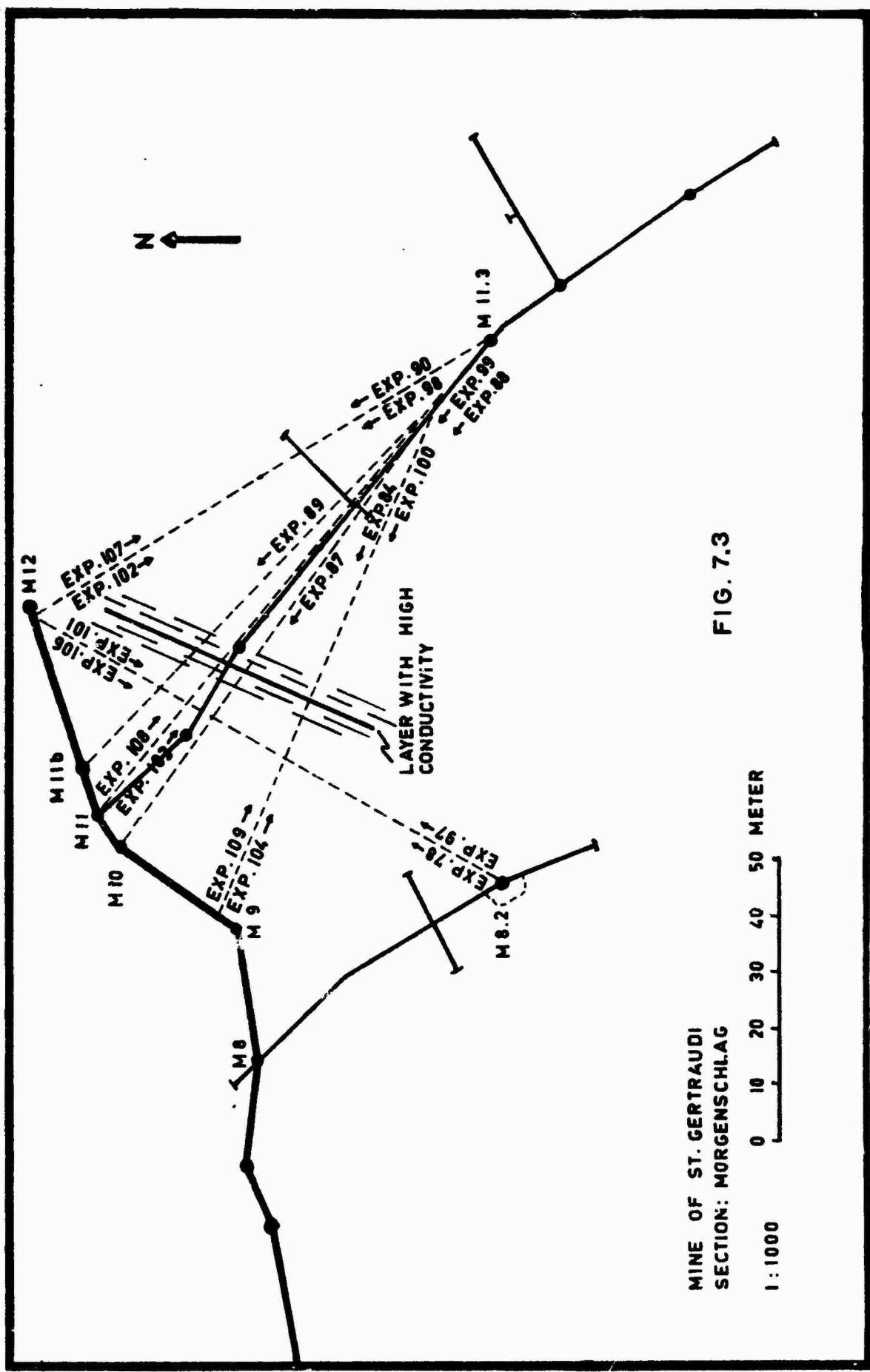
MINE OF ST. GERTRAUDI
SECTION: MORGENSCHLAG

1:1000

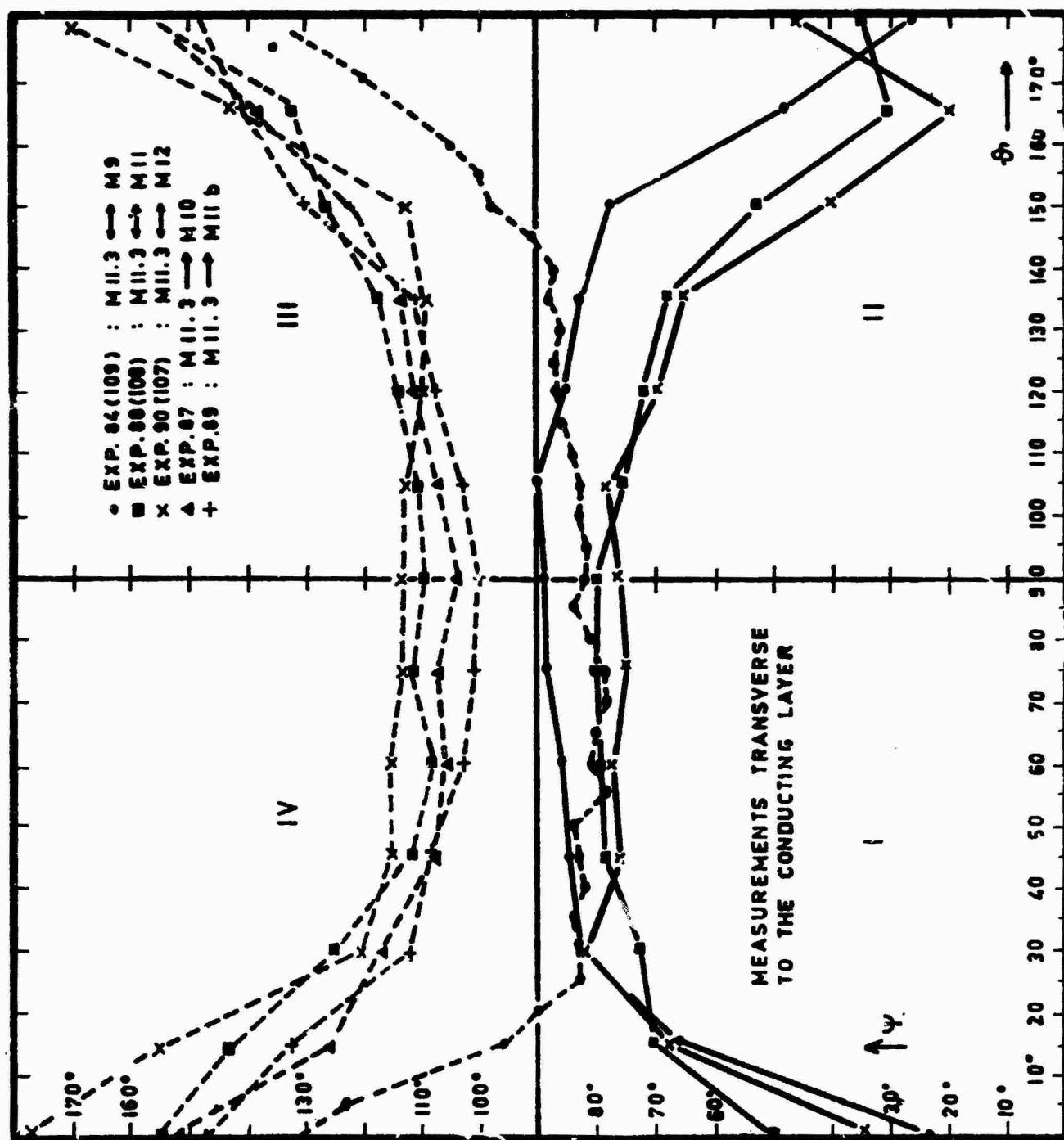0 10 20 30 40 50 METER

FIG. 7.3

FIG. 7.4

The curve of the backward measurement is, as it were, the "image" of the forward measurement curve.

An exact, purely mathematical description of this effect would be extremely difficult, because too many unknown quantities or variables are involved. Certainly, numerous papers were published on this subject but finally calculations are always based on the assumption of quite special facts. The main object of our method, however, was to give at least a qualitative explanation for the "pendulous motion" by means of a clearly arranged geometrical construction using the method of images.
The development of the theory was stimulated by /37, 38, 39, 40/.

7.7 Theory of images

If a quiescent charge is situated in direct neighborhood of a conducting infinite surface a field distribution according to Fig. 7.5a results. This consideration shall app y analogously for moved charges (Fig. 7.5b). The re' cion between the magnetic dipole moment and its age is shown in Fig. 7.5c.

There are two measuring possibilities in the neighborhood of a disturbing zone:

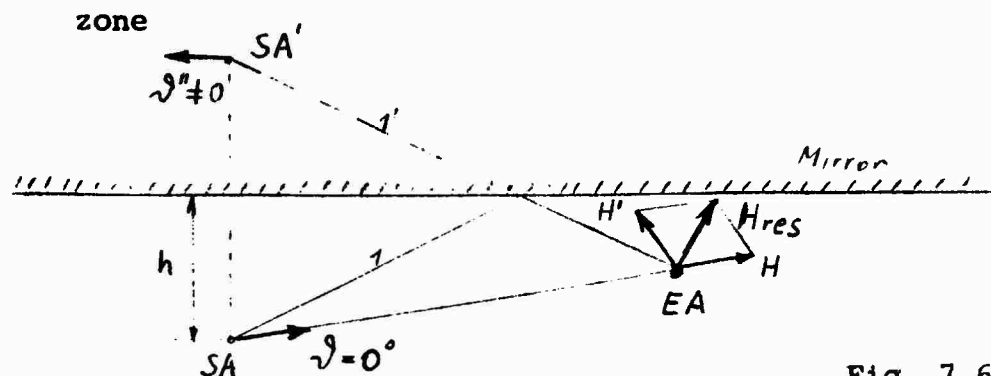Type 1: Measurement approximately parallel to disturbing zone

Fig. 7.6

Let SA' be the mirror image of SA. At EA, two signals
are received superponing one another. The two field
vectors $\vec{H}$ and $\vec{H}'$ generally having different directions
form a resulting vector $\vec{H}_{res}$ with another direction.

Type 2: The conducting zone is situated between trans-
mitting antenna and receiver
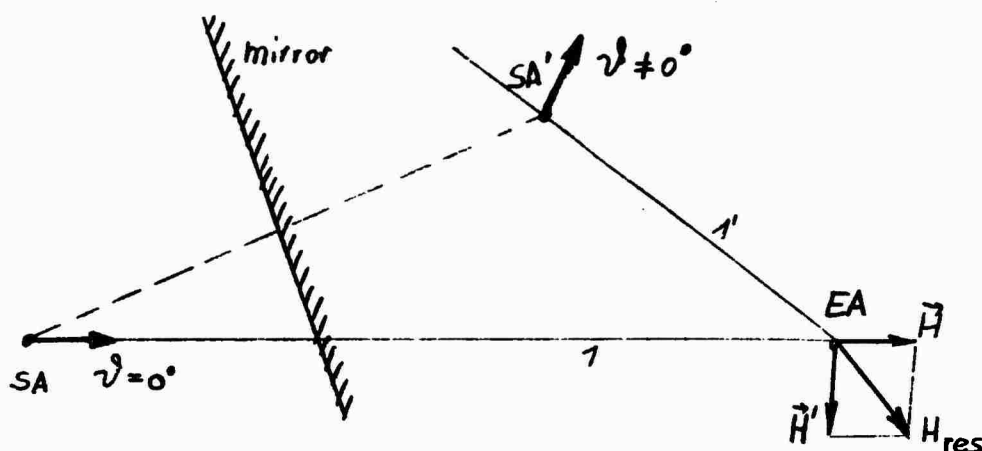
Fig. 7.7

Here, the image SA' develops from the charge distribu-
tion induced by SA in the conducting layer and acting as
an image of SA at SA'. The field strength at EA is again
composed of the signal originating at SA and SA'.

The good agreement between theory and experiment shall be
shown by means of two examples:
Fig. 7.8 is an example for type 1. The measuring distance
is parallel to the disturbance determined in "Morgenschlag".

Fig. 7.9 represents type 2 with the disturbance between
transmitter and receiver.

From the above figures we recognize that the auxiliary
vector $\vec{H}'$ explains rather well the deviating direction
of $\vec{H}_{ex}$.

If, however, $\vec{H}$ and $\vec{H}'$ include an angle of approximately

REFLECTION OF A STATIC CHARGE
a)

REFLECTION OF A ROTATING CHARGE
MIRROR
b)

REFLECTION OF A NORMAL, INCLINED OR PARALLEL DIPOLE MOMENTUM
c)
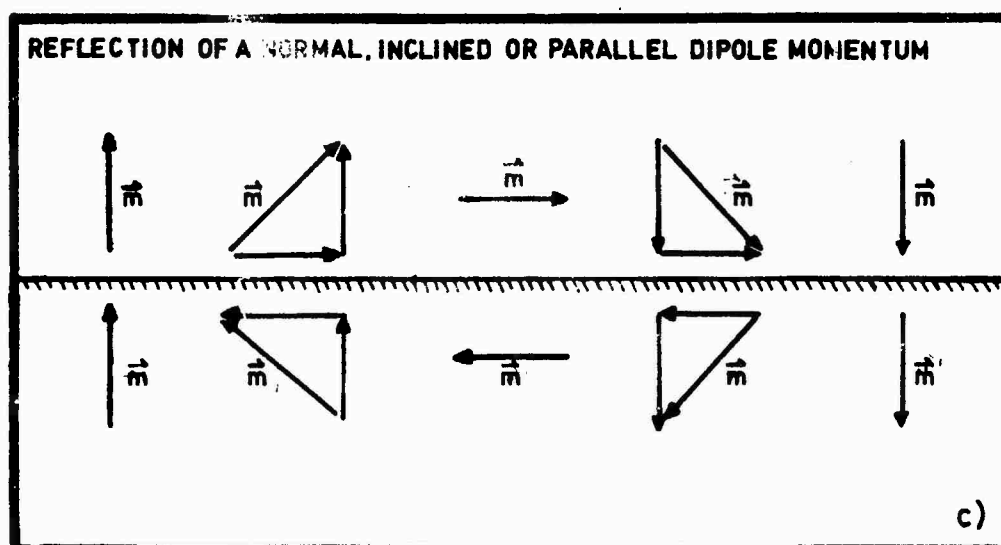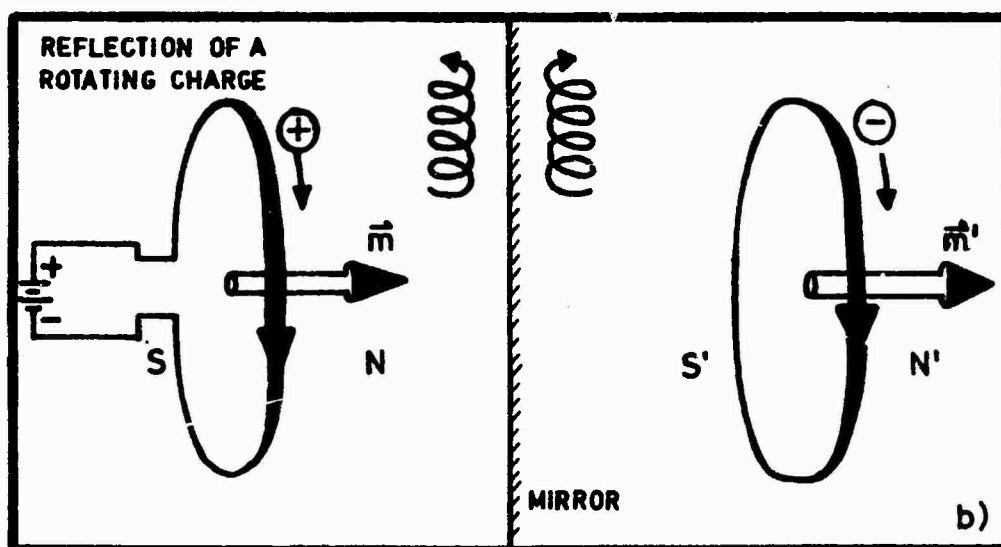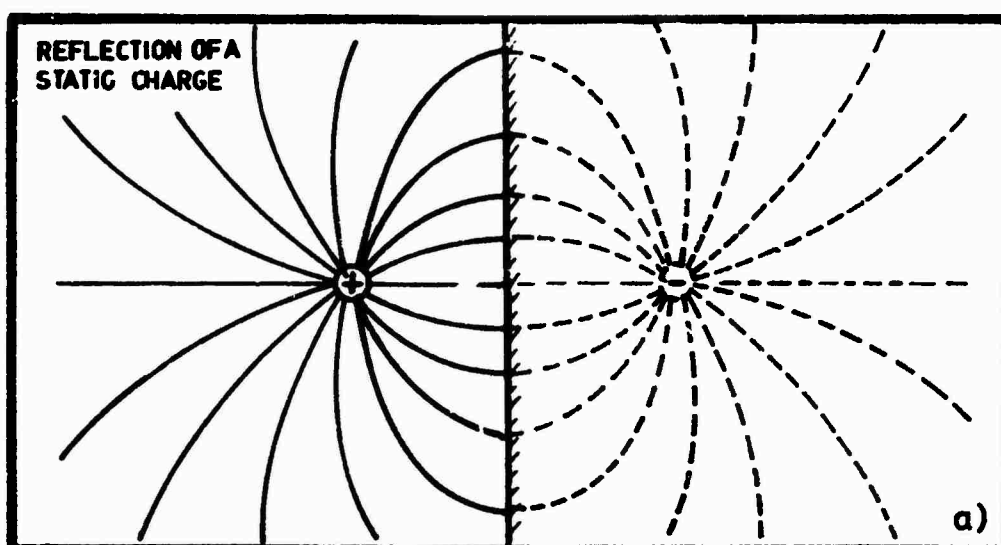
FIG. 7.5

EXP. 106 (M 12 → M8.2)   G = 0.2   χ = 7°
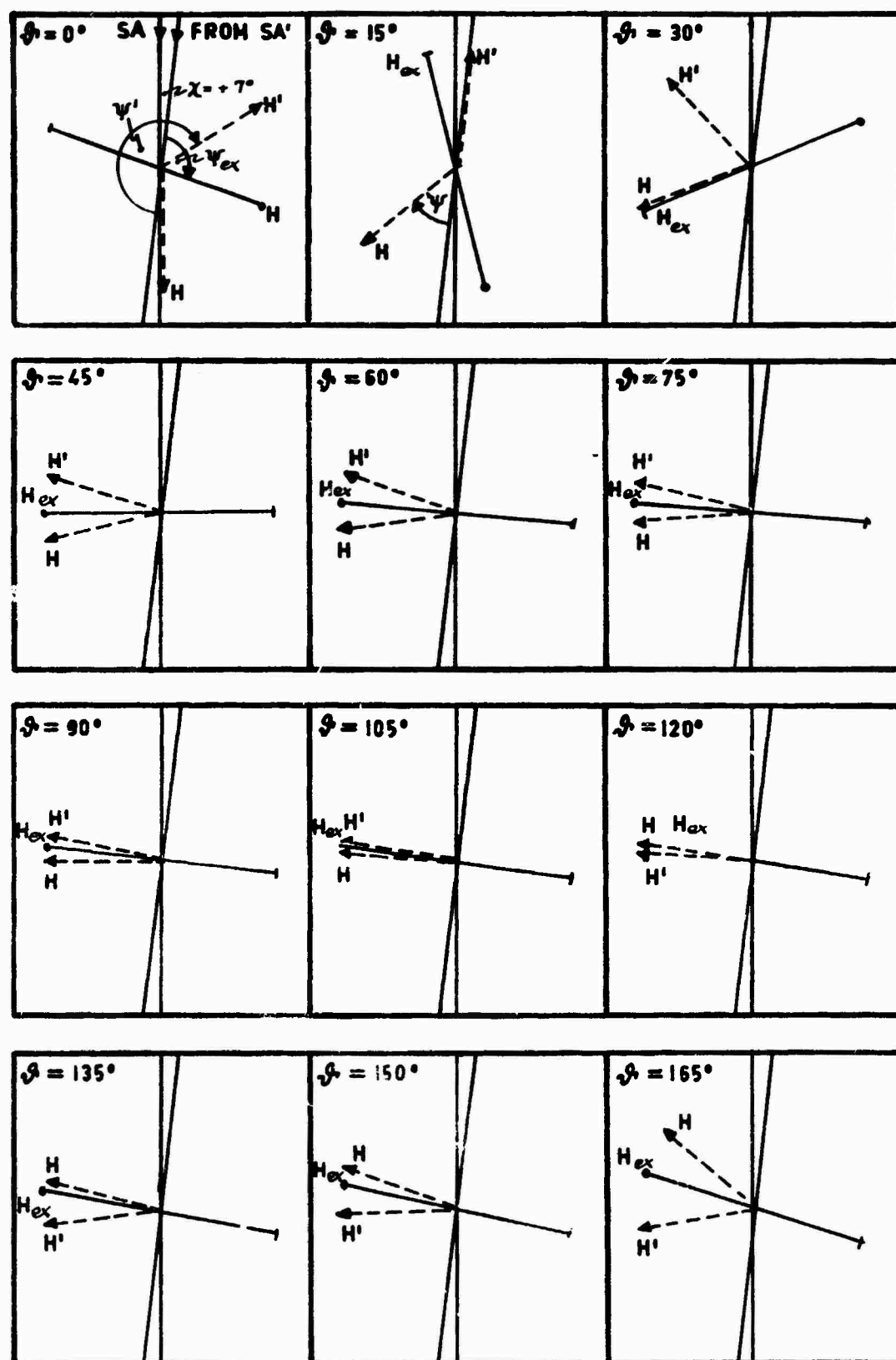
FIG. 7.8

EXP. 88   (M 11.3 → M 11)   G = 0.3   χ = 117°
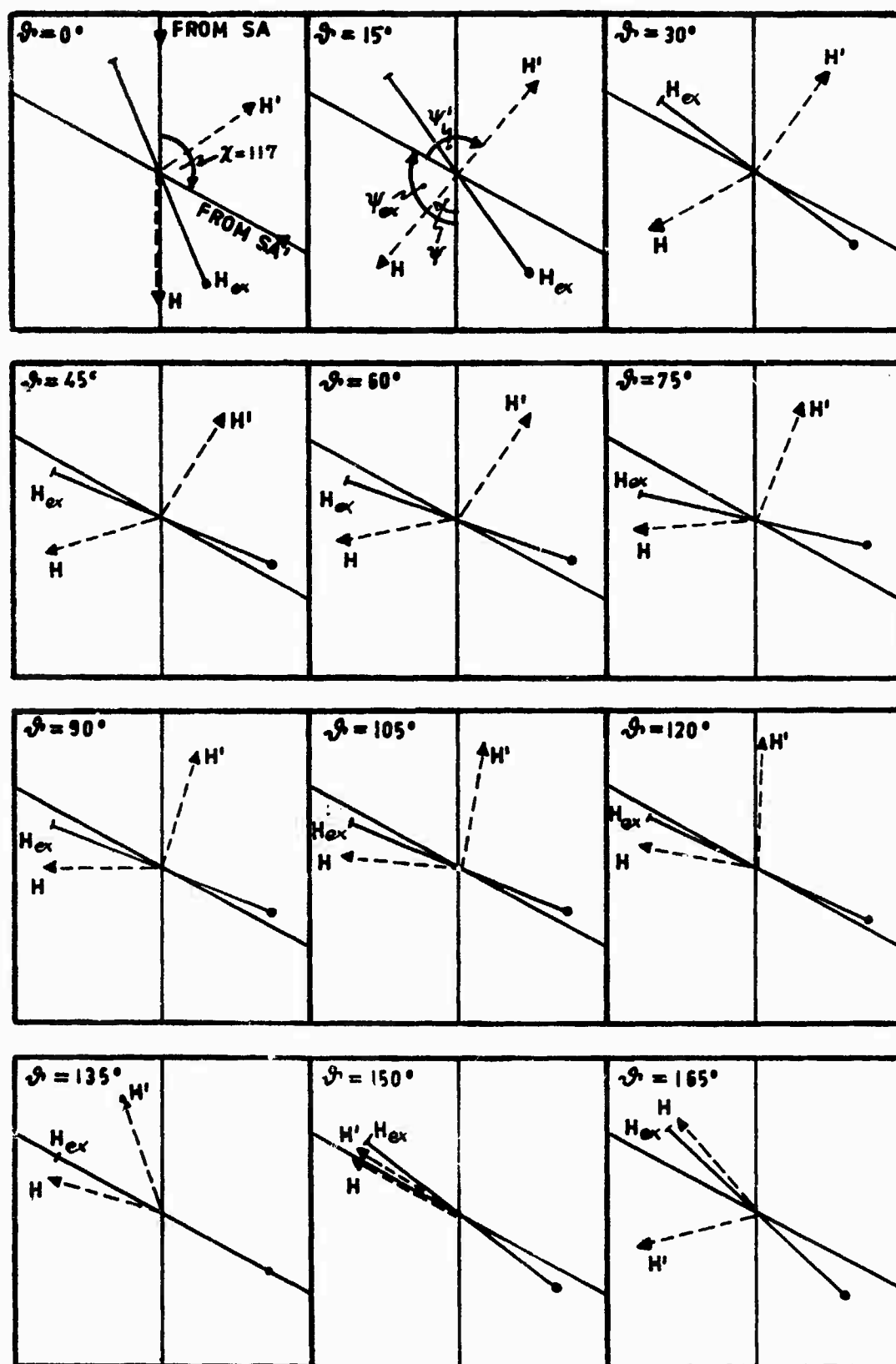
FIG. 7.9

180° some difficulties in interpretation will aris?.
The direction of the resulting vector $\vec{H}_{ex}$ coincides with
$\vec{H}$ or $\vec{H}'$ at type 1 (exp. no. 106), whereas $\vec{H}_{ex}$ is perpendi-
cular to $\vec{H}$ and $\vec{H}'$ at type 2 (exp. no. 88). So we have to
assume that a phase reversal in respect to $\vec{H}'$ (or $\vec{H}$)
occurs at the second case, thereby giving a good explana-
tion for the pendulous motion characterized by the re-
versal of rotation.

The method developed in the mine of St. Gertraudi was
already successfully applied in other mines (Schwaz/Tyrol,
Bleiberg/Carinthia) thereby confirming our theory. A com-
mercial application of this method for ore prospecting,
however, would require further experiments to investigate
the influence of watercourses, rails, and other technical
equipment.

CHAPTER 8

ENTERING MECHANISM OF ELECTROMAGNETIC WAVES
INTO A DISSIPATIVE MEDIUM

8.1 Introduction

In December 1972 the investigations on this subject were
finished. The basic theory which will be briefly referred
to was already published in Final Report 1971 together
with the development of an autorange receiver.

Problem:

Measurements /11/ of the broadcasting transmitter Ö-Re-
gional along a gallery of the mine St. Gertraudi showed
a local period of the maximum magnetic field strength
(major axis of a rotary field ellipse). The transmitter
(629 kHz) is situated at a distance of 30 km from the mine.

Repeated measurements confirmed this unexpected result
which was tried to be explained /30/ by developing a
theory for an electromagnetic wave with oblique inci-
dence on a boundary surface.

8.2 Equations of the magnetic field strength in medium

The equations used by Schumann /30/ are specified in /11/.
For $\vec{H}$ polarized in the direction of the plane of inci-
dence (in air) they take the form

$$E_z(x,y) = E_s e \exp\{j\omega t + f(x,y)\}$$

$$H_x(x,y) = -E_s e \frac{\cos\phi_1}{W_1} \exp\{j\omega t + f(x,y)\} \qquad (8.1)$$

$$H_y(x,y) = -E_s e \frac{\sin\phi_1}{W_1} \exp\{j\omega t + f(x,y)\}$$

for $\vec{H}$ polarized vertically to the plane of incidence
(in air) they read:

$$H_z(x,y) = H_s^e \exp\{j\omega t + f(x,y)\}$$

$$E_x(x,y) = H_s^e \cdot W_1 \cos\phi_1 \exp\{j\omega t + f(x,y)\} \qquad (8.2)$$

$$E_y(x,y) = H_s^e \cdot W_1 \sin\phi_1 \exp\{j\omega t + f(x,y)\}$$

E_s^e ... electric field strength of the incoming wave

H_s^e ... magnetic field strength of the incoming wave

W_1 .... wave resistance in air $= 377\ \Omega$

ϕ_1 .... angle of incidence

ω ..... circular frequency

With the boundary conditions the complex law of Snellius
is obtained

$$\sin\phi_1 = \frac{W_1}{W_2} \sin\phi_2$$

$$W_2 = \rho_{W_2} \exp\left|j^{\alpha/2}\right|$$

$$\rho_{W_2} = \frac{\omega \cdot \sqrt{\mu_2 \epsilon_2}}{c_0 \sqrt{\sigma^2 + \omega^2 \epsilon_0^2 \epsilon^2}} \sqrt[4]{1 + \left(\frac{\sigma}{\omega \epsilon_0 \epsilon_2}\right)^2} \qquad (8.3)$$

$$\alpha = \arctan\frac{\sigma}{\omega \epsilon_0 \epsilon_2}$$

W_2 .... wave resistance in medium (rock)

ϵ_2 .... dielectric constant in medium

ϵ_0 .... absolute dielectric constant

μ_2 .... permeability in medium (rock)

σ .... conductivity in medium (rock)

c_0 .... vacuum light velocity

From the boundary conditions we can conclude the complex transmission coefficients for the case of parallel polarization $(1 + \Gamma_p)$ and vertical polarization $(1 + \Gamma_v)$, respectively

$$1 + \Gamma_p = \frac{2 \cos\phi_1}{\cos\phi_1 + W_1 \sqrt{\dfrac{1}{W_2^2} - \dfrac{1}{W_1^2} \sin^2\phi_1}}$$

$$1 + \Gamma_v = \frac{\left(\dfrac{W_1}{W_2}\right)^2 \cos\phi_1 - \sqrt{\left(\dfrac{W_1}{W_2}\right)^2 - \sin^2\phi_1}}{\left(\dfrac{W_1}{W_2}\right)^2 \cos\phi_1 + \sqrt{\left(\dfrac{W_1}{W_2}\right)^2 - \sin^2\phi_1}} \qquad (8.4)$$

The equations can be simplified to

$$1 + \Gamma_p = \rho_{1+\Gamma_p} e^{j\zeta_p}$$

$$1 + \Gamma_v = \rho_{1+\Gamma_v} e^{j\zeta_v} \qquad (8.5)$$

After laborious calculations the following equations for the magnetic field strength are obtained

$$H_x^d = \rho_{1+\Gamma_p} \sqrt{\rho} \cdot W_1 \cdot H_p^0 \cdot e^\psi \cdot \exp\{j | \omega t + \pi + (\theta_p - \xi/2 |\}$$

$$H_y^d = \rho_{1+\Gamma_p} \cdot \sin\phi_1 \cdot H_p^0 \cdot e^\psi \exp\{j | \omega t + \pi + \theta_p |\} \qquad (8.6)$$

$$H_z^d = \rho_{1+\Gamma_v} \cdot H_v^0 \cdot e^\psi \cdot \exp\{j | \omega t + \zeta_p - \zeta_p + \zeta_v - \Omega |\}$$

$\rho_{1+\Gamma_p}$ ... amount of the transmission coefficient of the electric field strength with $\vec{H}$ polarized parallel to the plane of incidence

$\rho_{1+\Gamma_V}$ ... amount of the transmission coefficient of the magnetic field strength with $\vec{H}$ polarized vertically to the plane of incidence

$\psi=\psi(x,y)$ attenuation factor

$\theta_p=-\vec{k}\,\vec{x}$ .. position function of the phase

$\vec{k}$ .... vector of wave number

H_p^O, H_s^O ... amplitudes of the magnetic field strength of the incoming elliptically polarized wave

ζ_p, ζ_s ... phases of the complex transmission coefficients

Ω .... phase shift of the incoming elliptically polarized field

Furthermore,

$$\sqrt{\rho} \sim \frac{1}{\rho_{W_2}}$$

$$\xi \sim -\alpha \tag{A}$$

is valid with high accuracy (error less than 1 %).

In the following paragraph the reasons leading to a local periodicity are dealt with.

8.3 Reasons for the local periodicity

Assumption:

The rock is no longer assumed to be homogeneous but bearing a reflecting layer which is shown in Fig. 3a. By superposition of the incoming and the reflected wave a local periodicity is generated. Further calculations show the possibility of determining the angle between reflected layer and gallery axis from the three occurring modes:

a) $\vec{k}_r$ in the first quadrant of the complex period only in z'-direction. Since $k_{x',r}$ has the same direction as $k_{x'}$ no periodicity can occur in x'-direction.

b) $\vec{k}_r$ in the second quadrant

x'- and z'-periodicity. $k_{x',r}$ and $k_{z',r}$ are anti-parallel to $k_{x'}$ and $k_{z'}$.

c) $\vec{k}_r$ in the third quadrant

period only in x'-direction. $k_{x',r}$ antiparallel to $k_{x'}$, $k_{z',r}$ parallel to $k_{z'}$.

(The dashed quantities relate to the coordinate system determined by the gallery system.)

Fig. 3b shows the possible modes.

The following relations between the angles can be read from Fig. 3a:

a) $\quad 0 < \kappa = \dfrac{\pi}{2} + 2\gamma - \theta < \dfrac{\pi}{2}$

b) $\quad 0 < \kappa = \dfrac{\pi}{2} + \theta - 2\gamma < \dfrac{\pi}{2}$ $\qquad$ (8.7)

c) $\quad 0 < \kappa = 2\gamma - (\theta + \dfrac{\pi}{2}) < \dfrac{\pi}{2}$

8.4 Determination of γ

From

$$\theta_p = -\vec{k}\vec{x}$$

$k_{x'}$ and $k_{z'}$ can be obtained.

$$k_{x'} = \frac{1}{377} \mu\mu_0\omega \sqrt{1 - \frac{\cos^2\phi_1}{\sin^2\tau}} \qquad (8.8)$$

$$k_{z'} = \frac{1}{377} \mu\mu_0\omega\cos\phi_1 \frac{\cos^2\tau}{\sin\tau} + \sin\tau \frac{\omega\sqrt{\varepsilon\mu}}{c_0\sqrt{2}} \sqrt{1 + \sqrt{1 + \left(\frac{\sigma}{\omega\varepsilon_0\varepsilon}\right)^2}}$$

$$(8.9)$$

τ .... slope angle $\qquad\qquad$ σ ... rock conductivity

ϕ_1 ... angle of incidence $\qquad$ ε ... dielectric constant of
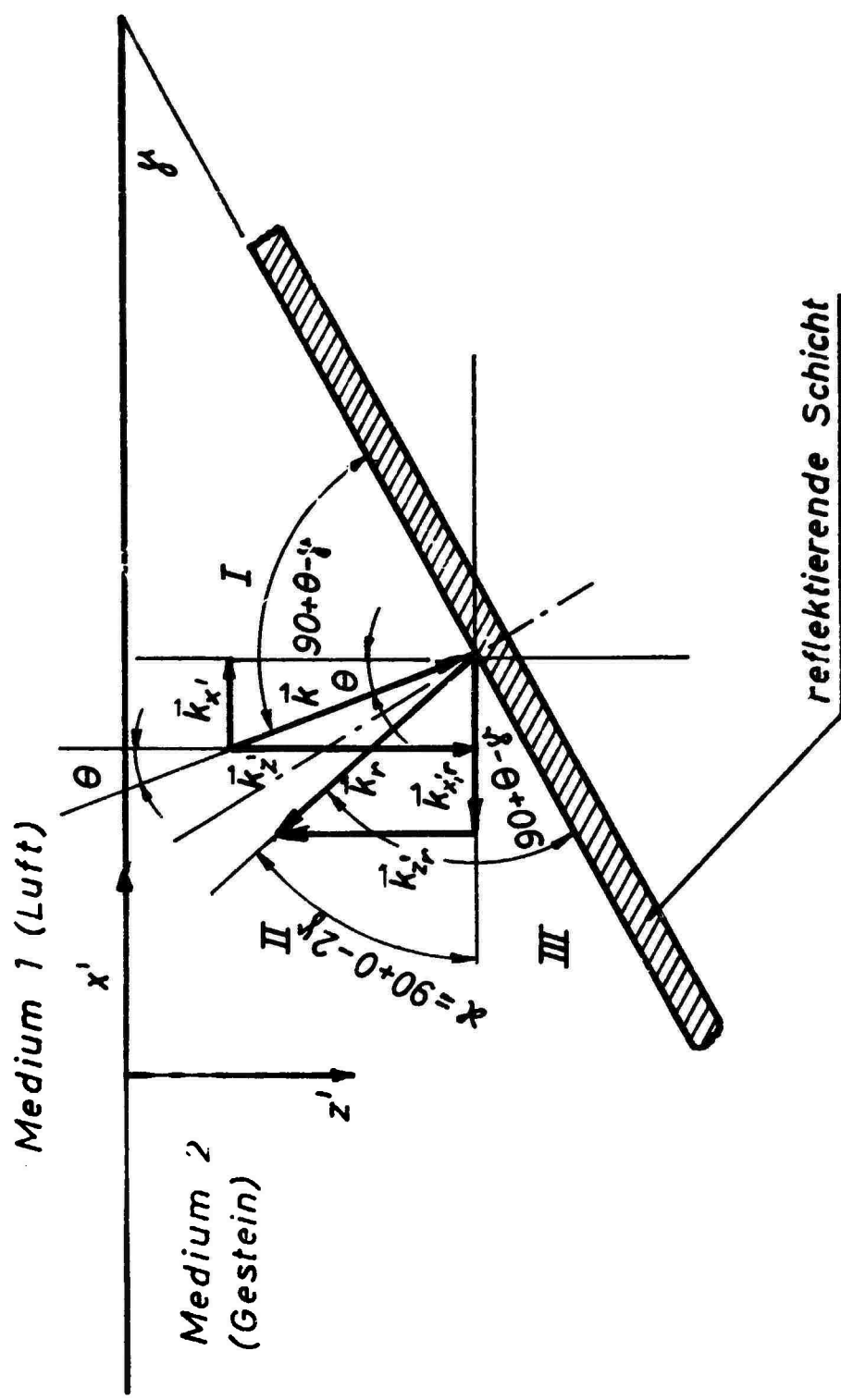$\qquad\qquad\qquad\qquad\qquad\qquad\qquad\qquad\qquad$ the rock

Fig. 3a

Wellentypen, die bei Anwesenheit einer
reflektierenden Schicht im Medium 2
dort auftreten können

Fall III

Fall I

Fall II
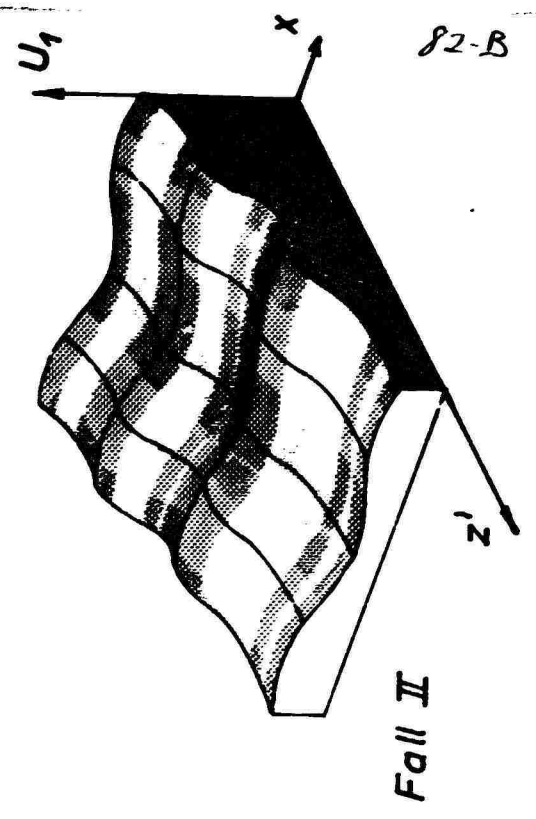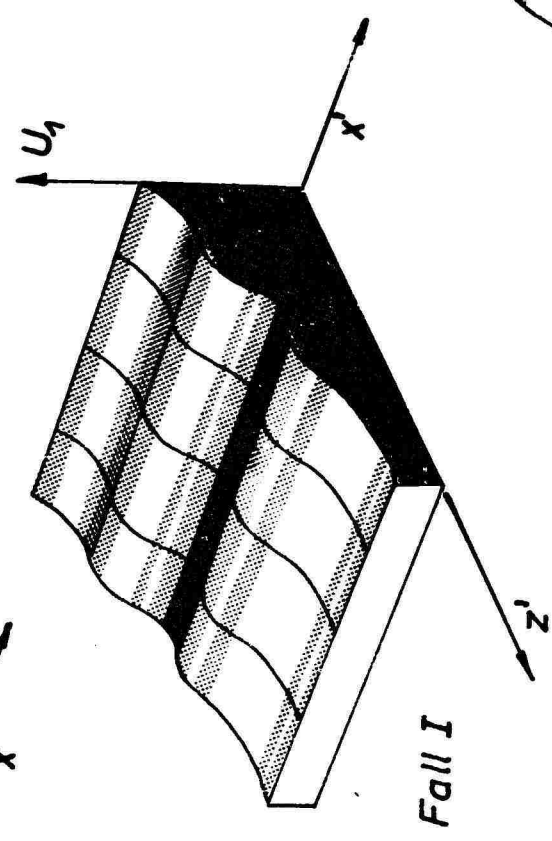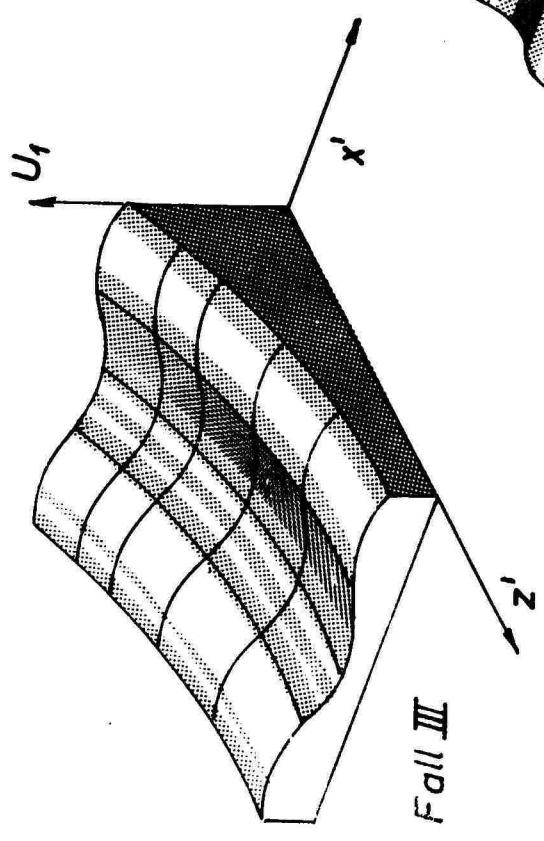
Fig.3b

From

$$k_{x',r} = |k| \cos \kappa$$

$$k_{z',r} = |k| \sin \kappa$$

(8.10)

and

$$|k| = \sqrt{k_x{}^2 + k_{z'}{}^2}$$

we can calculate both the period in x'-direction

$$P_{x'} = \frac{2\pi}{k_{x'} + k_{x',r}}$$

(8.11)

and the period in z'-direction

$$P_{z'} = \frac{2\pi}{k_{z'} + k_{z',r}}$$

(8.12)

Thus, it is possible to determine $k_{x',r}$ and $k_{z',r}$ from the rock parameters, and the period κ can be determined by means of Eq. (8.10) and finally γ is calculated from Eq. (8.7) if the mode is known.

Measurements showed a periodicity in z' thus proving the occurrence of case b).

For $\epsilon = 10$, $\sigma = 10^{-3}$ S/mm, $f = 629$ kHz and $\phi_1 \sim 84^{\circ}$

$$\gamma = 36,7^{\circ}$$

The above described method fails if wavelength and dimension of the reflecting surface are in the same order of magnitude. This fact could be proved by experiments at low frequencies (278 kHz). Eqs. (8.8) and (8.9) show that $k_{x'}$ and $k_{z'}$ are proportional to ω, the periods $P_{x'}$ and $P_{z'}$ being inversely proportional to ω.

Fig. 4b is a schematical representation of the surroundings of the measuring site in the mine of Grosskogel.

Theory says that for plane waves the x- and u-waves are not attenuated, whereas the y- and v-waves are. Influencing the test results by the v-wave is impossible on account of the large distance.

8.5 Transmission coefficients

The amounts of the transmission coefficients were computed for different values of σ and represented in dependence on ϕ_i in the diagrams 4c and 4d.

$(\rho_{1+\Gamma_p})_{el}$ always remains <1, whereas $(\rho_{1+\Gamma_v})_{mag}$ can grow much larger than 1.
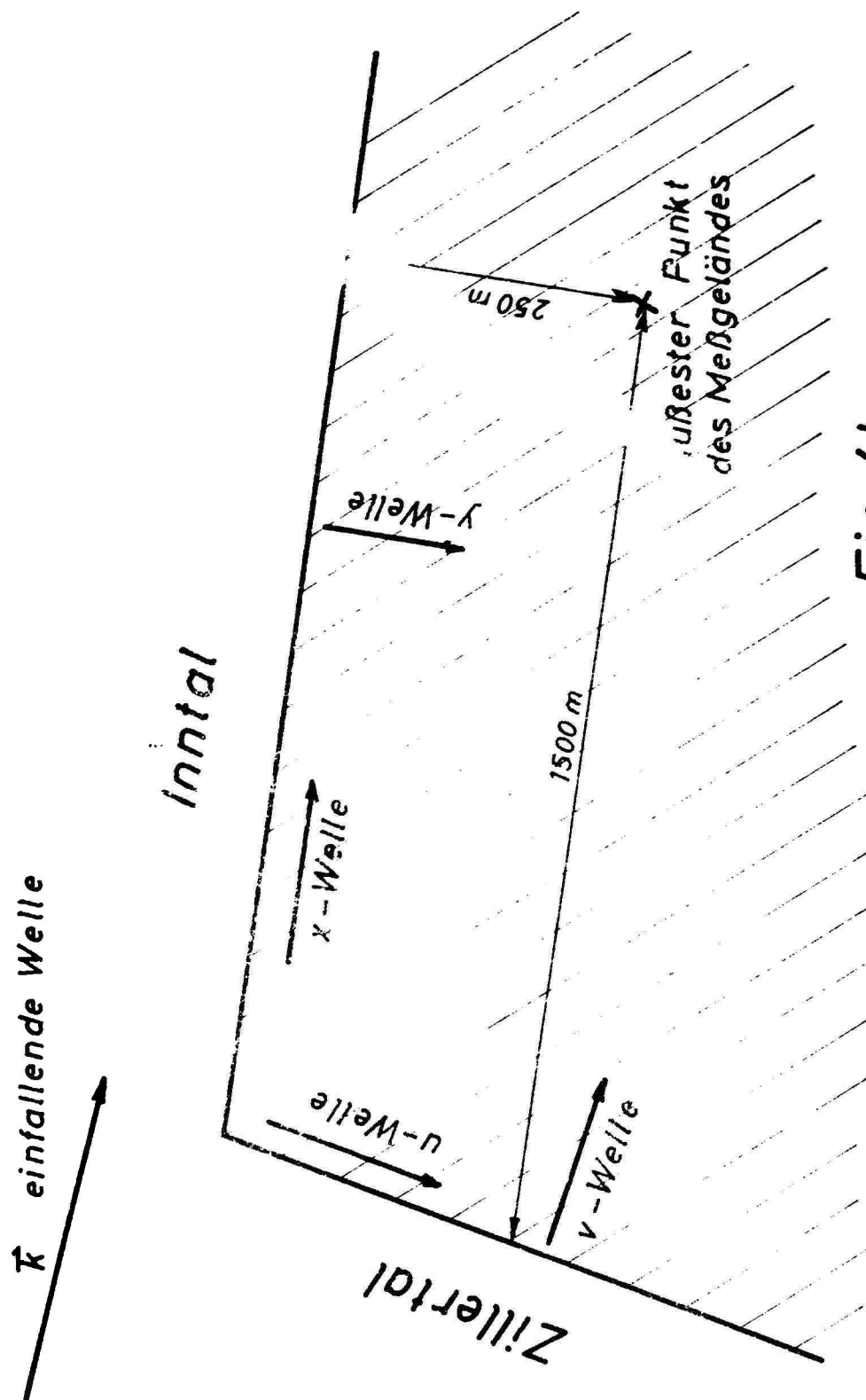
The present calculations, however, are not contradictory to the law of energy preservation, since the transmission coefficient of the pointing vector $\vec{S}$ is smaller than 1 in any case as is shown in Fig. 4e.

A possible explanation can be: The electric field in the dissipative medium is immediately transformed to an eddy current field. Thus, a transformation of electric into magnetic energy occurs. This is in good agreement with the unexpectedly high measuring values in winter.

On the one hand, the boundary surfaces are covered by a well conducting snow layer, on the other hand, the attenuation factor diminishes on account of the decreased humidity in winter.

8.6 The pointing vector $\vec{S}$

$\vec{S}$ was investigated for $\vec{H}$ polarized parallel to the plane of incidence and was found to be by no means stationary any more. The top of the vector $\vec{S}$ is following an ellipse being situated in the plane of incidence.

Fig.4b

Fig. 4c

Betrag des Transmissionskoeffizienten der elektrischen Feldstärke

Fig. 4d

Fig. 4e
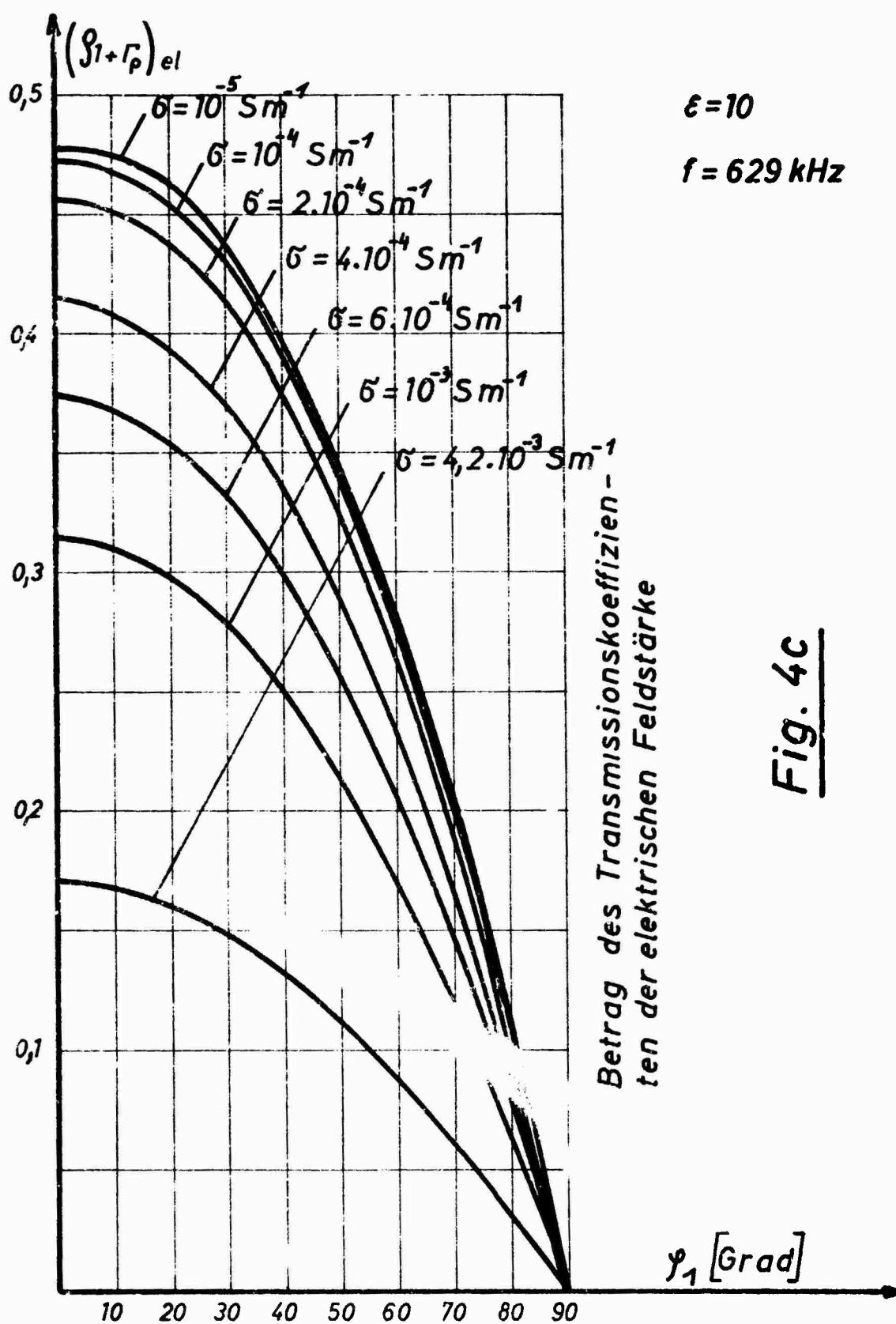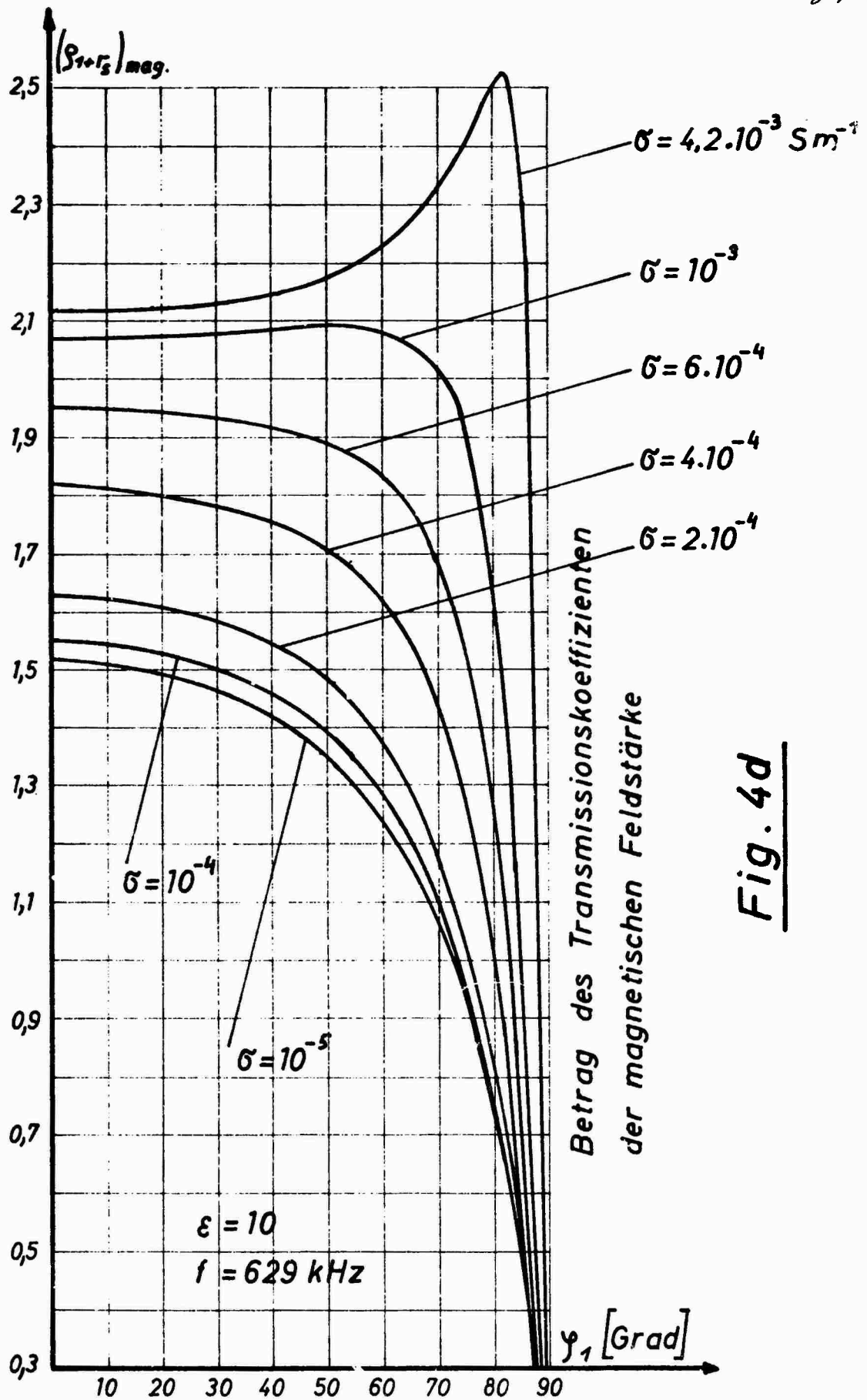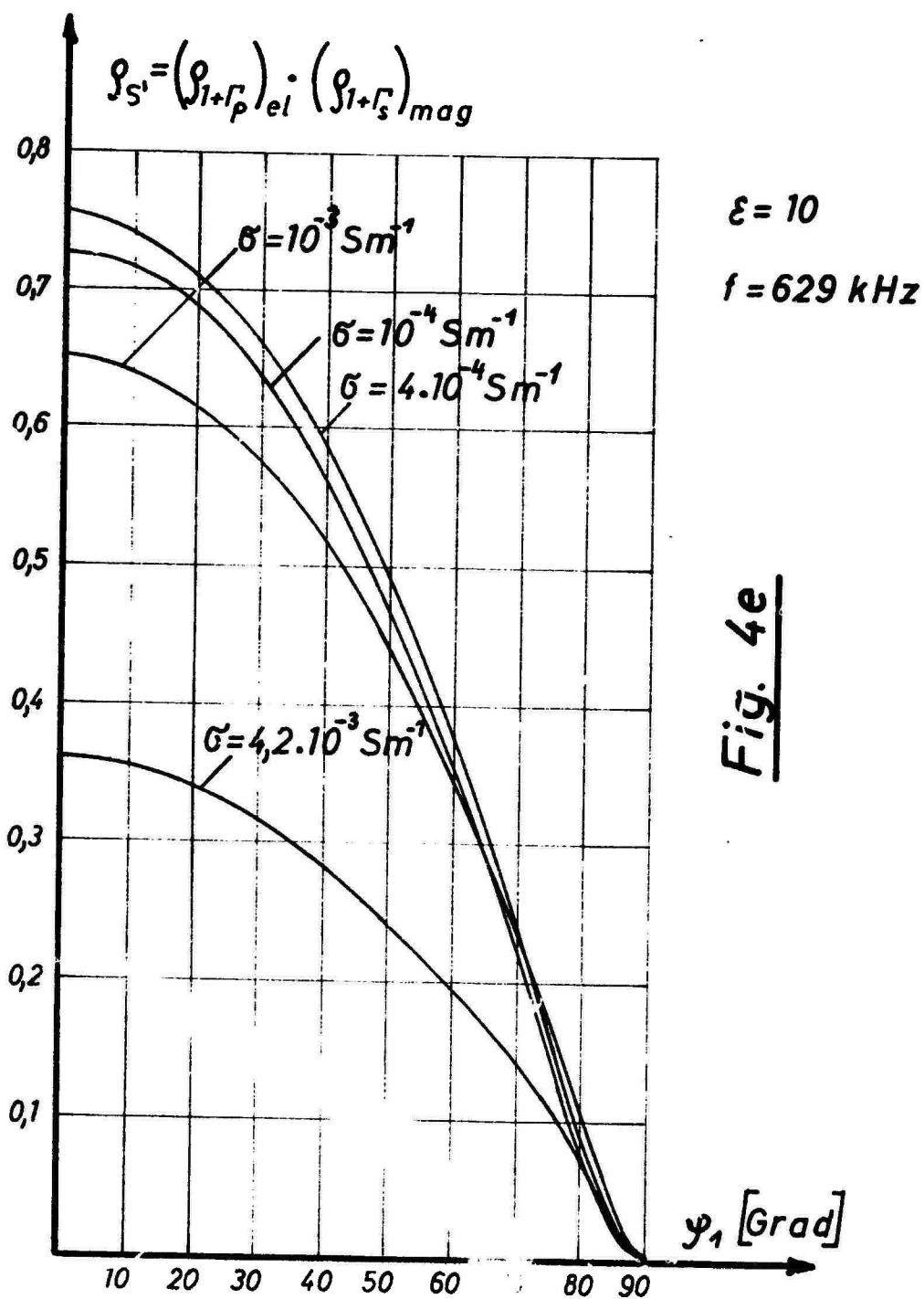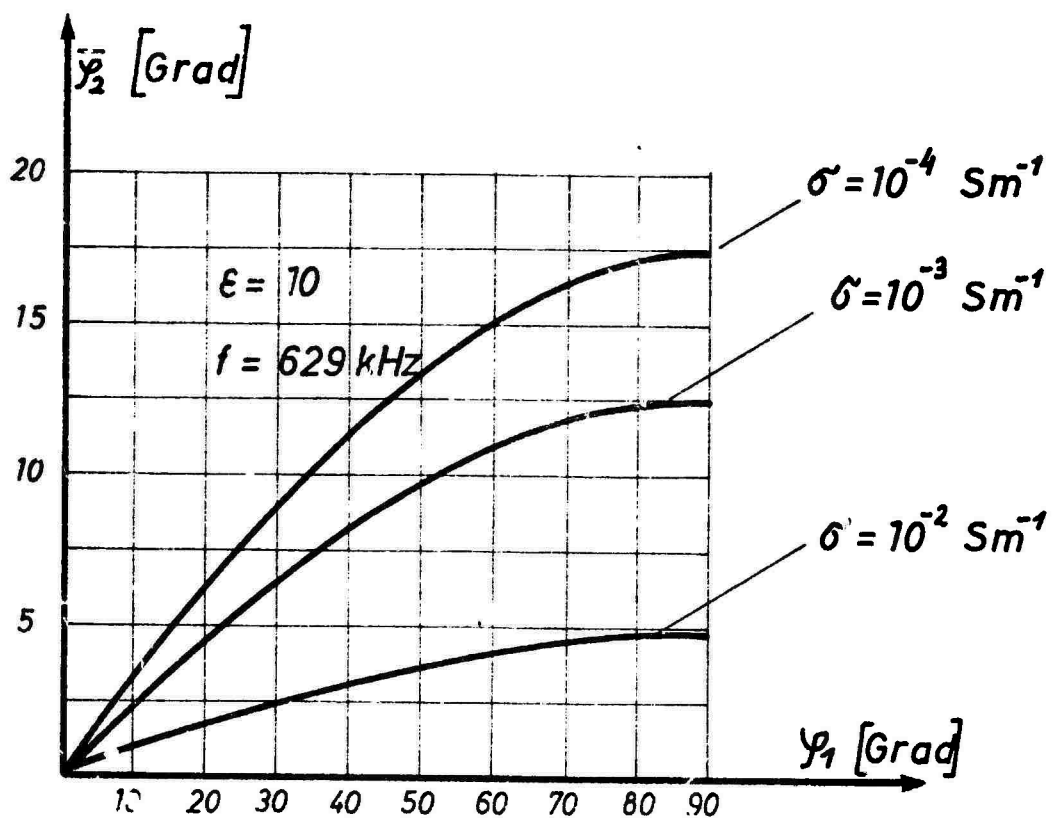
Richtung, die $\overline{Re\,\vec{S}}^{\,t}$ zum Einfallslot einnimmt

Fig. 4g

For the general case of an elliptically polarized wave
$\vec{S}$ is describing an oblique elliptical cone in the
dissipative medium. S is complex; the mean time values
of $\overline{ReS}^t$ and $\overline{ImS}^t$ were calculated

$$\overline{ReS}^t = \overline{ImS}^t$$

So only half of the total energy is measurable.

Finally, the direction of $\overline{ReS}^t$ in respect to the vertical
incidence was examined and represented in Fig. 4g for
different σ in dependence on ϕ_1.

CHAPTER 9

ABOVE-GROUND AND SUBSURFACE LONG-TIME
REGISTRATION OF VLF TRANSMITTERS

Based on some preparatory experiments of W. GRADL per-
formed in 1965, the wellknown British VLF transmitters
GBR at 16.0 kHz and GBZ at 19.6 kHz were registered.
The main purpose of this registration is to determine
whether or not a surface wave of measurable amplitude
is existing. Subsurface measurements shall make it
possible to eliminate above-ground atmospherics.

To measure the GBR and GBZ signals a tube-operated se-
lective levelmeter with a total band width of 80 Hz,
which is just including the frequency jump of 50 Hz at
frequency modulation was used. The simple rectification
used at the beginning proved to be insufficient because
the noise amplitudes amounted to a multiple of the ef-
fective amplitudes at times of greater atmospherics
(thunderstorms). Only a special decoder in two stages
with time constants of 0.1 and 10 sec allowed an un-
disturbed reception of signals.

The long integration time constant has the disadvantage
of delivering a distorted pattern if the signal is
amplitude-keyed, the distortion being due to the time
intervals (in the order of seconds). There are always
2 hours of information followed by 1 hour of outage
which showed up to be a negligible loss of information.

Since the tube-operated receiver did not maintain the
adjusted receiving frequency with sufficient accuracy
for a period of several days (owing to unevitable tempe-

rature fluctuations) a varicap was added to the oscilla-
tor thus providing the possibility of wobbling a certain
frequency band externally. Fig. 9.1 shows the block
diagram of the complete equipment.

Long ferrite rod antennas which were optimized ade-
quately have proved successful /9, 31, 32/. The essential
piece of the equipment is the selective levelmeter with
an input sensitivity of -11 neper corresponding to
about 10 µV. The saw-tooth voltage of a Wavetek 142
with 10 min time constant was used as sweep control.
The output signal of the levelmeter was amplified by
14 dB to max. 4 V by a PM 5175 (Philips) to keep down
the error influence of the threshold voltage of the
decoding diodes. The decoded signal is registered on a
line recorder and constitutes a spectral distribution
of the VLF signals in the requested frequency range.
Fig. 9.2 shows a part of such a registration tape.

One measuring point per transmitter for every 10 minutes
proved just sufficient, an increase in wobbling fre-
quency would have caused a decrease of the registered
maximum amplitudes on account of the integration time
constant.

The signals of all receivable VLF transmitters in the
world within the frequency range of 14.5 to 20.5 kHz
were received above and below the earth surface. The
object was to find out whether over a propagation di-
stance of 1300 km, several 100 m below the surface, the
sky waves, i.e. the signal, that is reflected by the
ionosphere, form the main part of the received signal
or if the surface waves represent a considerable amount
of signal or the signal at all.

For this purpose the course of the signal amplitude of
the GBR transmitter (16.0 kHz) was plotted in the same

scale during 24 hours from both a measurement below
and above the earth surface (Fig. 9.3). The two curves
were measured on two different days, because only one
reception apparatus was available. A determination of
a mean value of amplitudes over a period of several
days was impossible, since this would have blurred the
characteristic sudden increase of amplitude at sunrise.
The two curves may be regarded as standing for a number
of curves plotted under the same conditions. From the
curves it is obvious that the wave in soil (curve 2)
is certainly the sky wave, because the attenuation
measured at the very constant amplitude during daytime
corresponds exactly to the precalculated attenuation
of the sky wave. Furthermore, the course of amplitude
at sunrise and sunset characteristic for the sky wave
can be determined equally above and below the surface.
If the fluctuating night course of several measuring
series below and above the surface is averaged, the
same amplitude ratio as during daytime can be calcu-
lated. If there were a signal portion of significant
magnitude that is independent on the ionosphere, the
amplitude ratio would change on account of the different
attenuation for surface and sky waves. Thus, it is evident
that the ionosphere has a significant influence on the
diurnal course of amplitude even at subsurface reception.

The dashed parts of the curve in Fig. 9.3 are estimated
values corresponding to the AM-periods of the transmitter.
This characteristic course could be observed during all
the time of registration (several months) in practically
the same way. It must be mentioned that at night the
amplitude is considerably smaller than at daytime.

Plotting the GBZ transmitter at 19.6 kHz with the same
location brought about quite different results (Fig. 9.4).

REGISTRIERANLAGE
Blockschaltbild

Fig. 9.1

GBZ 19,6 kHz
GOD 19,0 kHz
NAA
GBR 16,0 kHz FUB

Fig.: 9.2

Fig.9.3

88·c

Fig. 9.4

88-b

Nachtamplitude

ober Tag

Sonnenaufgang

GBZ 19,6kHz

GBR 16,0 kHz

HF-Amplitude (normiert)

Uhrzeit →

unterirdisch

Sonnenaufgang

GBZ 19,6kHz

GBR 16,0kHz

HF-Amplitude (normiert)

Uhrzeit →
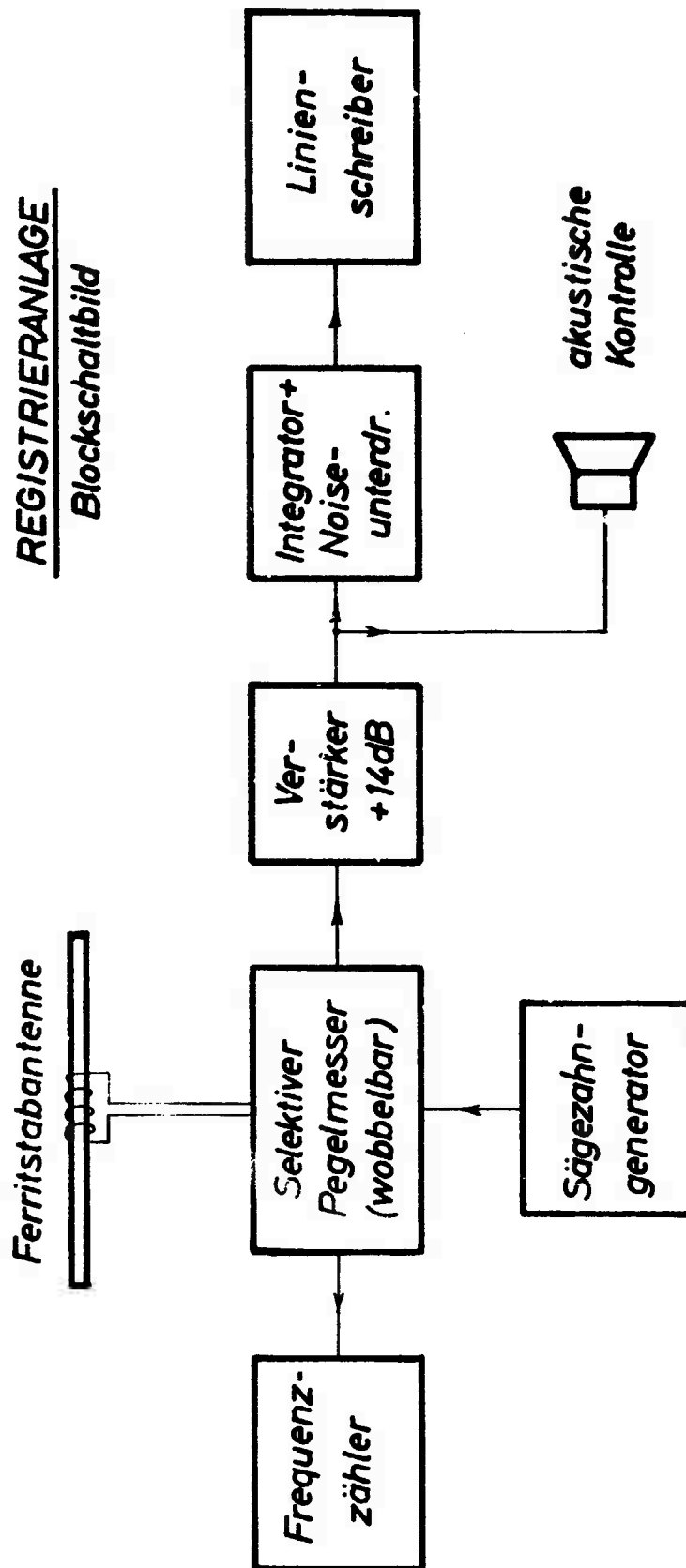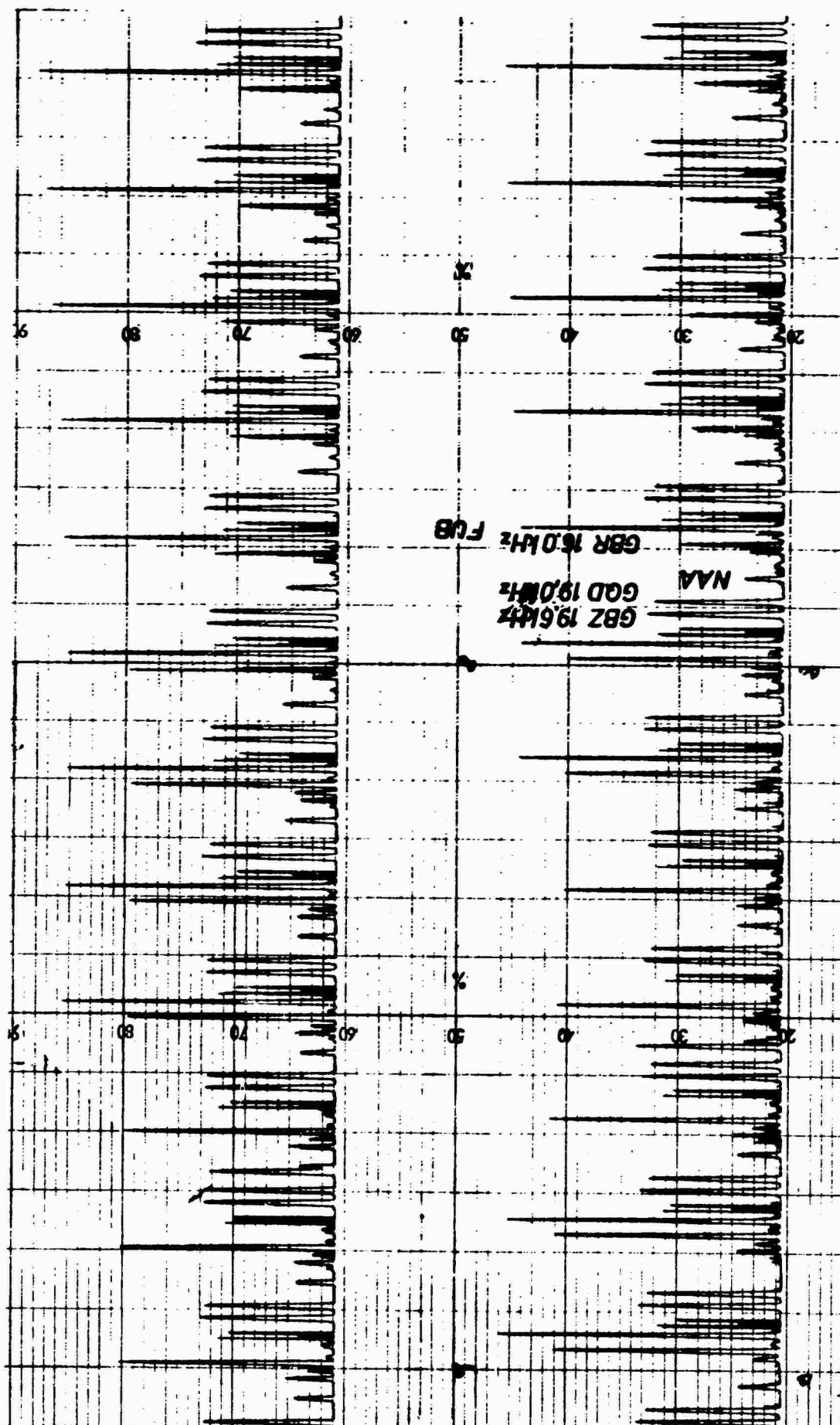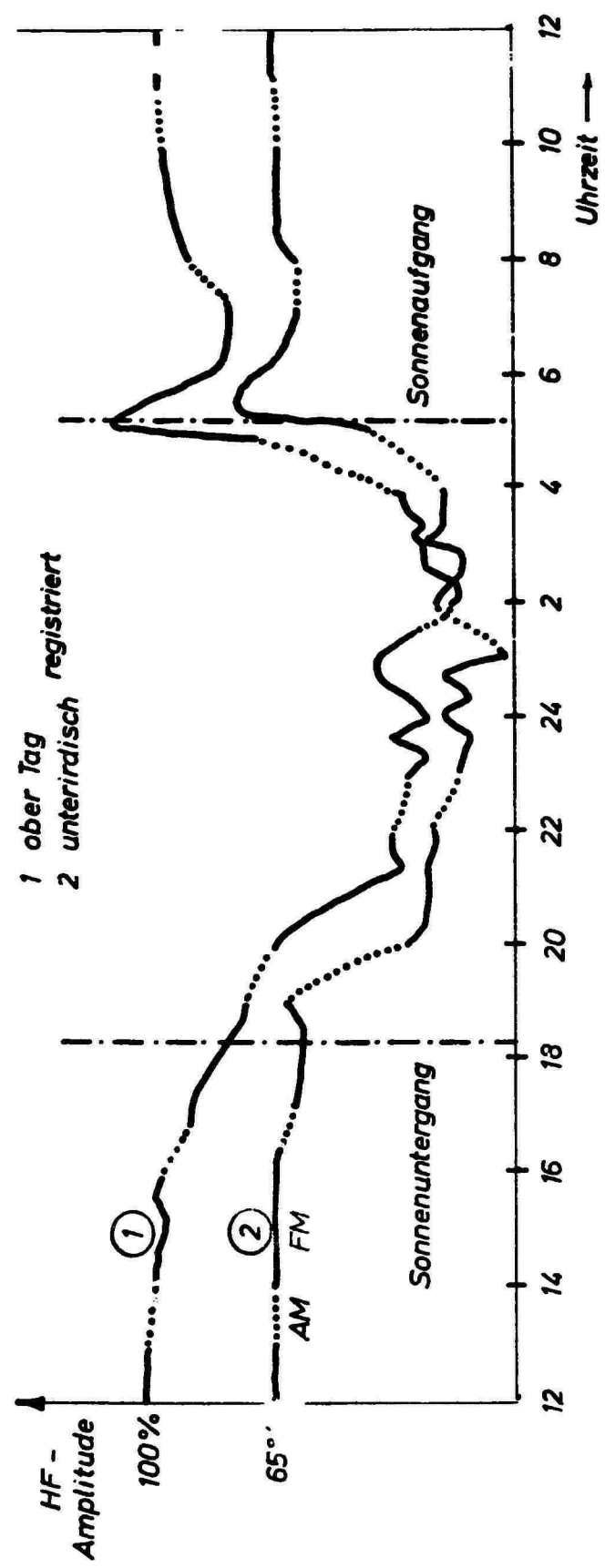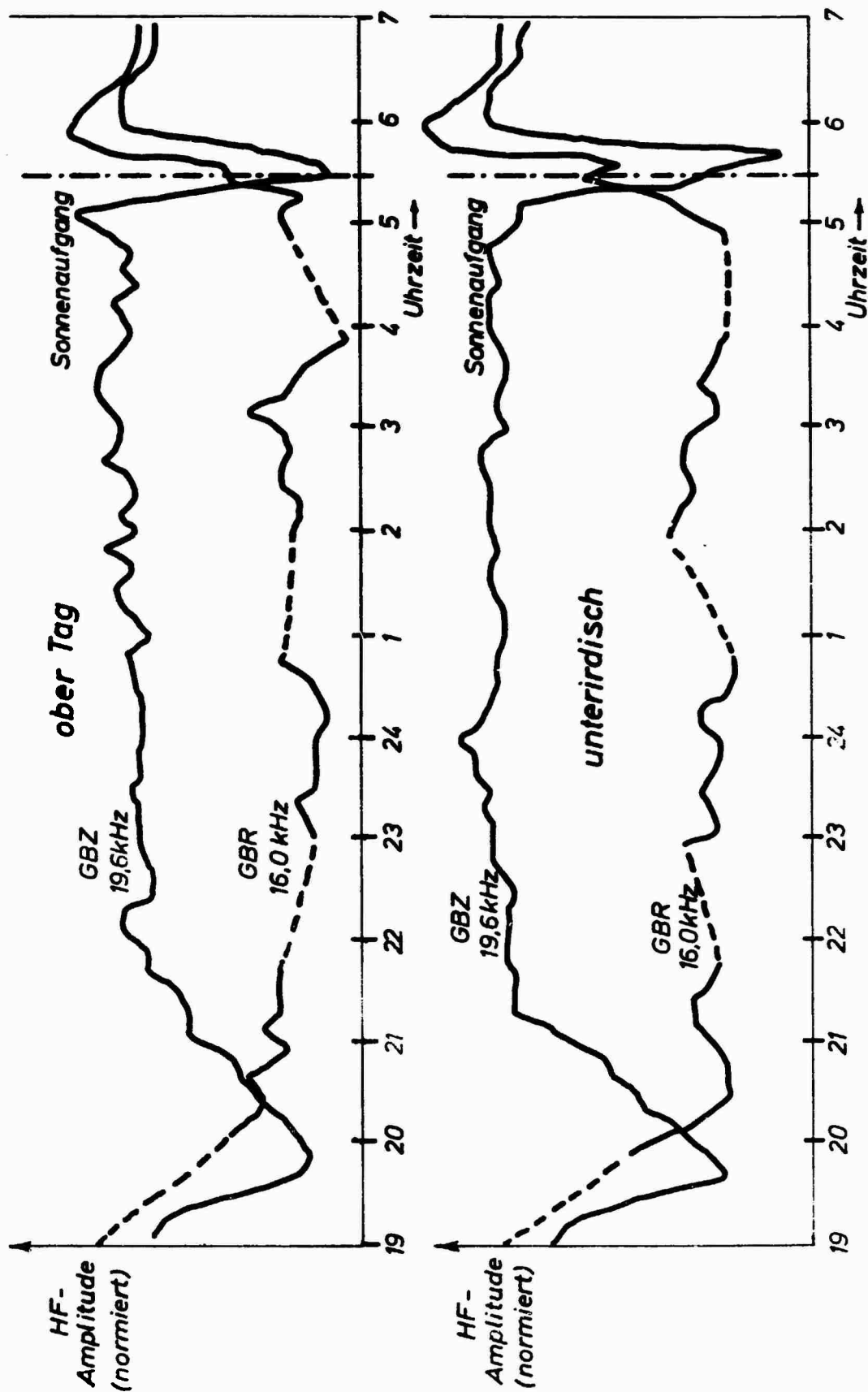
In Fig. 9.4 the night course between 7 p.m. and 7 a.m. is plotted. The diurnal course of the two transmitters is approximately identical (GBZ amplitude is by about 20 % smaller than GBR amplitude) whereas the GBZ night amplitude comes up to the value of the day amplitude. In some nights the day values were even exceeded.

The upper diagram of Fig. 9.4 shows the characteristic conditions of the above-ground registration, the diagram below shows the interpretation of a subsurface registration.

Since there was only one device available to plot all these diagrams an exact coincidence of the reception characteristics is impossible. Two comparable diagrams had to be measured on two different days.
To eliminate accidental fluctuations, a greater number of above-ground and subsurface diagrams was interpreted always showing this distinct difference between the two neighboring frequencies of 16 and 19.6 kHz. It is principally possible to take an average of the different similar diagrams and would equalize the slight fluctuations of the night course, but the characteristic sunrise peaks would also be blurred.

For a further examination of these effects it is absolutely necessary to register the signal amplitudes above and below the earth surface simultaneously. Two battery-operated registration devices are already under construction, using a magnetic tape instead of the line recorder as a data carrier. Thereby it will be possible to show up clearly one of the expected advantages of a subsurface registration, namely the fact, that artificial or man-made noise peaks are more heavily attenuated than the measuring signal penetrating from outside. This effect was partly determined with the simple equipment

already and is due to the fact that the signal of the
two transmitters arrives as a farfield at the point of
reception whereas the especially disturbing noise peaks
from the near neighborhood arrive as a nearfield with
a multiple of the measuring amplitude. This is explained
by the following two diagrams (Figs. 9.5 and 9.6).
Fig. 9.5 shows an above-ground registration during a
local thunderstorm; it can be seen that instead of the
zero line there is a beam of numerous noise peaks which
come through very distinctly in spite of the efficient
noise inverter.
Fig. 9.6 represents the equivalent subsurface registra-
tion showing an absolutely undisturbed diagram when
passing frequency ranges without transmitting signals.
An exact correlation of these diagrams is again im-
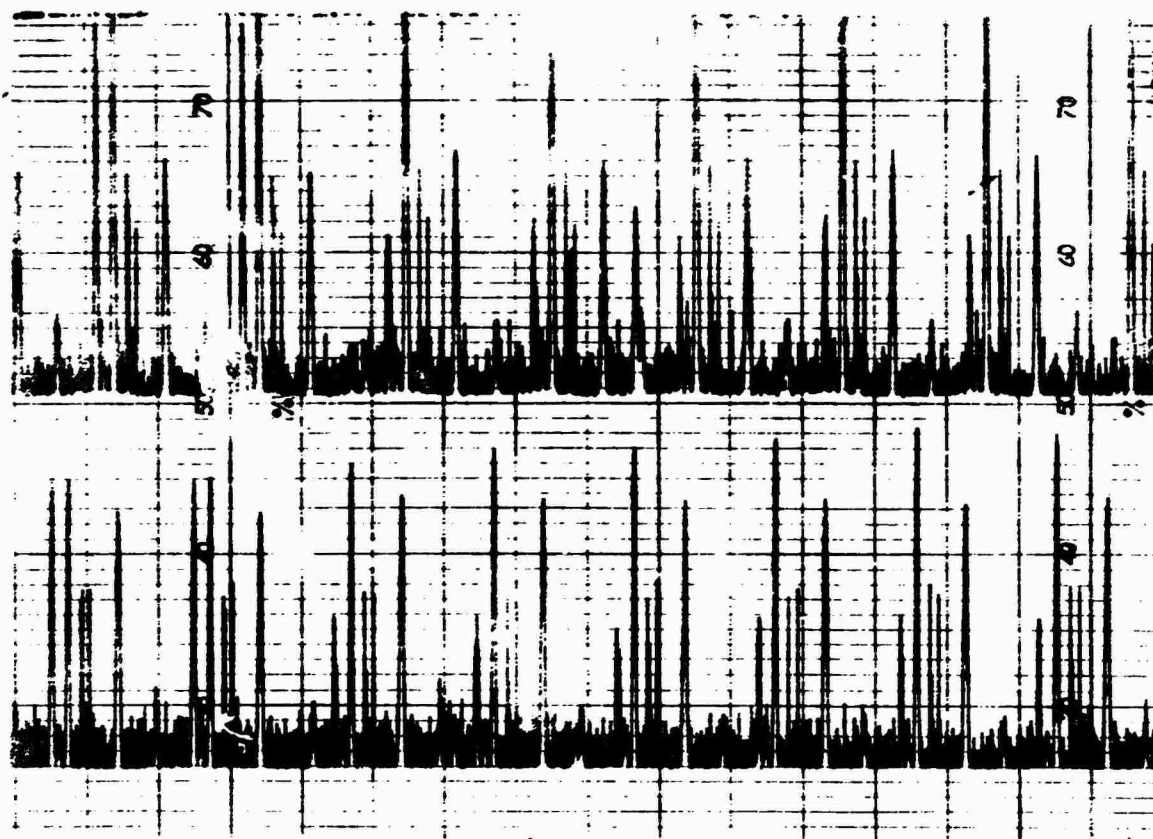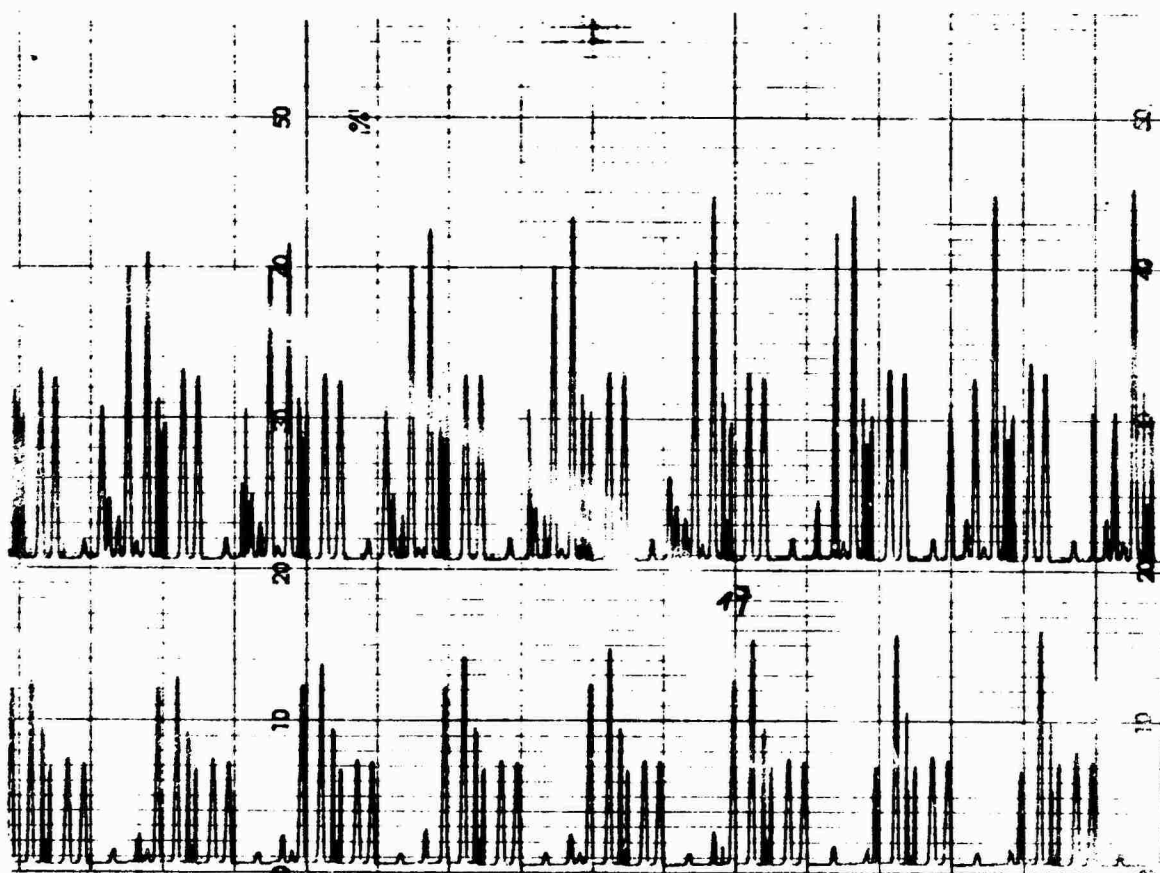possible, as they were plotted at different times.

Fig.: 9.5

Fig.: 9.6

REFERENCES

1   LUKAVEC, R., Über die Eigenschafter kleiner eigenreso-
    nanter Wendelantennen bei niedrigen Frequenzen
    und ihre Felder in dissipativen Medien. Thesis,
    Innsbruck University, 1969

2   HEYNISCH, H., Die Ausbreitung von Mikrowellen und langen
    Wellen auf einer Wendelleitung mit Dielektrikum und
    koaxialem Außenleiter. A.E.Ü. vol. 17, no. 5

3   MEINKE, H., and GUNDLACH, F. W., Taschenbuch der
    HF-Technik, Springer Verlag Wien/New York, 1968

4   HÜTTE 5b, Des Ingenieurs Taschenbuch, Teil B,
    Berlin/München, 1962

5   WHEELER, H. A., Fundamental Limitations of Small Antennas,
    Proc. I.R.E., pp. 1479-1484, Dec. 1947

6   ZHURT, H., Zlektromagnetische Strahlungsfelder, Springer
    Verlag Wien/New York, p. 151, 1953

7   WHEELER, H. A., A Helical Antenna for Circular Polariza-
    tion, Proc. I.R.E., pp. 1484-1488, Dec. 1947

8   GABILLARD, R., DEGAUQUE, P., and WAIT, J. R., Subsurface
    Electromagnetic Telecommunication - A Review, IEEE
    Transactions on Communication Technology, vol. 19,
    no. 6, pp. 1217-1228, Dec. 1971

9   BITTERLICH, W., Magnetische Dipolantennen für Feldstärke-
    messungen im LF- und LF-Bereich. Internat. Elektr.
    Rundsch. Berlin, vol. 21, no. 9, pp. 225-228, 1967

10 NESSLER, N., Die Ausbreitung langer elektromagnetischer
    Wellen durch homogene und inhomogene feste Medien.
    Thesis, Innsbruck University, 1967

11 Final Scientific Report, Theoretical and Experimental
    Studies of VLF and LF Waves; US-Contract No.
    F44620-72-C-0071, Innsbruck University, 1971

12 ROTHE, R., Höhere Mathematik für Mathematiker, Physi-
    ker, Ingenieure. G.B. Teubner, Leipzig, 1954

13 BERGMANN, L., Messungen im Strahlungsfeld eines
    Hertz'schen und eines Abraham'schen ungedämpften
    Erregers. Ann. Phys. vol. 4, p. 13 ff., 1967

14 KELLNER, A. W., Die Bestimmung elektrischer Gesteins-
    parameter aus der Feldstruktur eines magnetischen
    Dipols. Thesis, Innsbruck University, 1969

15 BERGMANN, L., SCHAEFFER, Cl., and MATOSSI, F., Lehr-
    buch der Experimentalphysik, Optik. Walter de
    Gruyter & Co., Berlin, 1966.

16 KLEIN, R., Mathematical Classification and Description
    of the Response Characteristic in the Elliptically
    Polarized VLF and LF Field, Scient. Rep. No. 3,
    US-Contract No. F44620-72-C-0052, Innsbruck
    University, 1972

17 KLEIN, R., Einfluß von Stollenhohlräumen und Inhomoge-
    nitäten auf die Ausbreitung von elektromagneti-
    schen Langwellen durch leitfähiges Medium. Thesis,
    Innsbruck University, 1972

18 BRONSTEIN-SEMENDJAJEW, Taschenbuch der Mathematik,
    Verlag Harry Deutsch, Zürich/Frankfurt a.M., 1967

19 TEICHMANN, H., Physikalische Anwendung der Vektor- und
    Tensorrechnung, BI Hochschultaschenbuch 39/39a,
    Mannheim, 1966

20 BITTERLICH, W., A Phase-sensitive Receiver for VLF
    Signals, Annual Report, US-Contract No. F61052-
    69-C0007, Innsbruck University, 1969

21 BECKSTEIN, H., Schmitt-Trigger mit in weiten Grenzen
        einstellbarer Hysterese. Elektronik, Franzis-Verlag
        München, no. 12, p. 360, 1969

22 BITTERLICH, W., Einführung in die Elektronik, Springer-
        Verlag Wien/New York, p. 512-517, 1967

23 BECKER, K. D., On Reflection and Refraction of Electro-
        magnetic Dipole Fields at Rough Surfaces of Homo-
        geneous and Inhomogeneous Media. Bericht des In-
        stituts für Radiometeorologie und maritime Meteo-
        rologie, Hamburg, No. 21, 1972

24 Handbuch der Physik, Springer Verlag Wien/New York,
        vol. 16, 1958

25 WAIT, J. R., Oblique Reflection of an Electromagnetic
        Plane Wave from a Striated Impedance Surface,
        Journal of Mathematical Physics, vol. 11, no. 4,
        1970

26 PESCHL, E., Funktionentheorie I, BI Hochschultaschen-
        buch 131/131a, Mannheim

27 VILBIG, F., Lehrbuch der Hochfrequenztechnik, Akademi-
        sche Verlagsgesellschaft, Leipzig, 1942

28 WÖBKING, H., Über den Frequenzgang der Dielektrizitäts-
        konstante und der elektrischen Leitfähigkeit bei
        Gesteinen. Thesis, Innsbruck University, 1968

29 GRISSEMANN, Ch., Untersuchung der komplexen Leitfähig-
        keit und Dielektrizitätskonstanten erzhaltiger
        Gesteine an Gesteinsmodellen, Thesis, Innsbruck
        University, 1971

30 SCHUMANN, W. O., Elektrische Wellen, Carl Hauser
        Verlag, München, 1948

31 NESSLER, N., BITTERLICH, W., Überlegungen zur Eichung
        einer Ferritstabantenne für Meßzwecke. Intern. El.
        Rundsch, Berlin, vol. 25, pp. 277-279, 1971

32 BITTERLICH, W., Measuring Device for Recording the
      Field Strength of VLF Signals over Long Periods
      of Time, Scient. Rep. No. 14, US-Contract No.
      61(052)-490, 1965

33 STEINACKER, I., SCOTTI, H., Attenuation in Subsurface
      Signal. Techn. Note No. 2, US-Contract No.
      61(052)-490, 1963

34 BITTERLICH, W., HOMMEL, R., Determination of Rock Con-
      Ductivity from VLF-Propagation Measurements.
      Techn. Note No. 3, US-Contract No. 61(052)-490,1963

35 NESSLER, N., BITTERLICH, W., Die Messung der Leitfähigkeit
      und der Dielektrizitätskonstanten eines schwach
      leitfähigen homogenen Mediums mittels Wellenaus-
      breitung. Acta Physica Austriaca, Springer Verlag
      Wien/New York, vol. 29, pp. 228-240, 1969

36 BITTERLICH, W., Altes Bergwerk mit neuen Aufgaben.
      Der Aufschluß, vol. 21, pp. 107-111, 1970

37 WAIT, J. R., Image Theory of a Quasistatic Magnetic
      Dipole Over a Dissipative Half-Space. Electronics
      Letters, vol. 5, no. 13, pp. 281-282, 1969

38 WEAVER, J. T., Image Theory for an Arbitrary Quasi-
      static Field in the Presence of a Conducting
      Half-Space. Radio Sci. vol. 6, no. 6,
      pp. 647-654, 1971

39 BANNISTER, P. R., Utilization of Image Theory. Techniques
      in Determining the Mutual Coupling between Elevated
      Long Horizontal Line Sources, Radio Sci., vol. 5,
      no. 11, pp. 1375-1381, 1970

40 WASYLKIWSKYJ, W., Gain Efficiency and Receiving Cross
      Section of Antennas in a Dissipative Medium.
      Radio Sci., vol. 6, no. 6, pp. 647-653, 1971.